



HAL
open science

Principes du repliement de la chromatine dévoilés par la microscopie super-résolue multi-couleurs

Mariya Georgieva

► To cite this version:

Mariya Georgieva. Principes du repliement de la chromatine dévoilés par la microscopie super-résolue multi-couleurs. Biophysique. Université Montpellier, 2015. Français. NNT : 2015MONT056 . tel-01591116

HAL Id: tel-01591116

<https://theses.hal.science/tel-01591116>

Submitted on 20 Sep 2017

HAL is a multi-disciplinary open access archive for the deposit and dissemination of scientific research documents, whether they are published or not. The documents may come from teaching and research institutions in France or abroad, or from public or private research centers.

L'archive ouverte pluridisciplinaire **HAL**, est destinée au dépôt et à la diffusion de documents scientifiques de niveau recherche, publiés ou non, émanant des établissements d'enseignement et de recherche français ou étrangers, des laboratoires publics ou privés.

THÈSE

Pour obtenir le grade de
Docteur

Délivré par l'**UNIVERSITE DE MONTPELLIER**

Préparée au sein de l'école doctorale
Sciences chimiques et biologiques pour la santé,
ED 168

Et de l'unité de recherche
Centre de biochimie structurale, UMR5048 U1054

Spécialité : **Biophysique**

Présentée par **Mme Mariya GEORGIEVA**

**Principles of the Higher-Order Chromatin
Folding Unveiled by Multicolor
Superresolution Microscopy**

Soutenue le 8 Décembre 2015 devant le jury composé de

M. Thierry FORNE, DR, UMR5535

Président du jury

M. Marcelo NÖLLMANN, DR, UMR5048 U1054

Directeur de thèse

M. Maxime DAHAN, DR; UMR168

Rapporteur

M. Romain KOSZUL; CR, UMR3525

Rapporteur

M. Frédéric BANTIGNIES, CR, UPR1142

Invité



“The greatest enemy of knowledge is not ignorance; it is the illusion of knowledge.”

— Stephen Hawking

Table of Contents

Summary.....	13
Résumé.....	15
Preface.....	19
1. Chapter 1 – How is the genetic material of a cell organized during interphase?	23
1.1 Packing the whole genome within a cell	25
1.1.1 A historical perspective.....	25
1.1.2 Chromatin fibers.....	27
1.1.3 Chromosome territories	29
1.2 Capturing chromatin conformations.....	31
1.2.1 Proximity ligation: the 3C techniques.....	31
1.2.2 Sub-chromosomal chromatin compartments	32
1.2.3 Self-interacting sub-chromosomal domains.....	36
1.3 Architectural proteins in Drosophila	40
1.4 What mechanisms for TAD formation?	42
2. Chapter 2 – Super-resolution microscopy concepts and applications	43
2.1 Fluorescence microscopy beyond the diffraction limit	45
2.2 Technology overview of super-resolution imaging.....	47
2.2.1 Stimulated emission depletion (STED)	47
2.2.2 Structured illumination microscopy (SIM)	49
2.2.3 Single-molecule localization microscopies (SMLM)	51
2.3 Live-cell imaging	55

2.4	Probes for super-resolution imaging	56
2.4.1	Molecular tags	56
2.4.2	Fluorescent molecules	57
2.5	The nuclear compartment studied with SRM	60
2.5.1	RNAP2 distribution and dynamics	60
2.5.2	Chromatin organization and dynamics.....	61
2.6	Perspectives in SRM	65
3.	Chapter 3 – Imaging nuclear structures with multicolor SMLM.....	67
3.1	Sample preparation	69
3.1.1	Cell culture	69
3.1.2	Fixation and permeabilization	70
3.1.3	Affinity staining of nuclear targets using antibodies.....	71
3.1.4	Imaging buffer for dSTORM	73
3.1.5	Sample mounting.....	74
3.1.6	Antibody conjugation with fluorescent dyes	76
3.2	Image acquisition in SMLM.....	78
3.2.1	Film length.....	78
3.2.2	Excitation/activation scheme	79
3.2.3	Sequential acquisition of two-color SMLM images.....	80
3.3	Data analysis	83
3.3.1	Detection and post-processing of localization data	83
3.3.2	Quantitative analysis of colocalization	86
3.4	Quality control of SMLM images	97
3.4.1	Dual color protein staining as an image validation strategy	98
3.4.2	Differences between secondary and primary antibody staining.....	99
3.4.3	Validation of labeling efficiency using quantitative colocalization analysis	100
3.5	Additional comments and perspectives.....	103

3.6	Materials and methods	106
3.6.1	Microscope used for multicolor SMLM imaging	106
3.6.2	Antibody labeling	108
3.6.3	Image registration for SMLM	110
3.6.4	Drift correction algorithm	110
3.6.5	Simulations for aCBC.....	111
4.	Chapter 4 – SRM applied to the study of Drosophila chromatin folding ..	113
4.1	Summary	117
4.2	Introduction.....	119
4.3	Results	121
4.3.1	Imaging single TD barriers at the single-cell level	121
4.3.2	Local organization of barriers at super-resolution	122
4.3.3	Chromosomal organization of barriers.....	124
4.3.4	Chromatin insulators and nuclear distribution of TD frontiers.....	125
4.3.5	Epigenetic organization of Beaf-32 clusters.....	127
4.4	Discussion	128
4.5	Perspectives and outlook	132
4.6	Main Figures	134
4.7	Experimental Procedures	145
4.8	Supplementary Figures.....	155
	APPENDIX.....	163
	ABREVIATIONS	163
	FIGURES INDEX	165
	FIGURES INDEX – SUPPLEMENTARY DATA CHAPTER 4.....	166
	BIBLIOGRAPHY	167

Summary

Interphase chromatin compaction has been described to follow a recurrent pattern that could be observed in a variety of organisms, such as bacteria, the fruit fly, and human. Genome-wide DNA contact mapping has revealed that in all of these organisms some sequences are preferentially found in proximity with one another and thus form Topologically Associating Domains (TADs). These are in turn separated by regions of low contact, termed TAD borders. What are the determinants of this particular type of chromatin organization and what are its functional implications is still largely unknown.

Genomic sequences analyses have demonstrated that genes within TADs are frequently regulated in a cell type and differentiation stage-dependent manner, while TAD borders are enriched in actively transcribed and housekeeping genes. Moreover, the epigenetic landscape that characterizes TADs changes at the borders of a given domain. Remarkably, the genome-wide binding profiles of a variety of gene regulation effectors including transcription factors, chromatin remodellers and insulator proteins revealed a strong preference for binding at TAD borders. The last category is of particular interest, since its members have the property of establishing long-range gene interactions through the formation of chromatin loops. In an emerging hypothesis TADs could be formed through contacts between TAD border sequences stabilized by the looping activity of architectural proteins.

The present work investigates the roles of insulator proteins in the TAD formation mechanism using *Drosophila melanogaster* as model system. For this purpose,

superresolution imaging was implemented and a series of developments were performed in Structured Illumination Microscopy (SIM) and Single-molecule Localization Microscopy (SMLM). Sample preparation was carefully optimized to fit the specific requirements of both SIM and SMLM, with particular attention on fluorescent labeling for single-molecule detection. SIM and SMLM are young techniques, which provide high detail in the visualization of biological structures. In this context, robust acquisition, quantitative analysis and image quality control procedures were established for multicolor SMLM. These developments were directly applied to study the nuclear organization of the Boundary Element Associated Factor (BEAF-32), one of the 11 insulator proteins discovered to date in *Drosophila*. The strong enrichment on TAD borders and the demonstrated looping activity make BEAF-32 a potent candidate to test for the clustering of TAD borders as a general mechanism of chromatin folding. Multicolor SMLM systematically located BEAF-32 foci at the periphery of large H3K27me3 chromatin domains. In the latter, segments of individual chromatin fibers could be discriminated for the first time through fluorescence microscopy. Quantitative analysis of SMLM images indicated BEAF-32 forms hundreds of surprisingly small foci (45 nm), containing a mean of 5 molecules, which argues against a large-scale looping of BEAF-32-bound chromatin. To directly probe for gene clustering at the DNA level, TAD borders on chromosome 3R were labeled using fluorescent oligonucleotide probes. The number of foci detected by SIM was once more incompatible with a model of chromosome-wide contacting of multiple TAD borders. At a more detailed scale, TAD borders pairs distances were measured at selected loci on chromosomes 2L and 3R, resulting in <5% of paired contacts among the measured barriers. Taken together, these results are inconsistent with constitutive interactions between consecutive or non-consecutive barriers in *Drosophila*.

The study communicated here contributed to the methodological development of super-resolution microscopy yielding high standard protocols and quantitative analyses for multicolor imaging of nuclear structures in cultured cells. As a result, experimental evidence was provided to invalidate the TAD border clustering model as a general mechanism of chromatin folding.

Résumé

Durant l'interphase, l'étape la plus longue du cycle cellulaire, le matériel génétique de la cellule adopte une organisation complexe qui intrigue les scientifiques depuis les débuts de la biologie cellulaire. Il est remarquable que la molécule d'ADN soit compactée de quatre ordres de grandeur pour être contenue dans le noyau. Malgré ce repliement impressionnant, les processus cellulaires majeurs, notamment la transcription, la réparation de l'ADN et la réplication ont lieu avec une précision et coordination étonnante qui assurent le bon fonctionnement physiologique d'organismes complexes que sont les métazoaires. La relation entre le repliement du génome et le fonctionnement cellulaire est un phénomène dynamique et régulé, comme il a été observé en microscopie. En effet, les chromosomes sont organisés chacun dans son « territoire ». En outre, les chromosomes semblent se positionner de manière non-aléatoire par rapport à l'enveloppe nucléaire. Les segments génomiques riches en gènes ont tendance à se retrouver au centre du noyau, tandis que les segments où la chromatine est condensée et peu transcrite sont situés en périphérie. Il a été par ailleurs observé que de nombreux processus nucléaires ont lieu dans un espace confiné, formant des foyers d'activité spécialisée ou « corps » nucléaires. Le plus connu est le nucléole, qui abrite les processus de synthèse et maturation des ribosomes. Mais encore, il a été mis en évidence que des gènes co-régulés, spécifiques à certains tissus sont transcrits dans des « fabriques de transcription ». De manière similaire, les gènes réprimés par les protéines Polycomb sont aussi regroupés dans l'espace nucléaire formant les corps Polycomb.

A l'échelle moléculaire, des études de biologie structurale ont révélé la structure du premier niveau d'organisation de la chromatine – le nucléosome. Ce dernier

est composé d'environ deux tours d'ADN enveloppant un octamère de protéines hautement conservées, les histones. Les domaines amino-terminaux des histones sont spécifiquement marqués par une multitude de modifications covalentes post-transcriptionnelles telles que la méthylation, l'acétylation et la phosphorylation, pour en citer quelques exemples. Ces modifications épigénétiques, par leur effet direct, ou par le recrutement d'autres facteurs, affectent la compaction de la fibre chromatinienne, ce qui affecte à son tour l'activité transcriptionnelle des gènes sous-jacents.

Comment alors les chaînes de nucléosomes, par leurs degrés de compaction régulés forment les territoires chromosomiques ? L'échelle de ces structures a longuement été inaccessible aux études biologiques par leur complexité et leur taille. En effet, la microscopie électronique révèle une densité électronique homogène qui distingue essentiellement deux états de condensation : l'euchromatine (peu condensée, active) et l'hétérochromatine (condensée, inactive). La microscopie optique conventionnelle qui a mis en évidence les territoires chromosomique peut, dans les meilleurs des cas visualiser l'existence de structures au niveau sous-chromosomique, sans information structurale, qui est rendue « floue » sous l'effet de la diffraction de la lumière. Pour visualiser la chromatine avec un détail permettant de distinguer et étudier le repliement du matériel génétique au sein des chromosomes, les microscopies à super-résolution sont nécessaires.

Récemment de nouvelles méthodes de la génomique ont vu le jour et permettent d'établir des cartes de tous les contacts de génomes entiers. Ces techniques ont révélé un niveau de l'architecture tridimensionnelle de la chromatine inconnu jusqu'à présent. A l'échelle des centaines de kilobases, certaines séquences génomiques se trouvent préférentiellement à proximité les unes des autres, formant ainsi des domaines topologiques associés (TAD). Les gènes situés dans le même TAD ont des propriétés épigénétiques similaires, et leur expression au cours de la différenciation semble corrélée, ce qui suggère un lien fort entre la structure de la chromatine et la transcription. Les TADs sont à leur tour séparés par des régions avec peu de contacts, appelées « frontières », qui sont généralement occupées par des protéines dites « isolatrices ». Les déterminants de cette organisation chromatinienne particulière et ses implications fonctionnelles sont largement méconnus. Selon une hypothèse récente, les TADs seraient formés par des contacts entre les séquences des frontières, qui seraient stabilisés par la formation de boucles de chromatine via les protéines isolatrices.

Les travaux présentés dans cette thèse ont pour but d'étudier le rôle des protéines isolatrices dans le mécanisme de formation des TADs chez la drosophile. La microscopie super-résolue multi-couleurs a été implémentée et une série de développements ont été réalisés en microscopie à illumination structurée (SIM) et la microscopie de localisation de molécules uniques par photoactivation (SMLM), avec une attention particulière sur le marquage fluorescent et l'analyse d'images quantitative. Ces développements ont directement été appliqués à l'étude de l'organisation nucléaire de la protéine associée aux éléments frontières (BEAF-32), une des 11 protéines isolatrices identifiées à ce jour chez la drosophile. Le fort enrichissement aux frontières des TADs, ainsi que son activité dans la formation de boucles d'ADN font de BEAF-32 un candidat intéressant pour tester l'hypothèse de regroupement de frontières comme mécanisme général de repliement de la chromatine.

La technique SMLM multi-couleurs a systématiquement localisé BEAF-32 à la périphérie des larges régions du génome portant la marque épigénétique H3K27me3. La distribution de ce marquage de répression par les protéines Polycomb a été révélée avec un détail qui n'avait pas été atteint lors d'études antérieures. La chromatine marquée par H3K27me3 est distribuée en larges domaines formés par des fibres finement intriquées, dont des segments de taille variable sont visibles. Remarquablement, l'analyse quantitative des images SMLM a révélé que BEAF-32 forme des centaines de foyers d'une taille de 45 nm, composés en moyenne de 5 molécules, ce qui est en désaccord avec la présence de boucles de chromatine à large échelle. Afin de tester le regroupement de gènes directement au niveau de l'ADN, des frontières ont été marquées par des oligonucléotides fluorescents. Le nombre de foyers détectés par SIM s'est à nouveau révélé incompatible avec le modèle de contacts entre les frontières tout le long du génome. Par ailleurs, les distances entre paires de frontières au niveau de deux régions génomiques ont montré <5% de contacts. Ensemble, ces résultats sont en désaccord avec l'établissement d'interactions entre barrières chez la drosophile.

Enfin, ces travaux de thèse ont contribué au développement méthodologique de la microscopie super-résolue, ce qui a permis d'apporter des preuves expérimentales invalidant le modèle de regroupement des frontières comme mécanisme général du repliement chromatinien.

Preface and acknowledgements

In 2011 I joined Dr. Marcelo Nöllmann's Lab at the Center of Structural Biochemistry in Montpellier. Marcelo proposed a project to study the role of insulator proteins in the organization of higher-order chromatin architecture in *Drosophila*. The structure of the chromatin fiber was known from crystallography and electron microscopy. On a higher structural level, the segregated nuclear localization of chromosomes had been observed by confocal fluorescence microscopy. However, the majority of biological processes in gene regulation involve an intricate organization at intermediate structural levels, which could not be addressed with methods available in the biology toolbox.

Insulator sequences and their binding proteins (IBPs) were known to be involved in the regulation of gene expression through the establishment of chromatin contacts between genomic regions distant at hundreds of kilobases and spanning multiple genes. There was microscopy evidence on the distribution of one class of IBPs that were seemingly organized in large nuclear bodies, in analogy with transcription factories and Polycomb bodies. The recently introduced super-resolution fluorescence microscopy techniques appeared then as a tool with high potential to uncover the architecture of these nucleoprotein assemblies.

Little before I joined the project, a super-resolution localization microscope had been built in the lab. To study the complex interplay between the various protein candidates involved in insulator body formation, a multicolor implementation of super-resolution experiments, mainly in Structured Illumination Microscopy (a commercial setup was available) and Single-molecule Localization Microscopies

(SMLM) was needed. The first six months of the project were spent in single-molecule analyses of the photoswitching properties of two organic fluorophores that would be used in multicolor imaging. Another six months were necessary to obtain the first reconstructed images of lamin with the expected almost continuous distribution along the nuclear periphery. In the process of image optimization it became clear that custom analyses are needed to extract biologically meaningful information from the super-resolution data.

Remarkably, once images with satisfactory quality were obtained, a whole new paradigm of nuclear organization was revealed. Indeed no insulator body-like structures could be observed. Rather IBPs appeared as large numbers of discrete foci, with nearly individual molecule sizes and composition, suggesting that these would not be sites of large-scale stable chromatin contacts.

This work has been made possible by the joint efforts and positive attitude of all the DNA Segregation and remodeling team members to whom I address my warm gratitude. I dedicate a special thought to Alessandro Valeri and Jean-Bernard Fiche who gave me solid ground to learn programming and image analysis with their expertise in fluorophore photophysics and optical device development respectively. I would also like to thank Laura Oudjedi, it has been a pleasure to collaborate and share. I am thankful to Delphine Chamousset and Diego Cattoni whose energy and rigorous work substantially contributed to the Insulator project advances. It has been a challenging and stimulating journey to work under the supportive supervision of Marcelo Nöllmann, to whom I am most grateful for providing me with excellent working conditions and the freedom to develop the skills I desired.

All my gratitude and love to my parents, my sister and my friends, who give me the strength to progress on the path I have chosen. With Linnea Olofsson and Svilena Ivanova we shared pain and joy in life and science which made the adventure priceless. My warmest feelings to Radimir Ivanov and Rayna Ivanova, my beloved husband and daughter, I am infinitely blessed to have you in my life...

Author's note

This thesis is organized in four chapters. In chapter 1, I introduce the current knowledge in interphase chromatin organization and its interplay with gene regulation processes, with an emphasis on *Drosophila* and mammalian model systems. The following chapter is an introduction to super-resolution methods. I discuss currently available developments in instrumentation, analysis and fluorescent molecular probes with particular attention to imaging of nuclear structures in eukaryotes. In chapter 3, I present and discuss the results I have achieved in terms of multicolor SMLM imaging, including sample preparation, image acquisition, data analysis, and procedures for quality control. Last, chapter 4 is in the form of a research article manuscript, which is in preparation for publication. This study was a joint project with my colleague Alessandro Valeri, in which we combined a series of super-resolution imaging modalities and analyses. Our results strongly suggest that topological domain borders in *Drosophila* are individual dynamic segments of chromatin, introducing a new model for higher-order genomic organization.

Chapter 1

How is the genetic material of a cell organized during interphase?

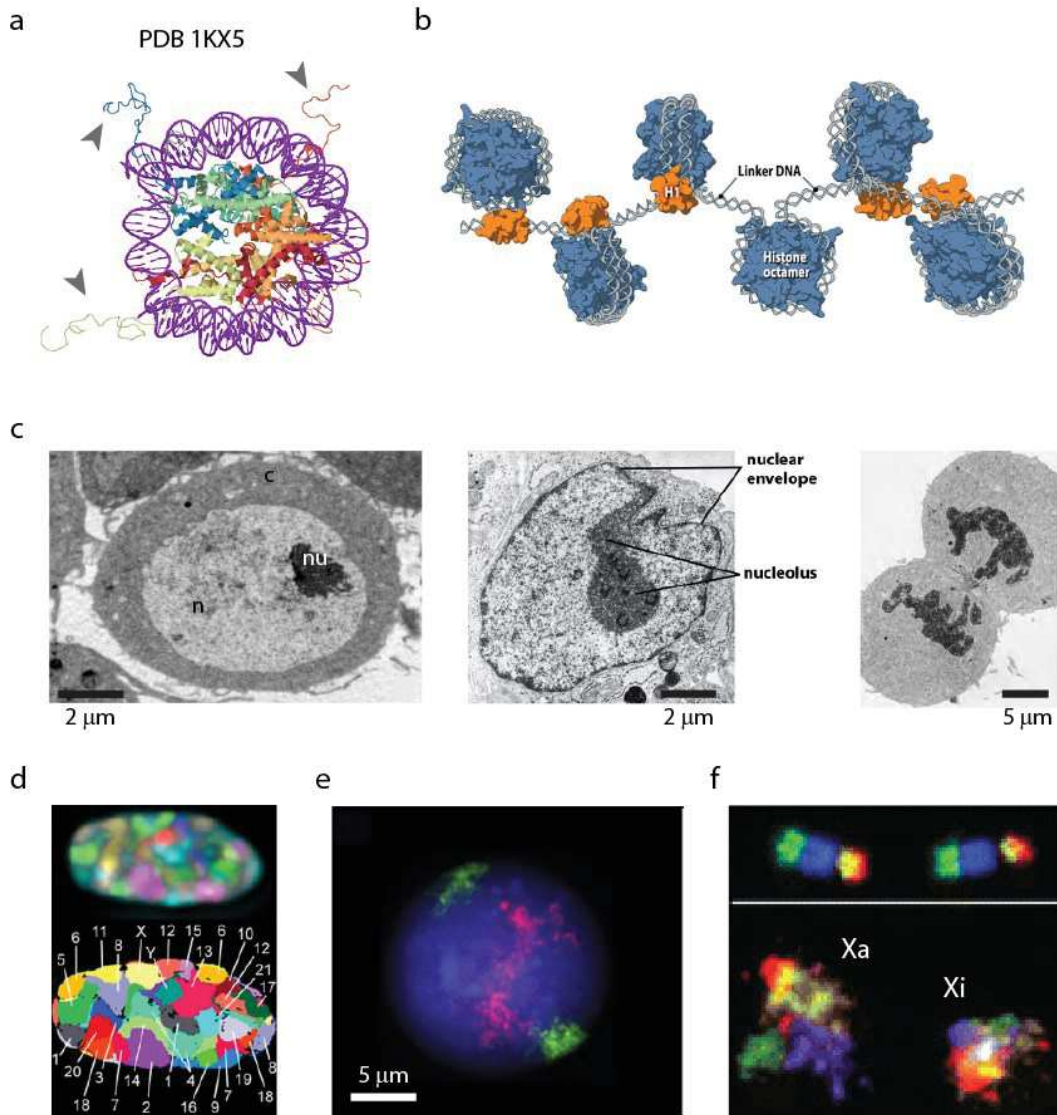
The nucleus is the largest and most easily discernible organelle of eukaryotic cells, and it was observed even with the first microscopes. And yet it conceals a puzzling phenomenon - how the millions and even billions of nucleotides of genomes are arranged in the crowded nuclear space while the genetic programs of organisms are performed with striking reproducibility? In this first chapter I overview current knowledge on interphase chromatin architecture and the interplay with gene regulation processes. At the scale of ~ 100 base pairs, DNA is wrapped around histones to form nucleosome fibers. At the scale of the whole nucleus, each chromosome occupies an individual territory. Recent advances in genomics have allowed a new level of chromatin organization to be uncovered between these two scales. Topological domains are self-interacting regions spanning 10 kb to 2 Mb and appear to host developmentally regulated genes. The domains are separated by contact-depleted regions or boundaries that play a role in the establishment of such conserved chromatin architecture, although the underlying mechanisms remain elusive.

1.1 Packing the whole genome within a cell

1.1.1 A historical perspective

On Earth it is estimated that there are more than 10 million species, as diverse as plants, fungi, bacteria, and animals. Despite the impressive differences between living organisms, they all share common structural and functional features. At the molecular level, the same chemical compounds serve as building blocks of all living matter, such as nucleic acids, proteins, lipids and sugars. The minimal unit carrying the potential for life is the cell, which contains all the hereditary information of a species. The cell was first observed in the middle of the 17th century by the physicist and microscopist Robert Hooke (1635–1702). Nearly two centuries later (1838 and 1839), the botanist Matthias Jakob Schleiden (1804–1881) and the zoologist Theodor Schwann (1810–1882) mark the beginning of cell biology by postulating that “the elementary parts of all tissues are formed of cells”, known as the cell doctrine. Little before the discovery of Schleiden and Schwann, in 1831, the nucleus was identified as an essential constituent of living cells by the botanist Robert Brown (1773–1858). In the following years, the introduction of the oil-immersion lens, as well as the development of new sample fixation and staining methods led to the identification of various cytoplasmic organelles such as the endoplasmic reticulum, mitochondria, and the Golgi apparatus. Within the nucleus, the nucleolus and a stainable substance could be seen. The latter, called “chromatin” by Walther Flemming (1843–1905), would take the form of densely stained filamentous structures (now known as chromosomes) during cell division. Flemming, who also introduced the term “mitosis”, described the splitting of chromosomes and their movement to opposite poles of the dividing cell (Mazzarello, 1999). Mitosis is a universal mechanism for the transmission of the genetic information to the offspring, and another feature common to all living organisms.

Figure 1.1 - Eukaryotic chromatin at various scales



(a) – Crystal structure of the nucleosome particle: 1KX5, front view (Davey 2002). The DNA double helix (magenta) is wrapped around the histone octamer (monomers labelled from blue to red). The arrowheads point to the N-terminal tails of 3 of the monomers. **(b)** – Molecular model of the 10-nm nucleosome fiber: DNA (grey), core histone octamer (blue), histone H1 (orange) stabilizes the nucleosome at the base of the linker sequences. **(c)** – Transmission electron microscopy images of a *Drosophila* S2 cell (Zhu 2013) (left; c-cytoplasm, n-nucleus, nu-nucleolus); a human fibroblast (from Molecular biology of the cell 5/e, ©Garland science 2008) (middle), a human embryonic kidney cell in cytokinesis where segregated chromosomes appear as two dark areas (right). **(d)** – Chromosome territories visualized by 24-color 3D-FISH (Bolzer 2005): pseudocolor image of all 46 chromosomes in a human G0 fibroblast (top), annotations of chromosomes in the same cell (bottom). **(e)** – Human lymphoblastoid cell nucleus hybridized by FISH with paint for the gene-rich human chromosome 19 (red) and gene-poor chromosome 18 (green) reveals the radial organization of chromosomes in the nucleus (Bickmore 2013). **(f)** – Top: Two human X chromosomes in a human fibroblast metaphase plate are shown after multicolor FISH representing four segments from qter to pter (q-arm: green, blue; p-arm: yellow, red). Bottom: Projections of light optical sections through the Xa- and Xi-territory of a human fibroblast nucleus following 3D FISH with the same labeling show four separate domains of these segments within the Xa- and Xi-territory (Cremer 2010).

1.1.2 Chromatin fibers

It is now well established that chromatin is the form under which the hereditary information is stored in the cell nucleus. Chromatin consists of two main types of substances: (1) the cell's genetic material encoded in the molecules of deoxyribonucleic acid (DNA), and (2) DNA-binding proteins. In a eukaryotic cell, genomic DNA must be compacted by four orders of magnitude to fit into the micrometer-sized nucleus (volume <1 pL), and yet it is accessible to a variety of highly regulated and specific processes, such as transcription, replication, and repair. However, the electrostatic properties of DNA challenge the folding within the limited nuclear space. Indeed, the negative charges of the phosphate groups that cover the surface of the DNA double helix are partially neutralized by wrapping around a basic protein complex, known as the core histone octamer (Maeshima et al., 2014). Histones are the most abundant proteins in chromatin and bind DNA mainly as nucleosomes composed of two copies each of H2A, H2B, H3, and H4 (Figure 1.1a). Wrapping of DNA around nucleosomes represents the first level of packaging, which effectively shortens the length of chromosomes by 7-fold (Fraser et al., 2015). The histone amino- and carboxy-terminal tails extend out of the nucleosome core and are subject to posttranslational modifications (PTMs) on multiple residues, the most studied of which are acetylation, phosphorylation, methylation, ADP-ribosylation, sumoylation, ubiquitylation (Kouzarides, 2007). Histone PTMs can directly affect the degree of chromatin local compaction, for instance acetylation and deacetylation lead to de-condensation and condensation respectively. Specific effector proteins that bind PTMs are also recruited to control the accessibility of some sequences. Thus, the particular combinations of PTMs over a given genomic region contribute to regulate the transcriptional outcome of its genes (see below).

The nucleosome is the first level of chromatin compaction and its crystal structure has been solved with a resolution of 1.9 \AA (Figure 1.1a) (Davey et al., 2002). A DNA segment of 147 base pairs (bp) performs 1.7 left-handed superhelical turns around a histone octamer. Individual nucleosomes are connected by 20-80 bp of linker DNA, to form the nucleosome fiber, also known as the 10-nm fiber (Figure 1.1b). Because only about half of the negative charges in DNA are neutralized by core histones, the remaining charge must be neutralized by other factors (e.g. linker histone H1, divalent cations, and other

positively charged molecules) for additional folding (Figure 1.1b) (Maeshima et al., 2014). Furthermore, nucleosomes are not homogeneously distributed throughout the genome. Digestion with DNA degradation enzymes such as DNaseI has allowed regions on chromatin that are cleaved with high efficiency to be identified, and named DNaseI hypersensitive sites (DHSs). These sites reflect a high local accessibility of DNA, which occur due to low density or depletion of nucleosomes, a hallmark of transcriptional activity (Thurman et al., 2012). DNaseI digestion has led to the discovery of all classes of cis-regulatory elements (i.e. regulatory DNA sequences), among which promoters, enhancers, repressors, silencers, locus control regions and insulators (see below).

Chromatin organization changes dramatically throughout the cell cycle. During interphase, DNA fibers adopt a loose conformation with only locally increased levels of compaction. In contrast, during mitosis, DNA in chromosomes is highly condensed to reach their characteristic elongated shapes (Figure 1.1c). Hence, much research concentrated over the last decades in uncovering the intermediate structures between the 10-nm fiber and the metaphase chromosome, and in studying the molecular mechanisms governing chromatin folding. In 1976, purified chromatin fibers were observed in transmission electron microscopy (EM) for the first time, revealing a folding of chromatin in fibers with a diameter of 30 nm (Finch and Klug, 1976). This observation led to the widespread assumption that the 10-nm fiber forms the 30 nm transcriptionally inactive fiber, and subsequently, the higher order chromatin structures observed during interphase and mitosis. According to the “hierarchical helical folding model”, the 30-nm chromatin fiber is folded progressively into larger fibers, including ~100-nm and then ~200-nm fibers, to form large interphase chromatin fibers (chromonema fibers) or mitotic chromosomes (Horn and Peterson, 2002). Alternatively, the “radial loop model” assumes that a 30-nm chromatin fiber folds into radially oriented loops to form mitotic chromosomes (Maeshima et al., 2014). Remarkably, only the 10-nm fiber, and not the 30-nm fiber, was observed *in vivo* using cryo-EM (Dubochet et al., 1988). Subsequent small-angle X-ray scattering (SAXS) indicated the 30-nm fiber would be a consequence of the chromatin isolation procedures and not a native state in cells either in interphase or mitosis (Nishino et al., 2012). These observations argue against the hierarchical model of chromatin folding, and suggest that rather irregularly folded 10-nm nucleosome fibers form the bulk structure of human interphase chromatin and mitotic

chromosomes. Interestingly, the scattering properties also hinted the existence of a scale-free structure or fractal nature up to ~275-nm in interphase chromatin and ~1,000-nm in mitotic chromosomes, which gives a physical dimension to sub-chromosomal DNA organization.

1.1.3 Chromosome territories

Optical microscopy observations of animal cell nuclei performed by Carl Rabl in the end of the 19th century introduced the concept of a territorial organization of interphase chromosomes. In 1909, the term chromosome territory (CT) was used by Theodor Boveri, who argued that after mitosis chromosomes occupy a distinct part of the nuclear space (Cremer and Cremer, 2010). In contrast, when observed with EM, interphase nucleosome fiber continuity could not be distinguished and suggests chromosomes are intermingled in the nuclear space. However, chromatin organization appears nonrandom in EM, since electron-dense regions in the nuclear periphery of mammalian cells, known as heterochromatin, could be discriminated (Figure 1.1c, middle). This observation, though, could not be generalized to all cell types and organisms, as for instance *Drosophila* S2 cells heterochromatin does not appear preferentially localized near the nuclear envelope (Figure 1.1c, left). CTs could be directly visualized once the *in situ* hybridization, and more recently, Fluorescence in situ hybridization (FISH) techniques were introduced (Cremer and Cremer, 2010). These use oligonucleotides complementary to a DNA sequence of interest, which are directly labeled with a fluorophore or functionalized by the attachment of a hapten. A series of developments in the design of chromosome-specific fluorescent probes has led to the experimental demonstration of the organization of interphase chromatin in CTs (Figure 1.1d). The direct evidence for the existence of CTs, provided by FISH has opened a new area of research, which investigates the patterns of chromatin fiber organization at the nuclear and whole-chromosome level.

Radial distribution and proximity patterns

Radial distribution analysis of all human chromosomes revealed a tendency for gene dense genomic regions to be localized in the nuclear interior, while gene poor regions were preferably at the periphery (Figure 1.1e) (Boyle et al., 2001).

This tendency was observed in other species which suggested that gene density within windows of 2–10 Mb is a strong player for the radial position of chromatin in the nucleus (Cremer and Cremer, 2010). Additional parameters were also correlated with non-random CTs distribution, for instance transcriptional activity, replication timing, and GC content (Cremer et al., 2003; Kozubek et al., 2002; Küpper et al., 2007; Murmann et al., 2005). Radial positions of specific gene regions were shown to differ significantly between cell types (Hepperger et al., 2008), which suggests chromosome radial localization may be a regulated process.

Proximity patterns between non-homologous CTs appeared nonrandom as well in mammalian tissues (Caddle et al., 2007; Khalil et al., 2007; Parada et al., 2004). Interestingly, the non-randomness of the distances between couples of genomic regions was reflected by preferential associations within cell populations, although characterized with a marked cell to cell variability. These observations indicate relative chromosome organization is not a deterministic process.

Sub-chromosomal domains within CTs

CTs visualized by FISH appear as structures with various shapes composed of sub-chromosomal domains (Khalil et al., 2007; Küpper et al., 2007) (Figure 1.1f). The existence of domains within CTs was first suggested in studies in which pulse labeling of DNA replication revealed foci of ~ 1 Mb that persisted throughout cell division (Albiez et al., 2006; Berezney et al., 2005; Schermelleh et al., 2001). It seems likely, then, that smaller domains would build these Mb-scale regions.

The positions of individual genes relative to CTs in the context of transcriptional activity have also been probed. It appears the outer surface of an individual CT does not provide a particular compartment for gene dense and/or transcriptionally active chromatin (Cremer and Cremer, 2010). Some particular cases of gene relocation to the CTs periphery have been reported, for instance the *MHC* (Volpi et al., 2000) or *HOX* (Chambeyron et al., 2005) gene clusters. On a more global level, however, gene-dense and/or highly expressed sequences were found equally distributed throughout their respective territories (Küpper et al., 2007; Mahy et al., 2002).

Overall, both microscopy studies using FISH and structural investigations of the nucleosome fiber support a hierarchical, multi-scale model of non-random chromatin folding at the sub-chromosome level. Although highly specific and sensitive to the biological variability, these methods allow only conclusion on particular gene regions to be made. A more systematic characterization of chromatin topologies at higher genomic resolution has been achieved by the development of high-throughput genomic techniques that are discussed in the following sections.

1.2 Capturing chromatin conformations

1.2.1 Proximity ligation: the 3C techniques

Research in the field of chromatin biology has significantly benefited from the development of a molecular biology approach allowing the physical proximity of genomic regions to be assessed. In 2002, (Dekker et al., 2002) introduced the chromosome conformation capture (3C) technology. This approach is based on the assumption that interactions between close regions are more likely to be captured by cross-linking than are those between regions located far away. Therefore, contact frequencies in a cell population essentially reflect how chromatin is organized in the nucleus of individual cells at a given time. By considering the frequency to be inversely proportional to the physical distance, genome architecture can be modeled with this type of data.

To perform 3C, a population of cells is chemically fixed with formaldehyde to create covalent bonds between chromatin segments (Dekker et al., 2002). The cross-linked chromatin is then digested with a restriction enzyme, which cuts at specific sites across the genome. The type of enzyme selected defines the resolution of the 3C experiment, since it determines the size of the crosslinked fragments by the frequency of enzymatic sites. The digested DNA is then diluted and crosslinked fragment are ligated, which results in unique DNA junctions that are quantifiable by PCR (Dekker et al., 2002; Hagège et al., 2007). As interactions are measured individually, 3C is generally used for small-scale analysis, which allows the detection of enhancer-promoter loops for instance (Fraser et al., 2015).

More recently, 3C was coupled to Next-Generation Sequencing (NGS) technology which led to the development of the 4C, 5C and Hi-C methods (Dostie et al., 2006; Lieberman-Aiden et al., 2009; Sexton et al., 2012; Simonis et al., 2007). These developments permitted the detection of genome-wide chromatin interactions and the investigation of local chromatin folding at scales of 10-100 Kb depending on the study (Figure 1.2).

1.2.2 Sub-chromosomal chromatin compartments

Consistent with the genome organization in CTs observed in microscopy, genome-wide contact maps were mostly enriched in *cis* rather than in *trans* associations (Kalhor et al., 2012; Lieberman-Aiden et al., 2009; Sexton et al., 2012; Zhang et al., 2012). Furthermore, both 4C (Tolhuis et al., 2011) and Hi-C (Hou et al., 2012; Kalhor et al., 2012; Sexton et al., 2012) analyses identified the centromere as a barrier that reduces associations between sequences located on the two opposite arms of the same chromosome, confirming a structural feature that had been observed previously (Dietzel et al., 1998).

The first Hi-C study provided a relatively coarse-grained view of chromatin topology of mouse and human genomes, with a resolution of ~ 1 Mb (Lieberman-Aiden et al., 2009). These experiments revealed chromosomes are divided into large multi-Mb compartments (or "megadomains") that contain either active and open (A-compartments) or inactive and closed chromatin (B-compartments). Long-range homologous contacts were predominant: A compartments cluster with other A compartments, as do B compartments with B compartments. Given that different cell types express different gene sets driven by distinct groups of regulatory elements, the positions of A- and B-compartments change accordingly. The correlation of contact frequencies with active gene-dense and inactive gene-poor regions had also been observed by 4C analysis which mapped the genome-wide contacts of the mouse β -globin locus (Simonis et al., 2007). Interestingly though, a systematic FISH analysis in a 4.3 Mb region of the mouse chromosome 14 demonstrated the tendency to cluster together for multiple gene-rich segments but not for gene-poor domains (Shopland et al., 2006).

Clustering of active regions

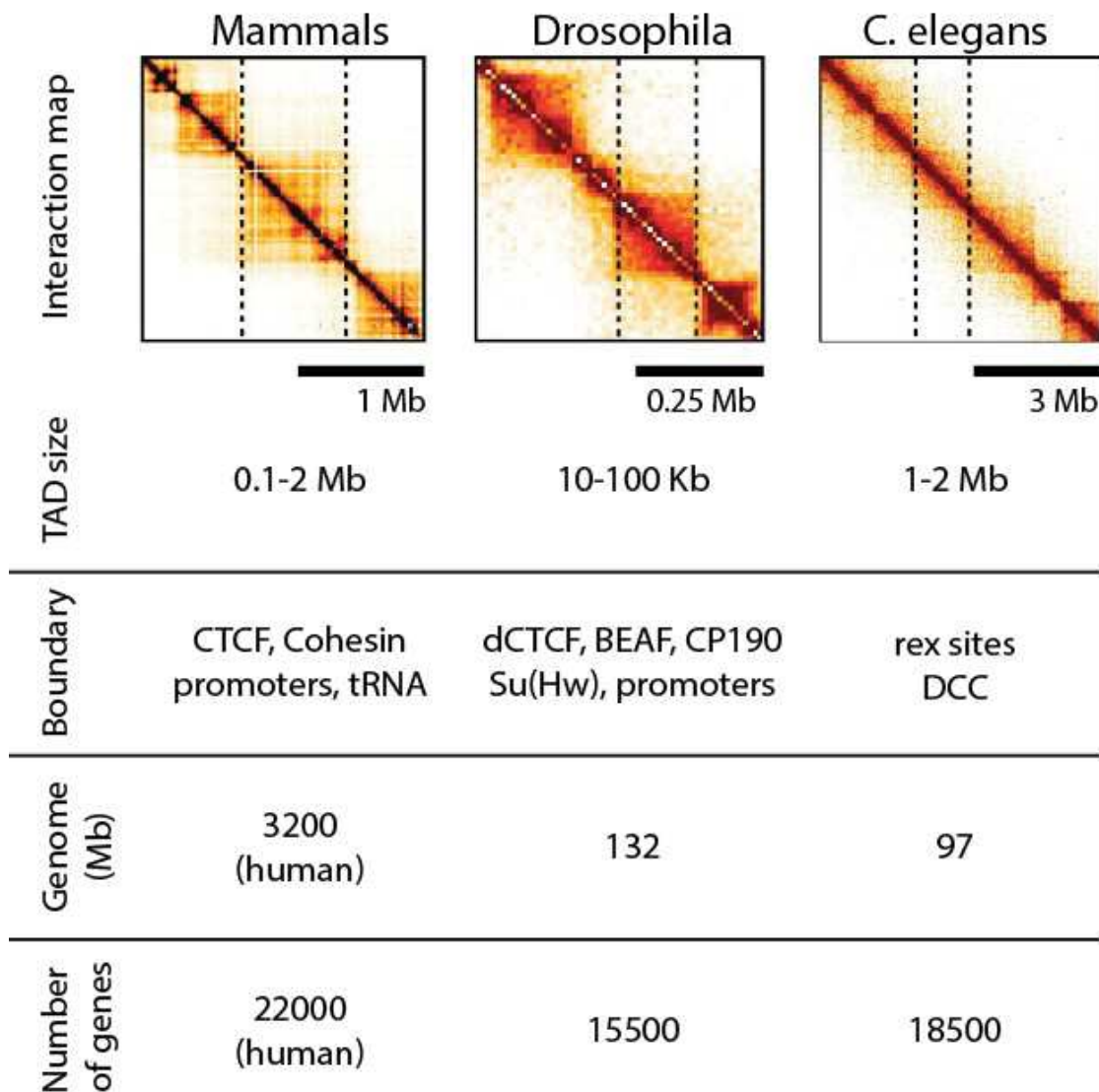
The associations between genes in active regions were not dependent on ongoing transcription as shown by (Palstra et al., 2008), suggesting some alternative chromatin functional feature may be responsible for the maintenance of interaction networks (Bickmore and van Steensel, 2013). The tendency of active regions to form long-range and interchromosomal contacts with each other has been correlated with the DHS chromatin profiles, which reflect high accessibility regions of the chromatin fiber (discussed above) (Hakim et al., 2011; Yaffe and Tanay, 2011). In addition, 4C analyses of the β -globin locus indicated active chromatin associations are similar between tissue types and are gene function-independent (Simonis et al., 2007), an observation generalized to the human genome in a recent Hi-C study (Kalhor et al., 2012). These observations suggest that preferential clustering of active chromatin regions is a general property of genomes, possibly influenced by the presence of ubiquitous factors.

Clustering of repressed regions

Similarly to active regions, inactive loci were preferentially captured with other inactive regions of the genome both in 4C (Simonis et al., 2007) and Hi-C (Lieberman-Aiden et al., 2009). Moreover, in the *Drosophila* embryo, the spatial clustering of telomeres and of centromeres with each other and with the heterochromatic 4th chromosome was detected (Sexton et al., 2012). The same observation was made using microscopy to visualize *Drosophila* polytene chromosomes and S2 cells labeled with the repressive epigenetic mark of constitutive heterochromatin H3K9me2 (Riddle et al., 2011). Repressed regions are physically restrained in their associations, as Hi-C contacts were spanning shorter distances on the chromosome compared to active domains (Bickmore and van Steensel, 2013). The difference in contacts profile of a region observed between the active and inactive state of a locus was directly visualized in mammalian ESC cells. The *Hox* loci are maintained in a silent and compact chromatin state by the Polycomb PRC2 and PRC1 complexes (Eskeland et al., 2010), and are found within their host CTs. Upon activation, *Hox* loci can be found at different positions in the nucleus with active alleles inside or outside their CT cores (Morey and Helin, 2010), which also increased the 3C detection of their interchromosomal associations (Würtele and Chartrand, 2006). In

Drosophila embryos, spatial colocalization and long-range contacts of silent Polycomb targets have been demonstrated (Bantignies et al., 2011). Silencing was not sufficient to target non-Polycomb target loci to Polycomb sites, and associations of Polycomb target loci were dependent on PcG proteins. This indicates that some spatial associations of silenced genes may be regulated by specific epigenetic silencing mechanisms.

Figure 1.2 - Topological domains seen by Hi-C



The three images represent Hi-C contact maps on the X chromosomes of three species. Contact enrichment ranging from white (low interaction frequencies) to black (high interaction frequencies). Mammals: mouse Xic in ES cells Nora 2012. Drosophila: chrX:4000001–4550001 in S2 cells; *C. elegans* embryos: chrX:5760001–12780001 Crane 2015. Genome and TAD features are summarized in the table at the bottom of the figure. Adapted from Dekker Heard 2015.

1.2.3 Self-interacting sub-chromosomal domains

Recent developments in 5C and Hi-C methods have resulted in contact maps with high resolution and rich coverage, unveiling a new level of three-dimensional chromosome architecture. A series of studies in various organisms, such as bacteria, *Drosophila*, nematodes, mouse and human, have demonstrated sub-chromosomal compartments (A and B) are partitioned into smaller compartments themselves. Indeed, at the sub-megabase scale, chromatin appeared partitioned into discrete regions called topological domains (TDs), topologically associating domains (TADs), physical domains^{*}, and chromosome interaction domains (CIDs) (Dixon et al., 2012; Hou et al., 2012; Le et al., 2013; Marbouty et al., 2015; Nora et al., 2012; Sexton et al., 2012). Loci within the same TAD interact more frequently with each other than with loci located in neighboring domains (Figure 1.2).

The partitioning of the *Drosophila* genome into physical domains was introduced by a 3C-seq study in early embryos (Sexton et al., 2012), and using Hi-C in the Kc167 cell line (Hou et al., 2012). Both studies described more than 1100 TADs of 10-100 kb, with a median size of ~60 kb. Remarkably, 42% of the defined TAD borders defined by the two studies overlapped at ± 4 kb (Ea et al., 2015).

In mammals, TADs were evidenced by a 5C analysis of the X chromosome inactivation center (Xic) in mouse cells (Nora et al., 2012), and by a Hi-C study in human and mouse cells (Dixon et al., 2012). Mammalian genomes are composed of more than 2000 TADs ranging from 10 kb to 1-2 Mb (median size of ~800 kb), and cover >90% of the entire genome, indicating that TADs constitute a key organizational element of mammalian chromosomes (Ea et al., 2015). Importantly, TDs were detected at the single-cell level, suggesting that they represent a genuine stable organizational principle of mammalian genomes and are not a result of ensemble averaging (Nagano et al., 2013). These preferential associations were also observed in microscopy, as FISH probes were on average closer within TADs than between them[†] (Giorgetti et al., 2014; Nora et al., 2012). The potential functional roles of physical domains are reflected by their

* These terms will be used equivalently throughout this manuscript.

† Recently, Williamson et al. (Williamson et al., 2014) found discrepancies between 5C and FISH results, pointing to the necessity of using both techniques in combination to cross-validate observations.

complete depletion during massive chromosome compaction events such as X chromosome inactivation (Nora et al., 2012) and mitosis (Naumova et al., 2013). Unicellular organisms were also found to contain chromatin compartments. In yeast, the *Schizosaccharomyces pombe* genome is partitioned into “chromatin globules” with a size of 50-100 kb (Mizuguchi et al., 2014). Interestingly, globule boundaries are enriched for 3' ends of convergent genes. These convergent sites are bound by the cohesin complex, which was shown to be essential to the maintenance of globules. TD-like organization was also found in the bacterial genomes of *Caulobacter crescentus* (Le et al., 2013; Umbarger et al., 2011) and *Bacillus subtilis* (Marbouty et al., 2015). In prokaryotes, transcription and replication were identified as major players of chromosome remodeling.

Recently, a genome-wide chromatin interaction map was released for *C. elegans* embryos (Crane et al., 2015). On autosomes no strong TADs were observed, however, large TADs (1-2 Mb) were present along the two copies of the X chromosome in hermaphrodites. In plants, *Arabidopsis thaliana* chromosomes did not contain TDs, rather small interactive regions were found, which involved constitutive and facultative heterochromatin islands containing the repressive marks H3K9me2, and H3K27me3 respectively (Feng et al., 2014). These findings suggest that higher order chromatin folding may involve different mechanisms among metazoan genomes.

Properties of topological domains

A remarkable feature of physical domains is the conservation in their boundary positions during differentiation and among species. The positions of a large proportion (~50%) of TD borders were conserved across cell types in *Drosophila* and mammals (Dixon et al., 2012; Hou et al., 2012; Nora et al., 2012; Sexton et al., 2012), and were even highly conserved between mouse and human (Dixon et al., 2012; Vietri Rudan et al., 2015). Furthermore, a comparative Hi-C study revealed TAD organization is strongly conserved in syntenic regions and that TADs are reorganized as intact modules during evolution (Vietri Rudan et al., 2015). In contrast, intra-TAD contacts change between cell types and differentiation, with some contacts appearing, while others are lost (Nora et al., 2012). More than 96% of cell-specific long-range interactions (LRI) across regions beyond 20 kb are found within the same TAD in mammals (Dixon et al.,

2012; Ea et al., 2015). A large proportion of these contacts are mapped to regulatory enhancer-promoter interaction events that orchestrate transcription during development (Phillips-Cremins et al., 2013). Accumulating evidence suggests that chromatin interactions involved in developmental transcription regulation are physically constrained within mammalian TADs (Dekker and Heard, 2015). On the other hand TAD borders are stable during development. Consistently, the disruption of TAD boundaries in loci involved in malformation syndromes has led to aberrant gene expression (Lupiáñez et al., 2015). These observations imply that two different activities would be necessary to define genome topology. The first would mediate regulatory enhancer-promoter LRI within TADs, and the second would be involved in maintaining TAD borders to avoid promiscuous associations between neighboring TADs.

In *Drosophila* little is known about differences in chromosome folding between tissues and developmental stages. A recent study in *D. melanogaster* embryos showed that looping between enhancers and promoters is conserved between developmental stages and they are often associated with paused RNA Pol II, arising before gene activation (Ghavi-Helm et al., 2014). Interestingly, a genome-wide investigation of enhancer-core promoter interactions discovered thousands of enhancers in S2 and ovarian cells have a preference to either one of two classes of promoters. The first type of promoters was associated to housekeeping, and the second to developmentally regulated genes (Zabidi et al., 2015). It is conceivable that this sequence-encoded enhancer to promoter specificity is implicated in TD organization.

Physical domains in *Drosophila* were found to correlate strongly with epigenomic features, including histone modifications, active gene density, replication timing, association with the nuclear lamina, and nucleotide and repetitive element composition (Sexton et al., 2012). Indeed, several types of chromatin were classified through statistical analysis of genome-wide protein binding profiles, thus reflecting the transcriptional activity of each class. A survey of 53 chromatin proteins in *Drosophila* Kc167 cells defined five principal chromatin types that segment the genome into domains that remarkably overlap with TADs and that consist of specific combinations of proteins (Filion et al., 2010; Sexton et al., 2012). There are three repressed and two active chromatin types. HP1 chromatin ("green") corresponds mainly to constitutive heterochromatin associated to Su(var)3-9, HP1 proteins and dimethylated histone 3 on lysine 9 (H3K9me2).

Polycomb (“blue”) domains are enriched in H3K27me₃, and “black” domains are not specifically associated to any of the proteins investigated although it represents more than half of the genome. Active chromatin regions marked with H3K4me₃ can be subdivided into “red” and “yellow” chromatin. The first is associated with cell type-specific promoters and the second type is preferentially marked with H3K36me₃ and associated with promoters of housekeeping genes. The correlation between epigenetic landscape and topological organization strongly suggest transcriptional activity and TAD organization are tightly linked.

Topological domain boundaries

Mammalian TAD boundaries are reported to be enriched in active transcription, housekeeping genes, tRNA genes and short interspersed nuclear elements (SINEs), as well as binding sites for the architectural proteins CTCF and cohesin (Dixon et al., 2012). However, ~85% of CTCF binding sites are found within TADs, and CTCF and cohesin depletion reduce the intensity of intra-TAD interactions without affecting overall TAD location or organization (Seitan et al., 2013; Sofueva et al., 2013; Zuin et al., 2014a). This is consistent with their putative role in mediating enhancer–promoter contacts within TADs but leaves open the question of their role at boundaries between TADs.

A recent high resolution Hi-C study revealed that looping interactions between CTCF sites and TAD borders depended on the orientation of the CTCF binding motif (Rao et al., 2014). This study identified smaller contact domains within TADs, in the order of 100–200 kb, containing multiple specific loops that occur between CTCF sites in a predominantly (>90%) convergent orientation. Such preferential interactions led to the hypothesis that boundary-boundary interactions established by architectural proteins such as CTCF would induce looping that would physically isolate loci within the loop from loci out of the loop (Crane et al., 2015; Downen et al., 2014; Rao et al., 2014). Consistent with this model, strong TAD boundaries enriched for cohesin were identified as sites where CTCF is highly conserved between mammalian species (Vietri Rudan et al., 2015). Alternatively, a predictive physical model of the chromatin fiber suggested that some TADs represent domains of probabilistic interactions between the sequences lying within them, rather than stable looping structures (Giorgetti et al., 2014).

TAD boundaries in *Drosophila* are highly enriched in active genes and in architectural protein binding sites (see below) (Hou et al., 2012; Sexton et al., 2012). Unlike mammals, however, numerous DNA binding architectural proteins, including CTCF, have been identified in *Drosophila*, each recognizing a unique DNA motif (Le Gall et al., 2015). There are also multiple accessory proteins, in addition to cohesin, that can associate with these DNA binding proteins. The combinatorial binding of these proteins could then underlie a mechanism for TAD border segregation. In this context, a genome-wide analysis of border strength in *Drosophila* Kc167 cells found protein occupancy correlated with the efficiency of contact depletion between adjacent TADs (Van Bortle et al., 2014). Li et al. performed heat shock, which induces general repression of transcription. It resulted in relocation of architectural proteins from TAD boundaries to the TAD interior and increased inter-TAD contacts between enhancers and promoters of silenced genes (Li et al., 2015). This study proposed that TADs may be dynamically remodeled upon external stimuli, and that architectural proteins could play a role in the stabilization if not establishment of TAD barriers.

1.3 Architectural proteins in *Drosophila*

Many of *Drosophila* architectural proteins (or chromatin insulator proteins) were originally characterized by their binding to chromatin insulators, which are gene regulatory elements involved in transcription regulation through the establishment of long range interactions (LRIs) (Le Gall et al., 2015). Five families of insulator binding proteins (IBPs) with specific DNA-binding motifs had been initially studied. These include Suppressor of Hairy-wing [Su(Hw)], Zeste-white 5 (Zw5), GAGA factor (GAF), the boundary element-associated factor (Beaf-32), and dCTCF – the *Drosophila* homolog of mammalian CTCF.

Each IBP binds thousands of sites genome-wide with a specific distribution, suggesting that different insulators may be involved in the regulation of distinct developmental programs (Bartkuhn et al., 2009; Bushey et al., 2009; Nègre et al., 2010; Wood et al., 2011). Furthermore, insulators are involved in transcription regulation of distinct gene ontologies. Consistent with their significant enrichment at TD barriers, IBP binding sites strongly correlate with borders of chromatin epigenetic domains (chromatin colors).

Genome-wide studies in cultured cells and embryos showed that dCTCF, Su(Hw) and Beaf-32 possess partially redundant localization patterns (Bushey et al., 2009; Emberly et al., 2008; Nègre et al., 2010), suggesting that the locus-specific composition of insulator complexes may play a role in their function (Van Bortle et al., 2014). Beaf-32 and dCTCF sites were found to be specifically enriched close to promoters, transcription start sites (TSS) and transcription end sites, contrasting to the distribution of Su(Hw) binding sites that are enriched in or near heterochromatic regions (Vogelmann et al., 2011).

Most insulators share the common Centrosomal Protein 190 (CP190) and/or one of the Mod(mdg4) isoforms as co-factors. CP190 is a protein found only in *Drosophila* and was originally described for its ability to bind to the centrosome during mitosis (Oegema et al., 1995). CP190 also plays a central role in the insulation function of various IBPs. A large proportion of CP190 binding sites (~50%) correlate with the presence of Beaf-32, and both factors are enriched at borders between TADs (Bushey et al., 2009; Nègre et al., 2010; Van Bortle and Corces, 2012). Another factor, Chromator (also known as Chriz/Chro), was also recently found to be overrepresented at those borders shared by Beaf-32 and CP190 (Sexton et al., 2012). Chromator forms a molecular spindle matrix during mitosis, localizes to inter-band regions of polytene chromosomes, and plays a role in their structural regulation as well as in transcriptional regulation during interphase through interaction with chromatin remodeling factors such as Jil1 kinase (Rath et al., 2006).

Recently an *in vitro* study showed the ability of CP190 to establish interactions involving pairs of DNA molecules bound by Beaf-32. Importantly, Beaf-32 alone was not sufficient for these interactions to take place (Vogelmann et al., 2014). These results were confirmed in a genome-wide study, which demonstrated the importance of CP190 in mediating LRIs through recognition of IBPs (Liang et al., 2014).

Overall, these studies support the hypothesis that architectural/insulator proteins play an important role in the establishment of interphase chromatin organization.

1.4 What mechanisms for TAD formation?

The mechanisms that define chromatin topology and their impact on gene regulation are yet to be defined. Chromatin adopts a multilevel architecture that could possibly be described by fractal geometry. Indeed, preferential long-range chromatin contacts have been observed at different length-scales ranging between kilobases and several megabases. Transcriptional activity emerges as a key process affecting genome organization during interphase. The transcription “potential” reflected by the combinations of epigenetic marks and DNA-binding proteins seems to be a driving force in the establishment of homotypic interactions between regions of similar activity. While TADs represent a dynamic and yet reproducible conformation of genomes, it is to be determined how the scope of preferential contacts is confined. Insulator binding proteins are abundant on TAD boundaries and their capacity to establish long-range chromatin contacts promoted a model in which domain borders cluster in space to limit inter-TAD interactions. The principal aim of this thesis project was to establish an experimental strategy to test the border interaction hypothesis and provide new evidence for the role of insulators in chromatin organization.

Chapter 2

Super-resolution microscopy concepts and applications

Super-resolution microscopy breaks the diffraction limit of light, making it possible to visualize a broad range of subcellular components with nearly molecular scale detail. The potential of this powerful tool is continuously growing since the implementation of optical configurations and data analyses compatible with the technically challenging, yet frequent in biology, thick and crowded samples. In this chapter I review the principles underlying stimulated emission depletion (STED), structured illumination microscopy (SIM), and single-molecule localization microscopy (SMLM) approaches, and their technical developments, with an emphasis on three-dimensional and live-cell imaging. Special attention is brought to the new requirements for probe efficiency, namely their size and their photophysical properties. Finally, recent applications exploring the interphase nucleus are presented to illustrate the performance of super-resolution techniques.*

* The contents of this chapter have been recently published in the journal *Research and Reports in biology* (Georgieva and Nollmann, 2015).

2.1 Fluorescence microscopy beyond the diffraction limit

Microscopy has long been a valuable tool for visualizing the complexity of biological structures as well as for directly probing the dynamics of biological processes within cells, tissues and organisms. The components of living matter span several orders of magnitude in size, ranging typically from several nanometers for individual proteins to tens of micrometers for a mammalian cell. Various microscopy techniques have been developed for the study of biological questions at these multiple scales. Electron microscopy (EM) is the method offering the highest resolution (\sim nm), and has allowed the detailed study of numerous cellular nanostructures. However, EM does not inform on the identity of molecules building sub-cellular structures and is unsuitable for applications in living systems, excluding the possibility to follow dynamics. Atomic force microscopy (AFM) is a scanning probe method providing high resolution, comparable to that of EM, and can be used for live imaging. Specific structural information can also be obtained by functionalization of the scanning tip, but AFM can only explore the surface of cells.

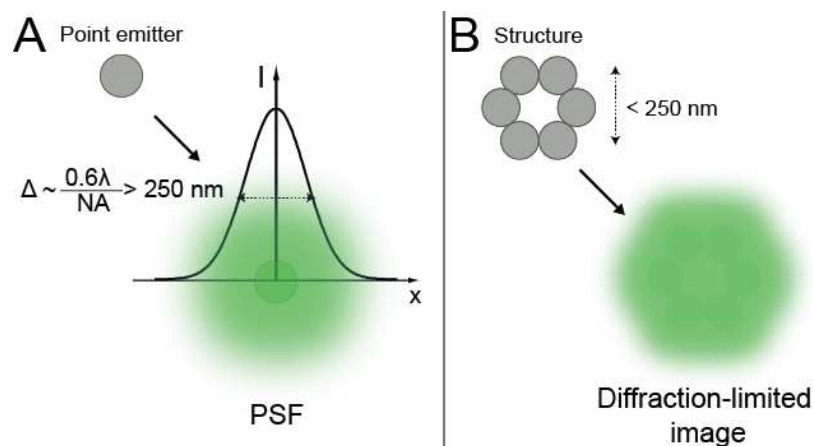
A technique that has been widely used for the specific study of dynamics and localization of intra- and extracellular components in living specimens is fluorescence microscopy (FM). The simplest method for fluorescence imaging is the widefield configuration (ie epi-fluorescence). Diffraction of light within the optical system sets a theoretical bound for the maximal resolution of a fluorescence microscope. The theoretical image of a point source through an optical system is best described by an Airy pattern. In practice, however, aberrations and other factors modify this theoretical profile. The point spread function (PSF) is the real three-dimensional image of a point source obtained through the microscope, and comprises both the effect of diffraction and aberrations of the system (Figure 2.1a). The width of the PSF in the lateral direction is $\Delta \sim \lambda * 0.6/NA$, where λ is the wavelength of the excitation light and NA is the numerical aperture of the objective. The resolution of an optical system is defined by the distance at which two point sources in the sample can be resolved in the image plane (Abbe, 1873; Rayleigh, 1896). When the two point

sources are found closer than Δ , their diffraction patterns overlap and the two sources cannot be resolved (Figure 2.1b). Thus, Δ represents the resolution of the optical system and structures smaller than this intrinsic distance cannot be resolved optically. This limit in resolution prevented scientists from visualizing the structures and processes happening below that scale-length. Confocal microscopy is a widely spread optical configuration which compared to epifluorescence improves contrast by discarding the detection of out of focus light using a pinhole (a small aperture) in the confocal image plane of the light path. The sample is illuminated with a focused spot of laser light and images are constructed pixel-by-pixel by raster scanning. The sizes of the spot PSF and the pinhole determine the diffraction-limited resolution of the constructed image, typically 200-300 nm in the lateral and \sim 500-700 nm in the axial directions.

Given the aforementioned advantages of FM, a major direction for instrumental development has been to beat the diffraction limit of light and increase resolution up to that of EM. In the past decade three classes of techniques that allow subdiffraction fluorescence imaging have been implemented, developed and commercialized (Cox, 2015; Fornasiero and Opazo, 2015; Habuchi, 2014; Schermelleh et al., 2010). Stimulated emission depletion microscopy (STED) is based on a confocal system and reaches subdiffraction resolution by decreasing the size of the detected PSF. This is achieved by selectively turning off molecules found away from the center of the excitation beam (Müller et al., 2012; Neupane et al., 2014). Structured illumination microscopy (SIM) is a widefield technique that beats the diffraction limit by illuminating the sample with patterned light, thus allowing the microscope to transmit higher spatial frequencies, *i.e.* finer sample structures, than allowed by the Abbe limit (Allen et al., 2014). Single-molecule localization microscopies (SMLM) access the precise positions of individual fluorophore molecules and use them to reconstruct high resolution images (Manley et al., 2011; Patterson et al., 2010; Sauer, 2013; Sengupta et al., 2012). Over the past few years, studies applying super-resolution microscopy (SRM) have revealed these three approaches have their specific advantages and drawbacks, suggesting their potential complementarity in unraveling nanoscale biological processes. A valuable comparative overview of SRM methods characteristics and performance, including, light sources, spatial and temporal resolution, and limitations has been provided in Schermelleh et al (Schermelleh et al., 2010).

Here we review the principles and fundamental advances in SRM methods and discuss their live-cell imaging and probes requirements. We then highlight diffraction unlimited quantitative microscopy studies that have allowed to gain unprecedented detailed insight into the structure and inherent dynamics of fine cellular components in the nuclear compartment.

Figure 2.1 - Resolution in conventional fluorescence microscopy



(a) Light emitted by a point source (fluorescent protein or organic fluorophore) is detected by the optical microscope as a PSF of width which depends on the wavelength of emission and the light collection capacity of the objective. **(b)** The diffraction of light limits the resolution of the system such that emitters closer than the width of the PSF cannot be resolved, leading to a loss of structural detail.

2.2 Technology overview of super-resolution imaging

2.2.1 Stimulated emission depletion (STED)

The first technique that has achieved subdiffraction resolution fluorescence imaging is STED microscopy. STED was theoretically introduced in the 1990s (Hell and Wichmann, 1994) and experimentally demonstrated in 2000 (Klar et

al., 2000). This method relies on the photophysical phenomenon formalized by A. Einstein termed stimulated emission. When a fluorophore in its excited state is illuminated, it can return to its ground state through emission of a photon with the same energy as the stimulating photon.

In STED microscopy, subdiffraction resolution is obtained by shrinking the effective PSF of the diffraction-limited excitation spot in a confocal setup (Figure 2.2a). Stimulated emission is used to deplete the population of excited fluorophores that are located at the periphery of the excitation spot. Selective depletion is achieved by applying a doughnut shaped beam with zero intensity at its center, aligned with the center of the excitation beam. The excitation laser has a wavelength near the absorption maximum of the fluorophore used for sample labeling, and the depletion laser has a longer wavelength than the fluorophore maximum emission wavelength. Thus excited fluorophores found within the minimum of the doughnut will emit at the natural emission wavelength and those outside will emit at the depletion laser wavelength. The resolution of the system is increased when the size of the doughnut hole is reduced by increasing the depletion laser power. In biological samples, resolutions up to 20 nm have been reported (Göttfert et al., 2013). The spatial resolution of a STED microscope is strongly dependent on the quality of the depletion beam profile which will define the shape and size of the STED excitation spot. Improving the spatial resolution requires a finely tuned depletion beam and a perfect alignment with the excitation line.

According to the excitation and depletion schemes used, there are several designs of STED microscopes, namely with pulsed, continuous wave (CW) and two-photon laser sources. Pulsed-mode STED (p-STED) achieves the highest resolution, and requires synchronization of the excitation and depletion laser pulses (Klar and Hell, 1999). To detect non-depleted fluorophores either the timing (Hell and Wichmann, 1994; Klar and Hell, 1999) or the lifetime information (Moffitt et al., 2011; Vicidomini et al., 2011) is used in p-STED. Using CW lasers for both excitation and depletion simplifies the setup since no precise time delays between laser pulses are needed (Willig et al., 2007). However, the resolutions achieved are lower compared to p-STED. Two-photon excitation has been combined with STED (Moneron and Hell, 2009) both in the pulsed and the CW modes in order to image thick samples, such as tissue slices, with diffraction-unlimited resolution (Ding et al., 2009; Takasaki et al., 2013).

The different modes of STED microscopy have been widely used for both fixed and live cells, and applications (Müller et al., 2012; Neupane et al., 2014).

In STED, the use of a doughnut-shaped depletion laser beam improves lateral resolution, but the axial resolution remains that of a confocal setup, since zero depletion intensity is distributed along the optical axis. Subdiffraction axial resolution was achieved by tuning the shape of the depletion beam (Klar et al., 2000; Neupane et al., 2013). Another approach has been to combine STED with either total internal reflection fluorescence (TIRF) (Gould et al., 2011; Leutenegger et al., 2012) or with a 4Pi microscope configuration. In TIRF the incident angle of the excitation light is highly inclined to obtain an evanescent wave with exponential decay, which restricts excitation to a thin region of 100-200 nm above the surface of the coverslip. TIRF effectively removes out of focus blur, however its use is limited to imaging cellular components near the cell surface. The 4Pi setup uses two opposing objective lenses both focused at the same point. This method improves axial resolution down to ~ 80 nm and can be applied to samples a few micrometers thick, though its implementation is challenging (Gugel et al., 2004; Schmidt et al., 2008).

Multicolor imaging has also been achieved in STED microscopy. The first type of multicolor STED requires an excitation/depletion laser couple per fluorophore (Bückers et al., 2011; Donnert et al., 2007; Meyer et al., 2008), which is technically demanding. Efforts have been made to reduce the number of laser lines by exploiting the spectral properties of both fluorescent proteins and organic dyes (Göttfert et al., 2013; Pellett et al., 2011; Tønnesen et al., 2011; Willig et al., 2011).

2.2.2 Structured illumination microscopy (SIM)

When a fluorescent sample is observed with an optical microscope, the structure is blurred in the resulting image due to the diffraction of light (Figure 2.2b). In other words, features of a sample smaller than ~ 200 nm in the lateral and ~ 700 nm in the axial directions could not be transmitted by the optical setup. This is the case of conventional widefield microscopy in which the specimen is illuminated with a nearly homogeneous beam of light. SIM is a widefield configuration capable of doubling the diffraction-limited resolution. In 2D SIM (Gustafsson, 2000), this is achieved by exciting the sample with a line-pattern of

sinusoidally alternating intensity maxima and minima with a frequency at the diffraction limit (Figure 2.2b). For a given orientation and phase of the sinusoidal stripes, the resulting raw image is an interference pattern between the illumination and the sample, and encodes sub-resolution structural information that is filtered by a conventional microscope. A high resolution image is thus reconstructed by mathematical processing of raw images acquired with several directions of the patterned excitation (Allen et al., 2014). Typically, two-dimensional imaging requires nine raw images (three phases along three orientations at 120°).

By modulating the illumination pattern so that it varies sinusoidally in all three directions in space, the third dimension was introduced to SIM (Gustafsson et al., 2008). 3D SIM allows physical optical sectioning with axial resolution of ~ 300 nm. The increased complexity of the excitation pattern requires to image at five different phases so that the resulting data can be mathematically decomposed into the constituting high-resolution parts. To be able to computationally reconstruct a high-resolution 3D-SIM data set, each Z-section requires fifteen exposures (Figure 2.2b). The sections have to be taken not more than 125 nm apart to allow full sampling in the axial direction.

A major disadvantage of SIM with respect to STED and SMLM is the relatively low attainable resolution. It has been shown that, in principle, SIM can reach higher resolutions if the fluorescence response is no longer linear, by saturating fluorophores in the excited state (Heintzmann et al., 2002). The concept was applied in saturated SIM (SSIM) with lateral resolution of ~ 50 nm using fluorescent beads (Gustafsson, 2005). The high laser intensities required in this approach make its application in biological imaging challenging. An alternative to obtain non-linearity is the use of reversible on-off transitions of a specific class of fluorescent probes. SSIM with the photoswitchable protein Dronpa allowed ~ 60 nm resolution imaging of nuclear pores in extracted nuclei using the TIRF mode (Rego et al., 2012).

The relatively large number of acquisitions per plane (~ 15) in SIM can lead to photobleaching and sample drift during the acquisition. These effects can severely degrade performance and produce reconstruction artifacts. To reduce these shortcomings, it is important to correctly match the refractive indices, increase labeling contrast, and reduce sample movement during acquisition (either mechanical or biological). Particular attention must be paid when

interpreting structures that are close to the SIM resolution limit as reconstruction at these lengthscales is intrinsically prone to artifacts. SIM has been a popular choice to reveal various cellular structures at higher contrast (Schermelleh et al., 2008). It offers the possibility of fast 3D imaging with most conventional fluorophores as long as they are sufficiently photostable, and is highly convenient for multicolor applications.

2.2.3 Single-molecule localization microscopies (SMLM)

SMLM or probe-based super-resolution imaging is a family of techniques that utilize the particular photophysical properties of a subset of fluorescent dyes to accurately determine their individual positions and thus obtain diffraction unlimited resolution (Patterson et al., 2010). These include photoactivated localization microscopy (PALM) (Betzig et al., 2006), fluorescence photoactivated localization microscopy (FPALM) (Hess et al., 2006), stochastic optical reconstruction microscopy (STORM) (Rust et al., 2006), and direct stochastic optical reconstruction microscopy (dSTORM) (Heilemann et al., 2008). Unlike STED and SIM, which tune the illumination pattern to improve imaging resolution, SMLM employs a classical widefield configuration. The principle of SMLM methods relies on the possibility to localize a single point source of light by fitting its PSF with a Gaussian or Lorentzian function. The precision of localization is dependent on the number of photons emitted by the molecule, the background, and the width of the PSF (Thompson et al., 2002). An underlying condition is a low probability of emitter overlap, i.e. only a small subset of fluorophores is to be emitting in the same time over the field of view (Figure 2.2c). This is achieved either using photoactivatable proteins that are reversibly/irreversibly turned on (PALM/FPALM), or through reversible stochastic photoswitching of organic dyes in the presence of a reducer in oxygen-depleted medium (STORM/dSTORM). The amount of simultaneously emitting molecules can be controlled by modulating the intensities of an excitation laser (typically in the visible spectrum) which serves to image and turn off (or photobleach) the fluorophores. In addition, a lower wavelength laser is used to re-populate the excited state through dye-dependent mechanisms (Dempsey et al., 2009; Heilemann et al., 2005; Zhou and Lin, 2013). STORM relies on pairs of activator and reporter dyes coupled to the same probe molecule. The activator dye absorbs at the activation laser wavelength and facilitates the activation of the

reporter dye through energy transfer between adjacent molecules. The activated reporter dye absorbs light from the excitation laser and its emission position is localized. In contrast, dSTORM makes use only of the absorption properties of the reporter dye. It is worth mentioning that both methods use similar activation/excitation schemes and imaging buffer composition.

Localization precision in SMLM is in the range of $\sim 10\text{-}30$ nm, and can be improved using brighter probes. However, the smaller the uncertainty in the emitter position, the higher the fluorophore labeling density required to effectively increase the structural resolution (van de Linde et al., 2010). According to the Nyquist sampling theorem, the average distance between adjacent fluorophores must be twice smaller than the desired resolution. For the evaluation of SMLM image resolution, a Fourier ring correlation method was introduced, with the advantage that no detailed knowledge of the sample is needed for the calculation (Nieuwenhuizen et al., 2013).

For the reconstruction of a high resolution image, the positions of all the detected single-molecule fluorescent events are overlaid, with intensities reflecting both density and localization uncertainty (Figure 2.2c, right). To collect a sufficient amount of localization data, most often tens of thousands of frames are needed for biological samples. The long acquisition times, typically lasting tens of minutes, lead to non-negligible sample drift. In the axial direction drift is corrected during acquisition with an auto-focus feedback system. Lateral drift is corrected during post-processing thanks to fiducial markers added to the sample or using spatiotemporal cross-correlation of localizations (Wang et al., 2014b).

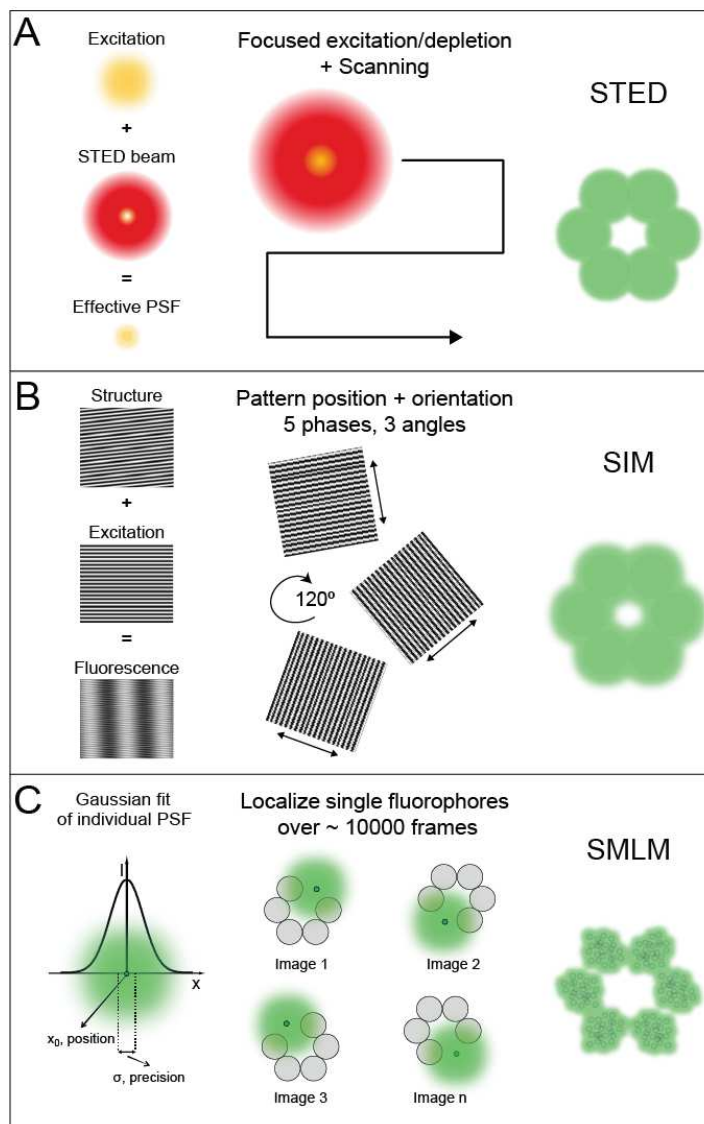
The first studies of SMLM were performed in the TIRF mode, which limits the depth of excitation, achieving subdiffraction resolution in all three directions (Betzig et al., 2006; Hess et al., 2006; Rust et al., 2006). However, to image structures located further than ~ 200 nm above the coverslip surface several optical and computational techniques have been developed to obtain axial localization information (3D-SMLM). Three categories of 3D-SMLM methods can be distinguished: interferometric approaches, including 4Pi, also used in 3D STED and 3D SIM configurations (von Middendorff et al., 2008), multiple plane imaging (Ram et al., 2008), and PSF engineering. The last category breaks the symmetry of the PSF, thus the axial position of fluorophores can be determined using calibration curves. A widely used approach is the introduction of astigmatism in the microscope emission path either with a cylindrical lens (Huang et al., 2008),

or with adaptive optics which in addition allow optical aberrations correction (Izeddin et al., 2012). Axial resolutions reported with this method have reached ~ 50 nm within a range of ~ 750 nm. Alternatively, higher probing depth has been obtained by double-helix shaping of the PSF (~ 1.5 μm) with similar axial resolution (Pavani et al., 2009). Isotropic resolution of ~ 10 - 15 nm with a 3 μm axial range was achieved with the self-bending PSF method (Jia et al., 2014). A detailed overview of 3D SMLM approaches as well as a critical assessment of their performances and applicability has been recently provided by Hajj et al (Hajj et al., 2014).

A further improvement of SMLM has been the optical sectioning capacity. Thick samples, such as whole cells (up to ~ 10 μm above the coverslip surface) and 3D cell cultures (50 - 150 μm deep) have been imaged combining 3D PALM with two-photon activation (York et al., 2011) and light-sheet microscopy (Cella Zanacchi et al., 2011; Hu et al., 2014) respectively.

The development and characterization of new photoswitchable proteins and organic fluorophores with different spectral and photophysical properties favored the multicolor extension of SMLM (Chozinski et al., 2014; Dempsey et al., 2011; Patterson et al., 2010; Shcherbakova et al., 2014). Thus the relative distribution of various molecular assemblies and cellular structures in both fixed (Bates et al., 2007a; Shroff et al., 2007) and live (Klein et al., 2012; Subach et al., 2009; Xu et al., 2013) cells have been revealed with remarkable detail.

Figure 2.2 - Super-resolution microscopy techniques



From left to right: principles underlying detection for each method, acquisition schemes, resulting images. **(a)** - In STED, a depletion doughnut-shaped beam is combined with the focused excitation light, thus decreasing the size of the PSF to a volume smaller than the diffraction limit (Left). Acquisition (Middle) is performed by scanning the two perfectly aligned light sources over the sample with the emitted light collected pixel by pixel by a detector (PMT or APD). **(b)** - In SIM the excitation of a structure with non-uniform light pattern results in an upshift of the sample spatial frequencies, resulting in Moiré fringes (Left). 3D SIM acquisition (Middle) is performed by laterally displacing the illumination pattern (5 phases) in 3 orientations (angles) of the sinusoidal stripes, and spatially modulated images are recorded by a CCD camera. **(c)** - In SMLM the position of individual emitters is obtained by fitting of their intensity profile detected by a CCD camera (Left). The acquisition (Middle) relies on the low density of emitting fluorophores ($< 1/250$ nm). The single localizations are then combined to reconstruct the super-resolved image (Right).

2.3 Live-cell imaging

A notable strength of fluorescence microscopy is the possibility to directly probe biological processes in living samples. This allows not only to visualize biomolecules in their nearly natural environment, but also to study the dynamics and structures of biomolecular factors, their interactions, and their transport. The high contrast, specificity and sensitivity, the relatively low invasiveness and versatility of the labeling have contributed to the establishment of fluorescence microscopy as a method of choice for live-cell imaging. However, the time scale of a large number of cellular events is such that it remains technically challenging to obtain sufficient temporal resolution while preserving the sensitivity of detection and the survival of the specimen (Stephens and Allan, 2003). The challenge is even greater when in addition high spatial resolution is needed to study smaller than the diffraction limit cell components with inherently low molecular density. In this context, the performance of fluorescence microscope configurations for a given live-cell experiment is to be evaluated by taking into account the imposed trade-offs in imaging parameters, namely acquisition speed, spatial resolution, imaging depth, and the extent of light-induced photodamage, affecting both the fluorescent probe and sample viability. For instance, improving the temporal resolution demands a faster imaging rate, hence shorter exposure times for excitation. The result is a lower fluorescence signal which affects the attainable spatial resolution regardless of the super-resolution technique employed. Consequently, laser power is to be increased for better signal detection, leading to phototoxicity, which generates a risk of artifactual observations.

In practice, SRM methods, while having their specific weaknesses and strengths, have been successfully applied for the study of nanoscale-sized dynamic biological phenomena with imaging speed of tens of frames per second (fps). SIM offers the highest acquisition rates and reduced photodamage compared to STED and SMLM (10^3 - 10^6 times lower light exposure), although spatial resolution is limited. Both fast imaging (28 fps) and high resolution (62 nm) have been achieved in STED in a molecularly crowded environment (Westphal et al., 2008). However, phototoxicity due to the elevated laser powers required to reach high spatial resolution remains a major limitation for live-cell imaging with STED. The

photon charge applied on the sample was significantly reduced with a STED variant which uses fluorophore photoswitching in line with the concept of reversible saturable optically linear fluorescence transitions (RESOLFT) (Hofmann et al., 2005). The imaging speed was further increased as RESOLFT was combined with multiple doughnut beams to scan the sample simultaneously (Chmyrov et al., 2013).

SMLM is intrinsically slow since accurate localization of individual fluorophores requires that only a sparse subset of emitters is fluorescent in each frame within a diffraction-limited spot. Thus, a large number of frames are needed for image reconstruction, which limits the temporal resolution. However, SMLM is able to access single-molecule information, making it an attractive technique to obtain quantitative information on protein numbers and dynamics. The development of high density localization algorithms (Holden et al., 2014; Huang et al., 2013; Zhu et al., 2012) led to a considerable decrease in acquisition time.

2.4 Probes for super-resolution imaging

Specific identification of molecules within biological samples with low invasiveness and high imaging contrast are the hallmarks of fluorescence microscopy. However, depending on the fluorescent probe and the individual requirements of the imaging technique, particular attention must be paid during sample preparation and the acquisition procedure to avoid potential artifacts.

2.4.1 Molecular tags

Specificity in fluorescent labeling is obtained either with genetically encoded tags fused to the molecular target or with affinity probes. The former strategy allows the labeling of proteins, the tag size is relatively low (~ 25 kDa) and it is live-cell compatible. Fusion protein labels can be either intrinsically fluorescent, i.e. the well-known GFP and its variants, or coupled to a fluorescent dye by covalent enzyme-ligand binding, such as the commercially available SNAP-tag (~ 20 kDa) (Gautier et al., 2008). When introducing tagged proteins in a biological specimen, cell physiology may be altered by overexpression, aggregation, mistargeting, misfolding and perturbation of protein function, which constitute the main

limitation of this labeling approach in conventional microscopies, and to an even greater extent at subdiffraction resolution. A powerful solution is the use of knock-in strategies, providing endogenous expression levels, especially when protein quantification is intended as in most PALM applications (Specht et al., 2013).

Biological structures can alternatively be tagged with affinity probes, among which antibodies are the most widely spread. Antibodies are an accessible, versatile tool, which allows direct specific labeling of endogenous epitopes. They are particularly useful to target, among others, post-translational protein modifications (phosphorylation, ubiquitination, sumoylation, *etc.*), and even to recognize methylation sites on DNA. Whereas diffraction-limited microscopy is insensitive to the large dimensions of antibodies (~ 150 kDa/ ~ 15 nm) allowing secondary antibody labeling, in super-resolution imaging (SMLM in particular) probe size becomes a parameter potentially limiting the achievable structural resolution. Consequently, primary antibody monovalent fragments (Fab, ~ 50 kDa) or the naturally occurring single-chain camelid antibodies (also named VHHs or nanobodies, ~ 15 kDa) are a promising development (Ries et al., 2012a), though their availability is still limited.

In SRM, a non-negligible aspect of intracellular components visualization with affinity probes is the requirement for sample fixation and permeabilization. These processing steps inevitably introduce alterations in the specimen, and structural preservation is critical for properly interpreting observations of molecular-scale detail. For instance, insufficient fixation or destructive permeabilization may result in target mislocalization or degradation. In contrast, strong fixation (as practiced in EM) preserves the structures but may also restrain epitope accessibility, thus limiting the labeling density and therefore the achievable structural resolution in subdiffraction imaging experiments. An optimized protocol for SMLM sample preparation has been recently introduced (Whelan and Bell, 2015).

2.4.2 Fluorescent molecules

Imaging contrast (*i.e.* how well the structure of interest can be discriminated from its environment) is a crucial component of fluorescence microscopy, which relies on the performance of fluorescent molecules. Some general parameters for

assessing fluorophores are brightness (calculated as the product of the extinction coefficient and the quantum yield), photostability and water solubility. Recently, an additional property that describes the ability of fluorescent molecules to transit between bright and dark states, termed photoswitching, has become fundamental in super-resolution microscopy applications (Heilemann et al., 2005). The principle of SMLM relies on the detection of single molecules with nanometer precision. Most often this is achieved by separating emission from each single emitter in time by making use of their stochastic photoswitching behavior. In addition, the use of photoswitchable probes has contributed to considerably improve the performance of other super-resolution methods such as RESOLFT and SSIM. Fluorophore photoswitching is usually quantified by the number of switching cycles, the number of detected photons per switching event, the duty cycle (fraction of time a fluorophore spends in an on state), and the on and off switching rates (Chozinski et al., 2014).

The number of switching cycles reflects the number of times an emitter enters the bright state and can be detected. For SSIM, RESOLFT and live-cell SMLM, multiple detections are preferred to construct high resolution images. In contrast, quantification of absolute protein numbers with PALM would ideally benefit from a single switch before photobleaching. In practice though, all known fluorophores display multiple switching cycles that must be accounted for in quantification procedures (Annibale et al., 2011a; Durisic et al., 2014; Puchner et al., 2013; Sengupta et al., 2011; Shivanandan et al., 2014; Veatch et al., 2012). The number of detected photons per switching event (a metric of the photoswitch brightness), and the duty cycle (the fraction of time an emitter spends in the fluorescent state) together determine the spatial resolution achievable in SMLM methods. The former is proportional to the localization precision, while the latter limits the number of fluorophores that may be localized within the volume of the PSF. Finally, the on/off switching rates are one factor limiting the speed of image acquisition and thus the temporal resolution of super-resolution methods employing photoswitchable probes.

According to their origin, fluorophores are of two types: naturally existing in living organisms and subsequently genetically engineered (fluorescent proteins), and chemically synthesized (organic dyes). In the context of super-resolution imaging, specific advantages of each category impact on the labeling strategy. Typically, the duty cycle of photoswitchable fluorescent proteins (FPs) tends to be

lower than organic fluorophores, and allows imaging of densely labeled structures. In addition, FPs label proteins with a controlled stoichiometry of 1:1, crucial in quantification experiments, whereas organic fluorophores are generally coupled to affinity probes, for which labeling efficiency is difficult to evaluate. In contrast, organic dyes display superior brightness and photostability this allowing higher localization precision. They are available in a broader variety of absorption/emission spectra spanning the visible and importantly the near infrared wavelengths, which makes them convenient for multicolor experiments. While FPs do not require a particular composition of the imaging medium in SMLM experiments, photoswitching of organic fluorophores has been initially obtained by depleting oxygen in the imaging buffer and by addition of a reducer (thiol), toxic for cells. Eventually, the exploration of cell-permeative tags and the optimization of imaging buffers have introduced organic fluorophores in live-cell super-resolution applications (Benke and Manley, 2012; Carlini and Manley, 2013; Carlini et al., 2014; Klein et al., 2011; Lukinavičius et al., 2013; Wombacher et al., 2010).

Several studies provide systematic evaluation of FPs and organic fluorophores for super-resolution applications (Dempsey et al., 2011; Shcherbakova et al., 2014; Wang et al., 2014a). While most fluorophores have been optimized for a single super-resolution technique, probes that display good performance in several of them have been recently developed, such as the photoswitchable proteins Dreiklang (Jensen et al., 2014) and mMaple (McEvoy et al., 2012), which will foster the development of multimodal SRM approaches.

2.5 The nuclear compartment studied with SRM

Since its first implementation, SRM has allowed to get molecular-scale insight into major cellular processes, notably membrane receptor distribution and oligomerization, a critical step in cell signaling (Pageon et al., 2013; Scarselli et al., 2012; Sengupta et al., 2011). With the evolution of optical setups providing the possibility to image thick samples and the improvement of analysis procedures performance in lower signal to noise conditions, structures and phenomena deeper in the specimens have become accessible to quantitative analysis. In this section, we review recent SRM studies that have contributed to enrich our understanding of the organization and functioning of the nuclear compartment. Specifically, we will focus on research performed in interphase chromatin folding and transcription machinery dynamics, two crucial components of gene regulation.

2.5.1 RNAP2 distribution and dynamics

The most regulated step in gene expression is transcription. It involves complex interactions between DNA and trans regulatory elements, the latter including histone modifying enzymes, transcription factors and RNA polymerase (RNAP) complexes. The DNA binding properties and dynamics of nuclear factors are central to the understanding of transcription and have been intensively explored with biochemical assays, or more recently with genome-wide chromatin immunoprecipitation techniques and single-particle tracking (Izeddin et al., 2014). RNAP2, is a well-studied transcription effector, however its nuclear distribution and dynamics at the molecular level had not been directly probed. In particular, quantitative imaging has been lacking essentially due to the relative abundance of RNAP2 in the nucleus and to microscope limitations. Recently, two elegant SMLM studies have provided molecular scale spatiotemporal insight into RNAP2 clustering in mammalian cells (Cisse et al., 2013; Zhao et al., 2014).

Transcription was proposed to take place in RNAP2-enriched foci known as transcription factories, where transcription of multiple loci can be coordinated and potentiated (Papantonis and Cook, 2013). Cisse et al (Cisse et al., 2013) tested this hypothesis by investigating the dynamics of RNAP2 assembly in live

U2OS cells by 2D single-particle-tracking PALM (spt-PALM), a variant of PALM allowing for the study of the assembly and disassembly dynamics of clusters with a size smaller than the resolution limit. Potential labeling artifacts were discarded by engineering a stable cell line expressing a Dendra2-fused catalytic subunit (RPB1), replacing the endogenous RPB1. Pair-correlation analysis (Sengupta et al., 2011) identified clusters of ~ 220 nm, while time-correlated detection counting within individual high density clusters revealed average lifetime of ~ 5.1 s, reflecting the transient nature of RNAP2 clustering. An analogous labeling strategy was used by Zhao and colleagues (Zhao et al., 2014), in which RPB1 was fused to a SNAP-tag and labeled with rhodamine dyes. Localization accuracy and efficiency were improved as STORM imaging was performed in a reflected light-sheet configuration achieving optical sections of $\sim 1\mu\text{m}$. Absolute numbers of RNAP2 molecules were determined through a novel spatiotemporal clustering analysis, which together with co-localization estimated that the majority ($>70\%$) of detected foci are composed of single RNAP2 molecules. Quantitative SRM has thus brought arguments against a pre-assembled, stable organization of transcription sites in the nucleus.

2.5.2 Chromatin organization and dynamics

It is well established that gene regulation and cell fate determination depend on the spatial organization of DNA. Until recently, endogenous genome folding could only be addressed through genetic or biochemical methods (Dekker et al., 2013; Sexton and Cavalli, 2015a), since nuclear substructures are typically smaller than the resolution limit of conventional optical microscopes. From this perspective, SRM is well suited to provide physical maps of gene regulation processes at molecular resolution and reveal subnuclear structures in situ.

The genetic material in eukaryotes is packed within the nucleus in the form of a nucleoprotein complex termed chromatin. The structural unit of chromatin is the nucleosome, composed of an octamer of the highly conserved histone proteins (H2A, H2B, H3, and H4) and 1.7 turns of the DNA molecule. Hence, fluorescent tagging of chromatin can be performed by labeling the core histone proteins, or directly the DNA (Flors, 2011). The former implies the use of immunofluorescence or protein fusions as discussed above. For instance, dihydrofolate reductase (eDHFR) and SNAP-tag fusions have been used for live-

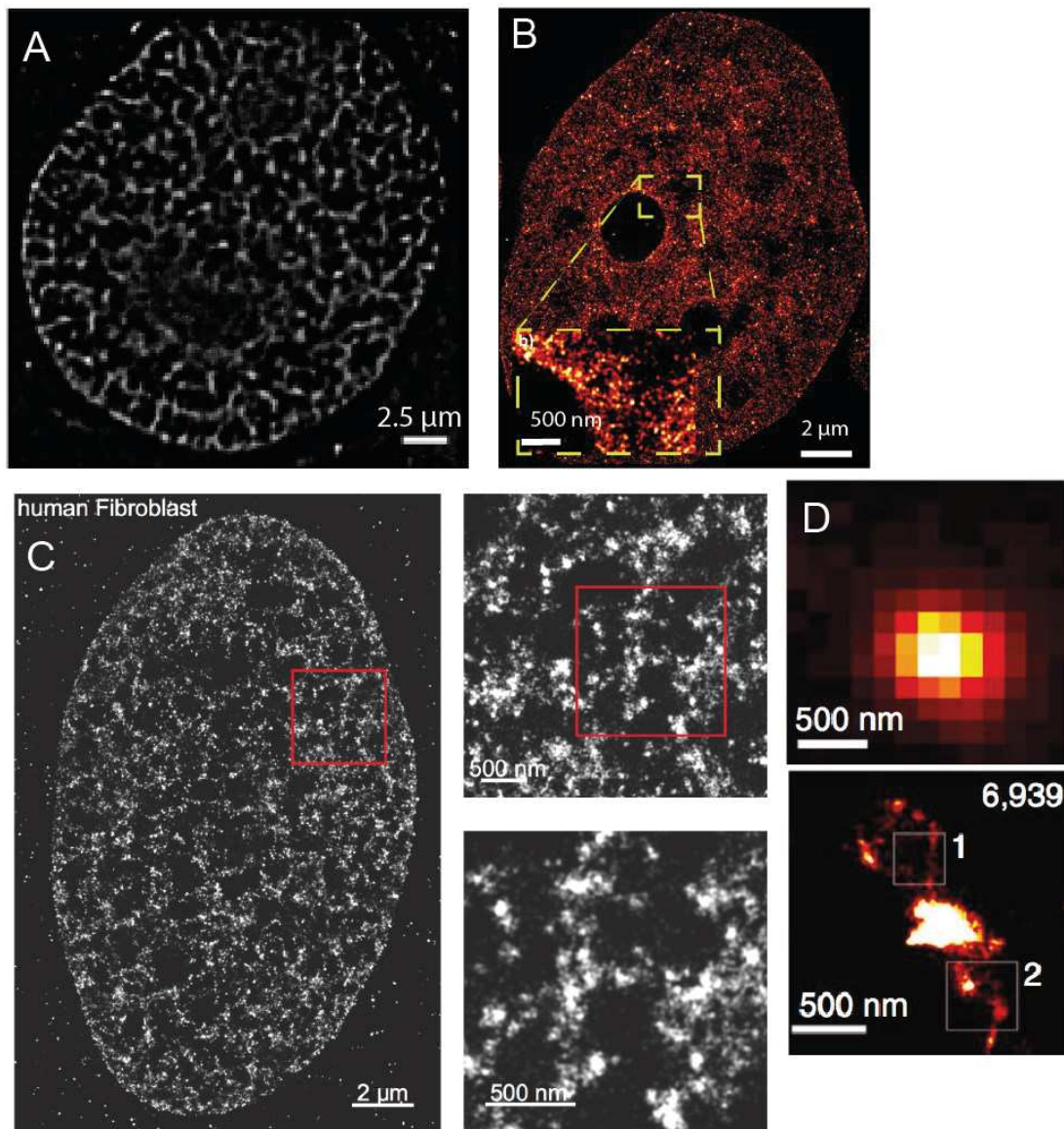
cell STORM imaging of the histone H2B in mammalian cells, potentially allowing to study chromatin dynamics *in situ* (Klein et al., 2011; Wombacher et al., 2010). The second strategy takes advantage of a large variety of intercalating dyes available for sequence-independent DNA labeling. Some of them display SMLM-compatible blinking characteristics and have been successfully used for STORM imaging, namely YOYO-1 in DNA extracts (Flors, 2010; Flors et al., 2009) and more recently PicoGreen in live cells (Benke and Manley, 2012), (Figure 2.3a). Furthermore, incorporation of modified nucleotides using the DNA replication machinery combined with click chemistry fluorescent labeling was employed for the visualization of nascent DNA fragments in live HeLa cells with STORM (Zessin et al., 2012), (Figure 2.3b). Another SMLM approach using the DNA binding kinetics of intercalating dyes rather than blinking is Binding-activated localization microscopy (BALM) (Schoen et al., 2011). Alternatively, DNA can be stained in a sequence-specific manner through the Fluorescence *in situ* Hybridization (FISH) assay. However, ultrastructural preservation is a major concern in FISH experiments, particularly at enhanced resolution. Adapted protocols have been designed for SIM (Markaki et al., 2012) and will likely be applicable to the higher resolution techniques STED and SMLM. Furthermore, a systematic evaluation of the different histone or DNA labeling strategies performance in SRM will allow the newly observed structural details of chromatin organization to be validated (Figure 2.3).

The global chromatin folding drastically changes throughout the cell cycle, from the ~ 500 nm thick and highly compacted chromosomes with characteristic shape in mitosis, to the decondensed ~ 10 nm chromatin fiber in interphase. These orders of magnitude structural variations represent a specific challenge in super-resolution experiments. In mitosis, the high density of DNA and histones is an obstacle to efficient labeling, and sample thickness deteriorates the signal to noise ratio due to out of focus light.

Interphase chromatin, on the other hand, adopts a loose conformation heterogeneously spreading throughout the entire nuclear volume, resulting in low contrast in SIM and STED images or low localization event numbers in SMLM. Several groups have investigated chromatin heterogeneity and reorganization by labeling core histone proteins in mammalian cells under normal cell growth conditions, comparing differentiation states, and upon physiological stimuli. In an early study, Gunkel *et al.* (Gunkel et al., 2009) applied an SMLM variant, namely

Spectral Precision Distance Microscopy (SPDM) in two colors to investigate nuclear distributions of mRFP1-fused H2A and the GFP-fused chromatin remodeler Snf2H in transiently transfected U2OS fixed cells. Counting the number of neighbors in a 300 nm radius showed non-random distributions for both factors, with nuclear regions depleted in H2A, sites of local enrichment of Snf2H, and a partial colocalization of the two proteins. Subsequently, a radial distribution function was calculated to quantitatively explore H2B-GFP localizations with 2D SPDM (Bohn et al., 2010), uncovering chromatin nanostructures on a scale <100 nm. The authors introduced compressibility measures to compare large scale structural fluctuations with polymer models, which indicated non-random chromatin distributions even on the micrometer range. Remarkably, significant differences of H2B distribution depended on the expression method, highlighting the crucial importance of proper fusion proteins targeting. Deeper investigation of H2B non-homogeneity at the nanometric lengthscale in the nuclei of fixed U2OS cells was performed using 3D PALM (Récamier et al., 2014). The Ripley $K(r)$ statistics of H2B-Dendra2 indicated clusterization without specific size in the range of 10 nm to 1 μ m, compatible with the fractal globule model proposed by chromosome conformation capture (Hi-C) (Lieberman-Aiden et al., 2009) and FISH studies (Sachs et al., 1995), and supporting the idea that chromatin organization is influenced by inter-loci contacts. Live-cell imaging of H2B-PAGFP further revealed that this organization is highly transient (Récamier et al., 2014). More recently, secondary antibody immunostaining combined with 2D-STORM (Figure 2.3c) was used to follow the endogenous H2B heterogeneity throughout differentiation in human and mouse cells (Ricci et al., 2015). The super resolved images indicated that H2B is distributed in discrete nanodomains throughout the nucleus, and clustering analysis of raw detections confirmed the lack of a characteristic size of nucleosome-enriched domains. The number of histone molecules per nanodomain was extracted using a calibration curve of H2B localizations densities, which were measured *in vitro* for nucleosome arrays of known length. Nucleosome density and number correlated with the pluripotency grade, indicating that differentiation leads to an increase in domain compaction. Interestingly, computer simulations showed the observed H2B heterogeneity can be explained by the incomplete nucleosome occupancy of the DNA fiber.

Figure 2.3 - Chromatin labeling strategies for single-molecule localization microscopy



(a) - 2D Live-cell dSTORM of DNA in U2OS cells based on direct DNA labeling with Picogreen. Note the sparser distribution obtained here compared to the rest of the images, which may be due to incomplete labeling or detection (Benke et al. 2012). **(b)** - 2D dSTORM of fixed HeLa cells labeled with EdU-Alexa Fluor 647. (inset) Magnification of a region of interest (Zessin et al. 2012). **(c)** - 2D STORM of H2B in an immunostained hFb. Progressively higher zooms of the regions inside the red squares are shown next to each nucleus (Ricci et al. 2015). **d** - Sub-diffraction and super-resolution image of the Bithrorax complex domain using oligoPAINT (Beliveau et al. 2015).

In addition to SMLM, other super-resolution methods have been applied to investigate chromatin structure. The transient organization of chromatin was probed with STED in immunostained rat cardiomyocytes, where pixel intensity levels accounted for the local densities of molecules (Mitchell-Jordan et al., 2012). Induction of hypertrophy, known to cause massive gene expression changes, resulted in multi-level redistribution of endogenous H3. Furthermore, SIM imaging of the β -globin locus with FISH in mouse erythroid cells allowed following of chromatin folding dynamics in opposing transcriptional states (Corput et al., 2012). Size and shape analysis revealed that inactive chromatin explores a wide range of conformations while gene activation resulted in the FISH spot condensation.

Overall, whole genome labeling methods combined with SMLM have provided a glimpse at the complexity in chromatin organization. However, two main drawbacks currently make interpretation of images difficult, and functional studies complicated. The first is the lack of genomic specificity, and the second is the common appearance in the observed structures of collections of protein clusters displaying no clear continuity. Recently, a new approach based on OligoPAINT technologies provided one possible solution to these issues. In this method, thousands of short fluorescently labeled oligonucleotides are used to produce a FISH probe that covers large genomic regions (Beliveau et al., 2012). The application of this method to visualize topological domains has produced impressive super-resolution reconstructions of the Bithorax Complex domain in *Drosophila* (Figure 2.3d) (Beliveau et al., 2015).

2.6 Perspectives in SRM

Super-resolution fluorescence imaging allows visualization of cellular components in the range of 10-200 nm, so far unexplored by diffraction-limited fluorescence microscopies. The optical configurations and analysis methods have undergone significant development over the last few years. However, several important obstacles need to be circumvented for super-resolution microscopies to become widespread.

Super-resolution microscopies are typically more difficult to implement than conventional microscopies, and their results more difficult to assess. Several

important controls have to be performed in the quality of acquisition and analysis in order to ensure an accurate reconstruction. These are usually performed by custom-made software packages. Unfortunately, few tools currently exist that allow for quality controls, and these are often not available to the community. Ideally, future software developments should be made in a common, open-source platform easy to port, validate, and improve. In this respect, much is to be learnt from software development paradigms used by other communities (i.e. CCP4 package for crystallography).

Conventional microscopy can be performed in multi-color due to the large panel of organic and genetically-encoded fluorescent probes available. This is currently not the case for SRM, which is in practice limited to at most two colors or less for live applications on real biological systems. In part, this limitation is due to a general lack of adapted fluorophores. Hopefully, future developments will improve our choice of available dyes. The careful study of dye photo-physics will likely improve our ability to rationally engineer better dyes and devise new acquisition and analysis modes, as well as help characterize novel fluorophores found by screening methods.

Finally, an important limitation of current SRM relies on their poor performance in thick specimens (e.g. embryos, tissues). This limitation is due to the increase in aberrations with the distance to the objective, as well as to the diffusion of light through highly inhomogeneous media. Recent developments using selective plane illumination, adaptive optics and multi-focus microscopy will likely be key to alleviate, at least in part, these important current hurdles.¹²²⁻¹²⁴

Chapter 3

Imaging nuclear structures with multicolor SMLM

Since the early days of cell biology, historical discoveries have come hand in hand with key developments in microscopy techniques. Less than a decade ago, subdiffraction fluorescence microscopies have opened new exciting perspectives for biological imaging. Structures that could not be discerned due to the diffraction limit have become accessible for structural investigation. Super-resolution techniques are growingly performant in terms of instrumentation and analysis methods in the new field of nanoscopy. However, every technological advancement in microscopy has required improvements in sample preparation methods and establishment of robust controls to validate the newly-uncovered structural detail. In this chapter I describe and comment on the experimental pipeline that I have established to perform 2-color SMLM in eukaryotic nuclei, using *Drosophila* S2 cells as model system. First, sample handling procedures are presented and specificities in the context of localization microscopy are highlighted. Next, the selected strategies for image acquisition and processing are detailed. I then introduce an automated quantitative colocalization analysis for localization microscopy and I evaluate its performance through simulations. Finally, I present a quality control method that allows the validation of SMLM images when no prior information on the structure is available.*

* The methods and results presented in this chapter are in the final stages of preparation for publication in the journal *Methods*.

3.1 Sample preparation

SMLM techniques have the potential to reveal subcellular structural features with impressive detail down to the single-molecule level. However, stringent protocols for the sample preparation are required to achieve sufficient ultrastructural preservation and the highest labeling density. The protocol discussed in this section provides the key steps for sample fixation and labeling for multicolor SMLM* imaging of nuclear structures in *Drosophila* cells. With the exception of cell culture specificities, similar considerations are valid for experiments on other systems. Note that the handling and seeding of cells presented below can also be performed on non- or semi-adherent mammalian cell lines.

3.1.1 Cell culture

The first element of any successful imaging experiment is to ensure good cell health. It is critical to continuously monitor cell growth and morphology before starting a labeling procedure. For the trained researcher, a visual inspection with a low magnification microscope is usually enough. The cell culture and seeding procedure on microscope coverslips that I established is detailed below.

1. *Drosophila* S2 cells are grown in Schneider's *Drosophila* medium (Gibco) in 75 cm² cell culture flasks (Nunc) at 25°C.
2. For microscopy experiments confluent cultures are used, from which the growth medium is slowly pipetted out in order to discard floating and dead cells, and importantly, to ensure a reproducible cell density over experiments.
3. For minimal cell stress, fresh medium is added to the flask to resuspend the cells instead of phosphate buffered saline (PBS) from Gibco.
4. Cells are gently detached from the recipient's surface with the help of a cell scraper (Nunc).

* The acronym SMLM is used when the statement is valid for both PALM (using fusion proteins) and (d)STORM (using organic fluorophores and affinity probes).

5. Cells are concentrated by centrifugation at 900 rpm for 3 minutes at 25°C and subsequently resuspended in 2-3 ml of culture medium.
6. 200 μ l of the cell suspension is then deposited as a 10 mm in diameter droplet on 22 mm #1.5 coverslips coated with Poly-L-Lysine (neuVibro, GG-22-1.5-p11). Typically this procedure yields a 50–70 % of cell confluence per field of view (FOV) which is dense enough to result in ~5-10 simultaneously imaged cells, and sufficiently sparse so that the autofocus system based on the reflection of a laser on the surface of the coverslip is not perturbed by an excessive cell density (see Section 3.6.1 for a description of the autofocus system).
7. The seeded cells are then allowed to adhere for 1h at 25°C under regulated temperature conditions as for cell culture. Longer incubation times are not recommended as the low volume of cell medium at this stage may evaporate and change the osmolarity of the liquid and perturb cell physiology. Furthermore, growth on a poly-Lys glass surface may induce cell stress.

3.1.2 Fixation and permeabilization

Microscopic studies of chromatin architecture and nuclear processes such as transcription regulation, DNA damage response and signaling often require direct labeling of DNA or protein post-translational modifications (e.g. phosphorylation, methylation, acetylation, ubiquitinylation and sumoylation, as the most frequently imaged examples). Since these molecular targets are not genetically encoded, the use of fluorescent fusion protein constructs is not adapted, and live-cell imaging cannot be performed. Rather, immunofluorescence (IF) and the fluorescence *in situ* hybridization (FISH) assays are the labeling methods of choice. To fluorescently label the molecular target of interest, cell fixation and permeabilization are required. For cytoplasmic components, a mild fixation procedure is often sufficient to permeabilize the plasma membrane. For nuclear structures though, the integrity of the nuclear envelope must be perturbed as well, and harsher treatments are required.

For fluorescence imaging of the nucleus there are several commonly used fixation protocols, which depend on the cell type, the epitope (structure of interest), and the affinity probe whether it is a protein or nucleic acid. Frequently used reagents

for fixation are formaldehyde, paraformaldehyde (PFA) followed by triton X-100 at room temperature (RT), PFA at RT followed by acetone at -20°C , and methanol at -20°C (Bennett et al., 2009). The concentrations of each reagent and the time of incubation are also adapted to obtain the desired strength of fixation and permeabilization (see below). In cases when very strong fixation is required, glutaraldehyde can be used instead of or in combination with PFA. For optimization purposes, it is critical that the different protocols of fixation and permeabilization are tested in conventional fluorescence prior to super-resolution experiments. Good quality control criteria of the fixation protocol are: preserved cell and nuclear morphology in bright field images compared to live cells, high specific signal strength, and low non-specific fluorescence outside of the nuclear compartment.

For the experiments presented through this thesis, including imaging of transcription factors (RNA Polymerase II), insulator-binding proteins (for example Beaf-32), and chromatin components (histones and DNA) the protocol that I adapted and applied both for IF and FISH is described below:

1. Cell fixation with 4% PFA (Electron microscopy sciences, #15714) for 15 min at RT
2. Cells are next washed three times with PBS for 5 min at RT.
3. Membrane permeabilization with Triton X-100 (Sigma) 0.5% for 5 min at RT.
4. Three PBS washes as in step 2
5. The cells are then directly labeled with fluorescents tags

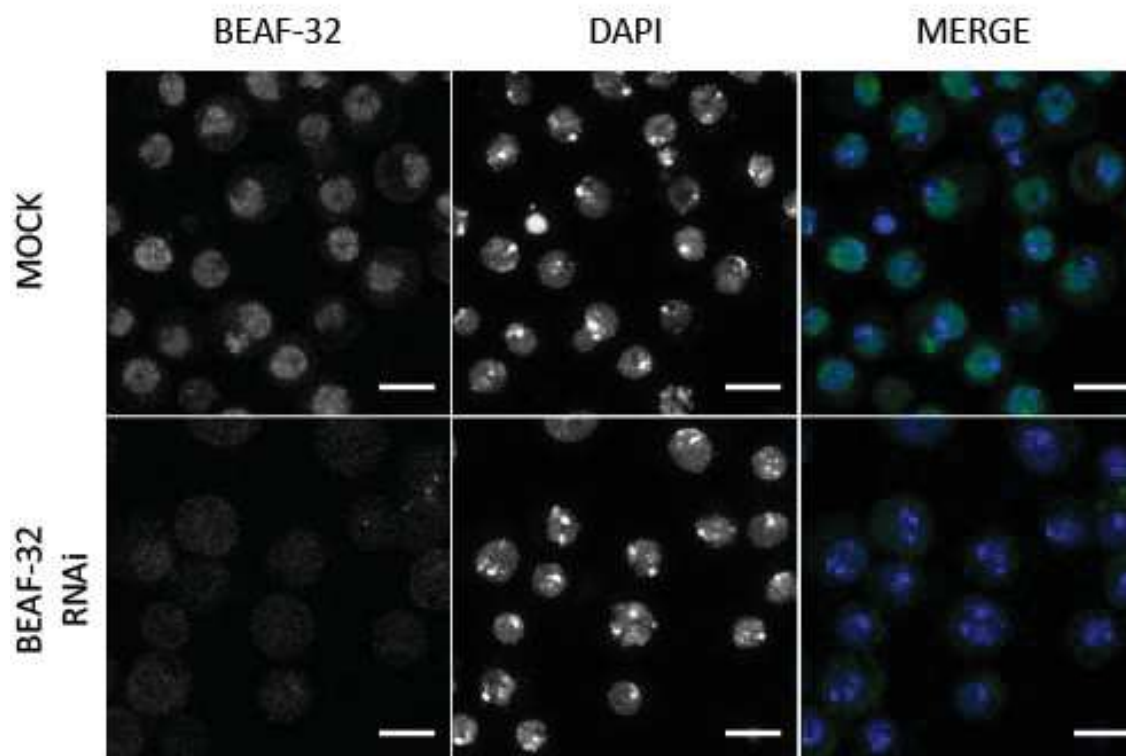
To ensure reproducibility, all the solutions for this and the following sample preparation steps are made fresh prior to each labeling experiment. For optimal quality in dSTORM experiments only freshly fixed and labeled samples should be imaged.

3.1.3 Affinity staining of nuclear targets using antibodies

In fluorescence microscopy applications, it is of crucial importance to use only specific and high affinity antibodies. Western blotting is commonly applied to confirm antibody specificity. An additional control is to knock down the targeted

protein by RNA interference (RNAi) followed by immunolabeling with the tested antibody[†] and by imaging using conventional microscopy. As shown in Figure 3.1, the nearly complete loss of fluorescence in the nucleus of S2 cells treated with RNAi against Beaf-32 is evidence for the good quality of the antibody.[‡]

Figure 3.1 - Control of antibody specificity by RNAi



Immunofluorescence images of BEAF-32 stained with Alexa488 and overlaid with the DNA signal (DAPI). Mock: Untreated S2 cells show a specific nuclear staining. RNAi: BEAF-32 knockdown with RNAi leads to a loss of fluorescence in the nucleus and the whole cell area displays a homogeneous signal.

[†] The references for all antibodies and material for IF are given in the Materials and methods section of chapter 4.

[‡] The non-specific signal observed in the RNAi-treated cells may be due to a very low degree of non-specific binding of the secondary antibody used for microscopy (as compared to the nuclear signal in the mock sample) or reflect the autofluorescence of other cellular components.

The immunofluorescence labeling protocol that I optimized for imaging S2 cells is described below:

1. Blocking of non-specific antibody binding sites with 10% bovine serum albumin (BSA) at RT for 1h. Note that 10 % normal goat serum (NGS) alone or in a cocktail with BSA gave similar results.
2. Three PBS washes.
3. Incubation with the labeled primary antibody (or a mixture of antibodies labeled with different dyes for 2-color experiments) at 4°C for 12-16 h to minimize non-specific binding. For optimal labeling density of nuclear structures I used antibodies at final concentrations of 5–10 µg/ml (see comment in the next paragraph).
4. Three PBS washes.
5. Samples were then immediately mounted for imaging (see Section 3.1.5).

The typical antibody concentrations used in IF protocols are at ~ 1 µg/ml.[§] Most IF experiments make use of secondary antibodies for detection. The intensity of the fluorescence signal is modulated mainly by the concentration of secondary antibody. Instead, to conserve optimal imaging conditions for single-molecule detection, I used primary antibodies. Importantly, the spatial resolution in SMLM is limited by the labeling density of the specimen, which is directly affected by the antibody binding efficiency as discussed in Chapter 2 (p.56). Because labeling density should not be limited by the antibody concentration, I optimized the IF protocol to reach a saturation of the specific sites (5-10 µg/ml). Thus, the density of probes will be limited mainly by epitope accessibility and steric effects between probe molecules. The former is sample-related and difficult to assess or control, the latter is tightly linked to the tag size.

3.1.4 Imaging buffer for dSTORM

When organic fluorophores are used to visualize cell structures with SMLM, the blinking required to achieve single-molecule conditions is obtained through the

[§] Most frequently, only the dilution factor is indicated in publications and not the final concentrations.

chemical environment in the mounting medium. The photoswitching cocktail I used for dSTORM is a slightly modified variant of the frequently used enzyme-based oxygen scavenging system in combination with a thiol as a reducer (Heilemann et al., 2008). Indeed fluorophore photoswitching properties in such buffer are sensitive even to slight changes induced by different imaging conditions (see Section 3.5).

The mounting solution is composed of:

1. PBS
2. glucose oxidase (Sigma) at 2.5 mg/ml
3. catalase at 0.2 mg/ml (Sigma)
4. 10% glucose
5. 50 mM of β -mercaptoethylamine (MEA)

Stock solutions of enzyme mixture at 100X and MEA at 20X are prepared in PBS and stored at -20°C . Note that MEA is unstable and only fresh aliquots are to be used.

The mismatch of refractive index between the objective oil, the coverslip surface and mounting media produces optical aberrations (spherical aberration, coma, astigmatism) that can distort the PSF of the optical system, which in SMLM deteriorates localization accuracy. To overcome this issue, switching buffer variants with Glycerol replacing PBS were used (Bennett et al., 2009), although the high viscosity of the medium strongly reduces the enzymatic activity of the oxygen scavenging system yielding poor photoswitching dynamics and therefore resolution. The commercial mounting medium Vectashield has been shown to allow efficient photoswitching of AF647 but has lower efficiency for some dyes with different emission spectra and is incompatible with Cy3B for dSTORM applications (Olivier et al., 2013).

3.1.5 Sample mounting

The sample mounting steps are detailed and commented below:

1. Two final washes in large volumes of PBS (2 times 50 ml). The coverslip is immersed into a PBS-filled beaker and gently stirred in the solution for

- 1 min. The coverslip edge is blotted on clean absorbent paper and the operation is repeated with the second beaker.
2. Fluorescent beads with a diameter of 0.1 μm emitting at four wavelengths (TetraSpeck Microspheres, Invitrogen) are diluted by addition of 0.6 μl of the bead suspension to a cell culture well containing the coverslip and 1 ml of PBS. Place cells plus beads mixture on an orbital shaker at low rotation speed (~ 100 rpm) for 5 min.
3. The coverslip side that will be facing the microscope objective is washed with milliQ water to remove buffer salts and to clean the surface. The coverslip edge is blotted on clean absorbent paper and the sample is mounted on a microscope slide containing a 100 μl well and filled with the photoswitching buffer. The cell-coated coverslip side should not be allowed to become dry.

For the final step of sample preparation, it is essential to eliminate all remaining non-bound fluorescent probes and other contaminants such as cell debris or particles. Also, fiducial markers are added to the sample in order to correct for lateral stage drift, and in the case of multicolor experiments to serve as an internal control to correct chromatic aberrations (c.f. Section 3.3.1).

The fiducial markers selected here to image nuclear structures in fixed cells are fluorescent beads. They are added to the sample at the latest stages of the preparation in order to adhere to the cell surface. Indeed, the middle cross section of *Drosophila* S2 nuclei is typically found at ~ 3 μm above the coverslip surface. Beads cannot be localized with sufficient precision if not in the focal plane of imaging, which deteriorates the drift and chromatic aberration correction efficiency (Erdélyi et al.). In this context, the capacity of beads to adhere to the cell surface is highly convenient as it ensures the presence of fiducials at different axial positions in every field of view. In many cases though, beads may get partially detached during imaging (*i.e.* do not remain stably bound). These fiducials should not be taken into account for drift or image registration analysis. It is therefore recommended to adjust bead concentrations such that 5–10 beads are found within the field of view of 45 x 45 μm .

In (d)STORM, photoswitching of organic fluorophores is achieved in the presence of a reducing agent and in conditions of depleted oxygen (Dempsey et al., 2011; Heilemann et al., 2008). However, SMLM acquisitions are time consuming and

oxygen and pH level variations may occur during the image acquisition process. This can negatively affect image quality if not controlled. It is a widely spread practice to monitor these photoswitching buffer parameters and to change the buffer solution when judged necessary. Repeatedly measuring pH and oxygen levels during imaging may reveal tedious and impractical. Alternatively, efficient isolation from the ambient oxygen can be achieved by sealing the imaging chamber. In this configuration, the buffer displays constant behavior for at least 3-4 hours. After that period, the sample is unsealed and fresh buffer can be added. For this purpose, flexible sealing is obtained using duplicating silicone (Rotec).

3.1.6 Antibody conjugation with fluorescent dyes

The degree of labeling (DOL) of an antibody, *i.e.* the number of fluorophores covalently attached to it, is a critical parameter both in diffraction-limited and super-resolution techniques. On one hand, for some methods (Confocal, SIM, and STED) a high DOL is preferred as it results in strong signal and resistance to photobleaching. Similarly, the density of detected events in (d)STORM** is higher when high DOL probes are used, since the probability of activating a fluorophore on a given antibody is increased. An excessive number of dye molecules, though, can negatively affect the antibody binding capacity. Typically, for commercially available labeled antibodies the DOL varies between 2 and 8 fluorophores, depending on the antibody, the dye, and the production batch. On the other hand, the resolution of SMLM is limited by the fraction of time the fluorophore spends in the emitting state, called the duty cycle (see Chapter 2, p.57). Consequently, a high DOL would increase the apparent duty cycle of that probe and hence the probability of multiple fluorophore localizations. This is a particularly acute problem when imaging protein clusters containing tens of proteins per diffraction limited spot. DOLs comprised between 1 and 4 are recommended in literature (van de Linde et al., 2011), depending on the dye duty cycle, photoswitching buffer composition and image acquisition parameters.

** The use of brackets in "(d)STORM" indicates that the statement is true both for dSTORM, where a single type of fluorophore is conjugated, and for STORM, which relies on two types of fluorophore per antibody to form the dye activator-reporter pair.

Importantly, the DOL is obtained through spectrofluorometric measurements of the labeled antibody solutions, which only yield mean values. As a result, a solution of labeled probe with DOL of 3 will contain molecules coupled to a variable number of dyes. This heterogeneity at the single-molecule level may affect the output of SMLM experiments by introducing artefactual localization density variations, which are enhanced as the DOL increases. To limit the effect of labeling heterogeneity at the single-molecule level, DOLs of 1-1.5 were chosen in this thesis. The control of the DOL depends on several parameters: the molar ratio between the dyes and the antibodies, the pH of the reaction buffer, temperature and time of the reaction.

Antibodies are commonly conjugated to fluorophores by the formation of a stable amide bond involving the amine groups present in the peptide chain and succinimidyl ester groups coupled to the dye molecules. Amines are reactive in their non-protonated form. Hence, the preferred reaction buffers are with alkaline pH between 8 and 9. On the other hand, for the specific reaction with the amine terminus ($pK_a \sim 9.5$), which additionally will yield low DOLs, the labeling may be performed at neutral pH.

There are two main types of coupling reactions depending on the environment. The most common type of reaction includes antibodies and reactive dyes freely diffusing in solution. This strategy is convenient when large amounts of the antibody are available, since efficient labeling is achieved for high protein concentrations (above 2 mg/ml) in volumes of $\sim 30 \mu\text{l}$. In addition, the pH during the different steps is constant when the reaction takes place at neutral pH, which preserves the antibody from denaturation. Only antigen affinity-purified antibodies must be used in solution-based labeling, as the presence of other proteins would result in loss of specificity during imaging. A thorough purification follows the reaction to eliminate free dyes, classically through gel filtration. Complete removal of free dye frequently needs a final step involving extensive dialysis. The efficiency of unreacted fluorophore removal from the antibody suspension is a major concern, especially for SMLM experiments, and its monitoring is essential. To obtain labeled antibodies with low levels of unreacted fluorophores, solid-phase labeling is the type of dye conjugation reaction of choice (Lundberg et al., 2007). In this method, a matrix of porous resins (*i.e.* beaded agarose) or magnetic beads is functionalized commonly with antibody-binding bacterial protein A or protein G, which are selected according to the

antibody host species. When introduced into the resin bed, the antibody is immobilized to the column by affinity binding. The solid-phase approach combines antibody purification and dye labeling in a single step, which allows the input of antibody solutions that contain stabilizing proteins and chemicals, which are frequently added by manufacturers. Furthermore, this procedure is able to label antibody quantities and volumes as low as 10 μg and 10 μl respectively, which is highly convenient for commercial antibodies. After labeling, antibodies are recovered from the column by low pH (~ 3) elution. This step may affect the specificity and reactivity of some pH-sensitive antibodies. There are higher pH (4-6) elution buffers commercially available, although they may result in a low purification yield. Independently of the labeling strategy, the antibody specificity and the absence of free fluorophore need to be controlled by conventional microscopy prior to super-resolution experiments. When labeling nuclear components, the presence of free dyes for example is readily manifested by an increase of fluorescence in the cytoplasm, whereas antibody denaturation results in a loss of intensity in the nucleus.

The final protocol for antibody labeling is detailed in Section 3.6.2.

3.2 Image acquisition in SMLM

3.2.1 Film length

SMLM achieves sub-diffraction resolution by temporal separation of the fluorescent signal originating from individual probes within image areas the size of a PSF. This requires the recording of image sequences, the length of which depends on the photoswitching kinetics of the emitting molecules and the density of labeling of the target structures in the sample. As a consequence, a high number of fluorophores in the sample commonly results in long acquisition times. The camera frame rate is matched with the blinking dynamics of the sample such that the emission from a blinking event is detected on average during a single or a few frames. The ideal acquisition duration of SMLM experiments, ensuring a

maximal rendering of the labeling density of the sample, lasts until all fluorophores in the field of view are photobleached*.

If fluorescent beads are used as fiducial markers to correct for lateral stage drift, they can substantially lose their intensity or photobleach in long acquisitions (tens of minutes). We have found that in our imaging conditions (see below), 0.1 μm TetraSpeckTM Microspheres are detectable for $\sim 30,000$ frames (per detection channel in 2-color acquisitions) at 50 ms frame rate. To circumvent this limitation, an alternative would be the use of functionalized gold fiducials, as recently described for yeast samples, where streptavidin-bound gold nanorods were imaged at several μm from the coverslip surface (Kaplan and Ewers, 2015).

3.2.2 Excitation/activation scheme

Single-fluorophore detection is central to SMLM experiments, and is dependent on photoswitching kinetics in the sample. These in turn are modulated by the chemistry of the mounting medium, in the case of (d)STORM, the excitation and/or activation laser power for PALM and (d)STORM, and the fluorophore density. On one hand, photoactivatable proteins such as mEos2 may be activated by the excitation laser (561 nm). Thus, for very dense samples the power of the readout laser has to be adjusted to ensure single molecule conditions (as the higher the excitation powers the higher the probability of photoactivation). On the other hand, organic dyes like AF647 and Cy3B, under low oxygen conditions and in the presence of a reducer, typically require an additional activation (405 nm). In this case, increasing the excitation power results in higher emission intensities and accelerates the transition to the dark states. The activation laser mediates the transition from the metastable dark state back to the ground state (S1). Thus, the combination of excitation and activation illumination accelerates the photoswitching dynamics of fluorophores allowing faster acquisition as long as single molecule conditions are respected (one emitter per diffraction-limited area). Both pulse and continuous illumination can be applied to obtain the desired blinking behavior. In our system, the simplicity and high efficiency of continuous excitation and activation was preferred. Frequently used illumination

* In dense pools of molecular targets, such as nuclear proteins, this requirement may not be achieved due to diverse factors including fiducial marker photobleaching, photodamage on the sample, or limited data storage capacity.

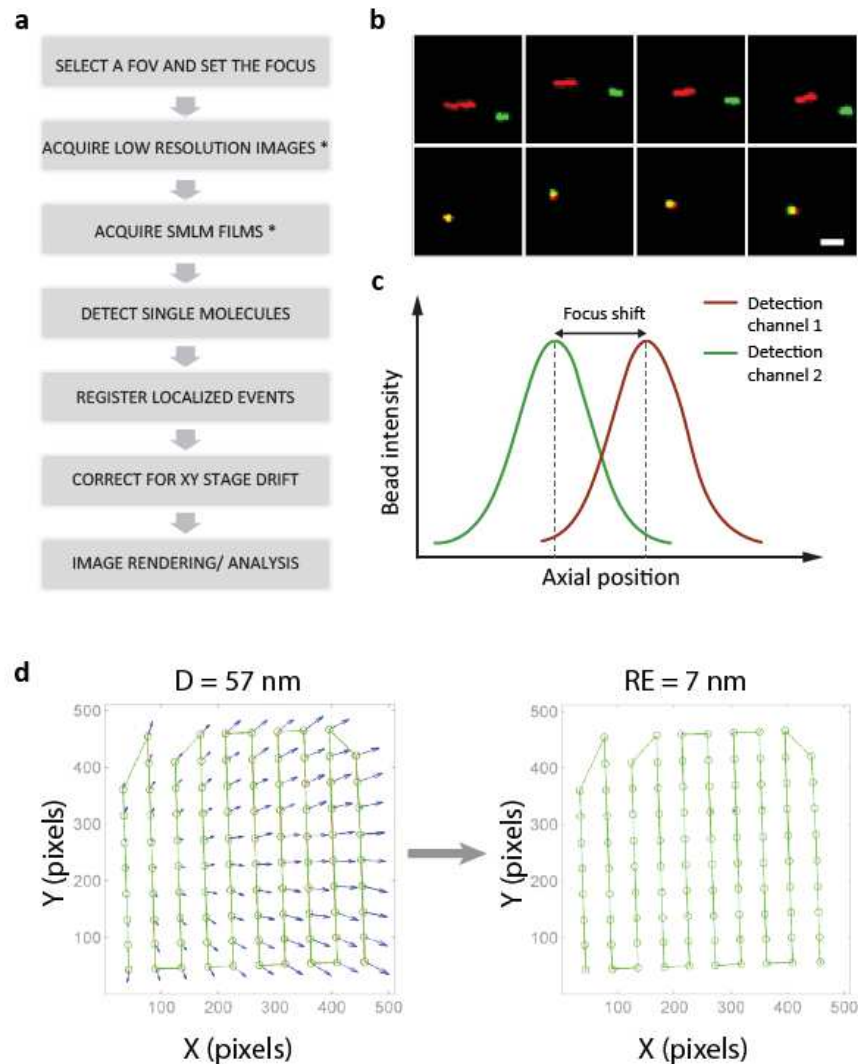
powers in SMLM imaging of *Drosophila* nuclear components are as follows: 1 kW/cm² at 641 nm (for AF647), 0.8-1.2 kW/cm² at 561 nm (for Cy3B and mEos2), and 0-0.1 kW/cm² at 405 nm for activation. The intensity of activation is progressively increased throughout the acquisition to ensure a constant amount of simultaneously emitting fluorophores within the labeled structures.

3.2.3 Sequential acquisition of two-color SMLM images

Multicolor fluorescence imaging of cellular components has the potential to reveal spatial proximity (colocalization) of the labeled species, providing an *in situ* indicator of putative molecular interactions. SMLM techniques allow the precision of the colocalization measurements to be substantially increased, as the resolution is improved ~ 10 -fold compared to diffraction-limited methods. Imaging molecular species in two or more colors, however, is prone to systematic errors related to the optical system (chromatic aberrations) and the spectral properties of the detected fluorophores (crosstalk between the different species)(Scarselli et al., 2012). Different imaging and analysis modalities have been implemented to correct for errors in multicolor experiments (Heilemann et al., 2009; Lampe et al., 2015; Shroff et al., 2007; Testa et al., 2010).

As for conventional microscopy, the signal from the different detection channels may be recorded simultaneously or sequentially. Simultaneous SMLM acquisition may be achieved by simultaneously activating spectrally separated fluorophores, individually detected by splitting the camera chip with a dichroic-based emission splitter (Crossman et al.; Ries et al., 2012b). To correct for chromatic aberrations in this configuration, an image registration step is required. While convenient for some applications, the observation area is reduced at least twice, and in the case of small cells like *Drosophila* cell lines, the experiment throughput is reduced. Alternatively, using activator-reporter dye pairs (STORM), the same reporter dye and detection channel may be used while activating different activator dyes with lasers of different wavelengths (Bates et al., 2007b). No image registration is required here, however, the system suffers from channel crosstalk that needs to be evaluated and removed in a complex post-processing step.

Figure 3.2 - Sequential 2-color SMLM imaging procedure



(a) – Acquisition and post-processing pipeline in two-color SMLM. The asterisk in steps 2 and 3 indicates that the focus must be adjusted before the acquisition in the second channel. **(b)** – *Top*: Reconstructed 2-color SMLM images of four Tetraspeck beads from the same field of view and separated by $>10 \mu\text{m}$ from one another, before processing. Lateral drift over the acquisition of 20,000 frames per channel is reflected by the elongated trace-like images of the spherical beads. Images from the red and the green channel do not overlap due to chromatic aberrations in addition to drift. *Bottom*: The same beads but after drift and chromatic shift correction. Scale bar: 50 nm. **(c)** – Schematic representation of the calculation of focus shift in two-color acquisitions of spectrally separated fluorophores. The normalized bead intensity in each channel can be fitted with a Gaussian function. The peak of the curve indicated the position of the focus plane of the bead. The difference in the intensity maxima is used to adjust the focus before starting the acquisition in channel 2. **(d)** – Bead scan for image registration. *Left*: raw localization plot of the bead at each position on the field of view. Positions are indicated with red (for channel 1) and green (for channel 2) empty circles. Blue vectors indicate the extent and directionality of the local chromatic offset, which is inhomogeneous in the field of view. Before correction, the mean distance between red and green beads is $D=57\text{nm}$. *Right*: After registration using the “local weighted mean” transformation, bead positions are corrected and the mean registration error (RE = 7 nm) indicates a substantial improvement in coincidence of the XY bead coordinates (note that blue arrows are too small to be seen in this image).

In the sequential acquisition mode, spectrally separated dyes are activated and detected at different time points of the acquisition, minimizing channel crosstalk. The whole field of view (FOV) can be used for each of the colors and the optical setup needs no modifications with respect to single color acquisitions. Therefore, sequential imaging was performed in the multicolor experiments described here. The individual acquisition steps are detailed below and schematically summarized in Figure 3.2a.

The use of separate detection channels leads to a chromatic offset in the resulting images on the camera in all three directions. Chromatic aberrations in the lateral direction result in image distortions such that the same object detected in the two channels appears at different positions on the camera as depicted in the upper panels of Figure 3.2b. The lateral displacement of images can be corrected during post-processing in a procedure described in Section 3.3.1.

In the axial direction, a focus shift is observed, and its amplitude increases with the increased difference between the detection wavelengths. Therefore, the focus must be adjusted, prior to the acquisition of the second color. For this purpose, the following steps were implemented:

1. The focus is set in one of the colors over the FOV of interest.
2. The intensity of one or several beads in the field of view at or close to the focus set in the previous step is measured from -1 to $+1$ μm from the focus position of the bead along the Z axis. The same operation is repeated for the second color.
3. A plot of the intensity as a function of the axial position is drawn for each bead in the two colors. A Gaussian fit is applied to each curve and the focus shift is calculated as the difference between the axial positions at the peaks of the curves in each color as shown in Figure 3.2c.

Note that the focus shift is relatively constant between the different FOVs and increases slightly with the depth of the imaging plane. However, the rapidity and simplicity of the focus adjustment procedure allow the focus correction for every SMLM film. In the experiments described here, in which the detection channels are at 700 nm (AF641) and 600 nm (Cy3B or mEos2) and the imaging planes are at ~ 3 μm deep in the sample, the focus shift adopts typically values of 500 ± 70 nm.

In conventional microscopy, the lower wavelength acquisition is performed first, in order to preserve the sample from photobleaching. In dSTORM experiments, no substantial difference was observed when the order of channels was switched. In PALM/dSTORM acquisitions though, when fluorescent proteins are detected in one of the channels (e.g. mEos2 and AF641 as a PALM/dSTORM pair), it is preferable to image first the protein channel as the continuous activation laser (405 nm) powers are lower than for organic dyes. When mEos2 was imaged after AF641, the protein was essentially overactivated and little single-molecule blinking could be observed.

3.3 Data analysis

In this section I briefly describe the two-color SMLM image post-processing steps that I have implemented in a graphical user interface using Matlab (SMLM_2C).

3.3.1 Detection and post-processing of localization data

Following the acquisition of SMLM films in *Drosophila* nuclei, the images are obtained after several steps of processing that are described. The procedure is identical for single and 2-color experiments with the exception that for the latter an additional lateral chromatic error correction is required.

Localization of single-molecule fluorescent events is performed using two localization algorithms: 1-the Localization Microscopy plugin in Micromanager (Edelstein et al., 2014), and 2- Multiple Target Tracing (MTT) (Sergé et al., 2008). The former is very convenient for its speed and good performance and was mainly used during acquisition to check the quality of the samples and films. The latter method is slow, however it yields superior detection efficiency and accuracy.

Chromatic aberrations correction in 2-color experiments is applied as previously described in (Churchman and Spudich, 2012) (see Section 3.6.3). As shown in Figure 3.2b, distortions of the image are observed between the different colors. This error in the positioning of the same object can be corrected by an operation termed image registration, which is the process of aligning images of the same source. One of the images is selected as reference and the

second image is geometrically transformed (for example by translation, scaling, and rotation) to match with that reference. For superresolution images, a local nonlinear (local weighted mean) transformation yielding nanometer registration precision is applied. To perform image registration an additional acquisition is required, in which a bead is imaged in the two colors at different positions of the field of view. The following steps are performed in our two-color SMLM experiments:

1. A fluorescent bead in the imaged sample is automatically scanned across the FOV using custom acquisition software. Ideally, the bead should have the same axial position as the structures or markers of interest.
2. For each position of the scan, a short film (20–30 frames) is acquired in each of the detection channels (Figure 3.2d)
3. The higher the number of positions recorded, the better the precision of registration. For a $45 \times 45 \mu\text{m}$ FOV a scan of 12×12 bead positions yields satisfactory results.
4. The beads positions are detected using MTT and the spatial transformation required to align images is calculated. The mean error of registration (see Section 3.6.3) is calculated, which typically ranges between 5 and 10 nm (Figure 3.2b, lower panels), as reported to be the maximum precision of this method (Churchman and Spudich, 2012; Malkusch et al., 2012). Bead scans with TRE > 10 nm are typically discarded.
5. The transformation is applied to the localizations detected on the sample in one of the channels. The reference channel in the beads image and the sample must be at the same wavelength.

Drift correction is applied using a custom algorithm (Fiche et al., 2013a) (see Section 3.6.4), which I adapted for 2-color acquisitions. A short part of the film is automatically loaded by the analysis program, and after processing beads are identified by means of an automatic (or user-defined) intensity-based threshold, as beads intensities may vary between experiments. The trajectories of beads are calculated and a reference trajectory is derived to correct the positions of the single-molecule events detected during the time of the acquisition. Importantly,

in two-color experiments, the co-ordinates of localizations in the two channels are concatenated for the drift correction, since the acquisitions have occurred sequentially. After the drift correction is applied, the localizations are re-attributed to their respective channels for further processing.

At this stage of the analysis, it is imperative to monitor the performance of both the image registration and drift correction. For this purpose, the super-resolved images of the entire field of view are reconstructed and the following controls are performed:

1. Visual inspection: the spherical shape of the fiducial marker localization distributions illustrates the good performance of the drift correction.
2. To evaluate the alignment of images in the two colors on drift-corrected localizations, the registration error (RE) is calculated on the beads used for drift-correction. If $RE > 10$ nm the images are discarded from 2-color analyses. Note that when the drift correction is satisfactory (even if the chromatic aberration correction is not) single color analyses can still be performed on these datasets.

Segmentation is a convenient post-processing step in which the FOV is split in regions of interest (ROIs). Each ROI contains a single cell, thus localizations from different cells on the same image can be classified and analyzed separately. In the case of SMLM, a 45×45 μm FOV contains thousands of localizations in each color (typically $\sim 10^5$), which may be challenging due to computer power limitations. Two types of filters have been implemented in the 2-color analysis program. These filters are applied to filter out false positive localizations, such as events detected from beads (high density of detections) or non-specific events (low percentage of the total detected events). Briefly, the following operations can be performed after drift and chromatic aberration corrections using the SMLM_2C program:

1. In the Manual mode, rectangular ROIs are defined through interactive selection.
2. The Automatic segmentation mode uses low resolution images (epifluorescence image acquired before the SMLM film) to detect the regions containing specific fluorescent labeling. Background is subtracted, a Sobel filter is applied for edge detection of the specific signal (a function readily

available in the Matlab “Image processing toolbox”), and a series of morphological operations (dilation, erosion) are performed to detect the ROIs. When proteins or complexes with homogeneous distributions within the nuclear compartment are imaged, such as the RNA polymerase II (Pol2) or Insulator Binding Proteins (IBPs), the fluorescence signal is sufficient to segment the nuclear regions^{*}. The resulting ROIs are sorted according to their size and shape using predefined criteria. For instance, IBP-stained nuclei with elongated shapes (length ratio between major and minor axis $> \sim 1.5$) are discarded as *Drosophila* S2 nuclei are essentially spherical. Similarly, ROIs with diameter outside of the 4-6 μm range are discarded. Regions smaller than 4 μm would belong to cells that are either in a critical physiological state, to out of focus cells, or to cell debris, while larger nuclei may correspond to cell aggregates or mitotic cells.

Image reconstruction is a post-processing step required to retrieve the localization information from SRM experiments into pixel-based images. The SMLM methods yield a list of discrete spatial coordinates that are pixelated (*i.e.* grouped together) to form an image. Image reconstruction can be performed in several ways. One method is the representation of localization coordinates as a 2D histogram in which the intensity is proportional to the number of localizations in a given pixel with a user-defined size. Another method is a widely applied rendering approach, in which the intensity associated with each localization event is spread on the surrounding pixels with a Gaussian distribution of standard deviation equal to the experimental localization precision. The pixel size is defined by the user and is typically ~ 2.5 fold smaller than the standard deviation of the Gaussian function.

3.3.2 Quantitative analysis of colocalization

Methods to measure the association of two cellular components

Multicolor fluorescence microscopy is frequently applied to evaluate the relative spatial distributions of cellular structures and components and provide a

^{*} If localized signal is imaged such as in FISH, DAPI staining of DNA is used to segment nuclear regions in cells.

spatiotemporal framework for biological phenomena. To study molecular interactions on the <10 nm lengthscale Förster Resonance Energy Transfer (FRET) techniques are most commonly applied. For longer than 10 nm separation between the molecular species of interest, the colocalization or the degree of spatial coincidence is estimated in a qualitative or quantitative manner using diffraction-limited microscopies. In spite of being widely used as an indicator of potential structural and functional association between factors, colocalization in confocal microscopy has a precision limited by the diffraction of light. This is due to the fact that structural details beyond the limit of diffraction cannot be resolved by confocal microscopes. In other words, when two species are considered colocalized, their true distance may be $>\sim 250$ nm. This limitation becomes then critical given that proteins have a typical size of a few nanometers (~ 5 nm for a 50 kDa globular protein). Classically, to estimate the degree of colocalization from fluorescence images one can analyze the intensity information of the pixels. Alternatively, in object-based methods, the structural features of the detected signal are extracted through the process of segmentation, and the distances or overlap between the identified “objects” are measured (Bolte and Cordelières, 2006; Cordelières and Bolte, 2014).

Intensity-based approaches evaluate the extent of correlation between the pixel values in the first detection channel and the pixel values in the second channel. This type of colocalization analysis is not suited for SMLM. The reason lies in the nature of the SMLM image, which is reconstructed from lists of position coordinates. The intensity in reconstructed SMLM images typically integrates the number of detections in a given pixel, and the PSF intensity of single molecule emission events. The density of localizations depends on the density distribution of target molecules, but also on the efficiency of labeling, and importantly, on the blinking dynamics of the dye. The photoswitching properties are specific to each fluorophore. Hence, two SMLM images of the same structure labeled with the same labeling efficiency but with two different fluorescent dyes would result in different intensity distributions.

Object-based colocalization analysis is applicable on SMLM data as it relies only on the structural properties of the signal. In conventional fluorescence images, segmentation is performed by applying an intensity threshold on the image. Segmentation of single-molecule localizations into objects is performed by grouping the individual events that are found closer than a given distance in a

method termed clustering (see Clusterization in PALM/STORM in Section 4.6 for the principle and application of clustering analysis). The size, position and shape of the identified “clusters” can be measured. Structures with centers found at a distance smaller than the size of the objects (because of overlap) or smaller than the resolution of the technique (10-20 nm in SMLM) can be thus considered colocalized.

Coordinate-based colocalization analysis (CBC)

A novel approach for single-molecule colocalization quantification has been recently introduced by Malkusch et al. (Malkusch et al., 2012) with the name of Coordinate-Based Colocalization analysis (CBC). The procedure is analogous to the Pearson correlation coefficient calculation for conventional microscopy (Manders et al., 1992). The Pearson correlation is an intensity-based approach that calculates the correlation between the pixels’ intensities in the two channels, or the extent to which the pixel values tend to change together. For each 2-color image, the Pearson correlation yields a single coefficient with values comprised between -1 for negative correlation (interpreted as exclusion between the two signals) and 1 for complete positive correlation (colocalization), with 0 when no correlation is found.

In CBC, a colocalization coefficient is attributed to each single-molecule localization, from each detection channel, by calculating the Spearman rank-order correlation. If A are all events detected in the first channel and B are all events detected in the second channel, then the CBC coefficient of the localization A_i is determined as follows (Malkusch et al., 2012):

1. Distribution of localizations of species A around A_i

$$D_{A_i,A}(r) = \frac{N_{A_i,A}(r)}{\pi r^2} \cdot \frac{\pi R_{max}^2}{N_{A_i,A}(R_{max})} = \frac{N_{A_i,A}(r)}{N_{A_i,A}(R_{max})} \cdot \frac{R_{max}^2}{r^2}$$

2. Distribution of localizations of species B around A_i

$$D_{A_i,B}(r) = \frac{N_{A_i,B}(r)}{N_{A_i,B}(R_{max})} \cdot \frac{R_{max}^2}{r^2}$$

where $N_{A_i,A}(r)$ is the number of localizations of species A within the distance r around A_i , and $N_{A_i,B}(r)$ is the number of localizations of species B within the

distance r around A_i . The distributions are corrected for the area (πr^2), normalized by the number of localizations within the largest observed distance R_{max} (see below) and divided by the largest observed area for species A ($N_{A_i,A}(R_{max})/\pi R_{max}^2$) and B ($N_{A_i,B}(R_{max})/\pi R_{max}^2$). A uniform distribution would give an expected value of $D(r) = 1$ for all r .

3. Attribution of ranks to each distribution for each r
4. Calculation of the Spearman rank correlation

$$S_{A_i} = \frac{\sum_{r_j=0}^{R_{max}} (O_{D_{A_i,A}}(r_j) - \overline{O_{D_{A_i,A}}})(O_{D_{A_i,B}}(r_j) - \overline{O_{D_{A_i,B}}})}{\sqrt{\sum_{r_j=0}^{R_{max}} (O_{D_{A_i,A}}(r_j) - \overline{O_{D_{A_i,A}}})^2} \sqrt{\sum_{r_j=0}^{R_{max}} (O_{D_{A_i,B}}(r_j) - \overline{O_{D_{A_i,B}}})^2}}$$

where $O_{D_{A_i,A}}(r)$ is the rank of $D_{A_i,A}(r)$ calculated after Spearman, and $\overline{O_{D_{A_i,A}}}$ is the arithmetic average of $O_{D_{A_i,A}}(r)$.

5. The colocalization value C_{A_i} , is calculated as :

$$C_{A_i} = S_{A_i} \cdot e^{\left(-\frac{E_{A_i,B}}{R_{max}}\right)}$$

where $E_{A_i,B}$ is the distance from A_i to the nearest neighbor from species B . C_{A_i} is calculated for every single-molecule localization and can adapt values from -1 to 1 , similarly to the Pearson coefficient.

Implementation of CBC for automated whole-cell analysis (aCBC)

The calculation of the CBC coefficient requires three types of input: the localization coordinates from the two detection channels, the distance interval r , within which the number of neighbors will be counted, and the position and size of the region to analyze. In the original work (Malkusch et al., 2012), the analyzed area (ROI) is user-defined, similarly to the manual segmentation procedure described in Section 3.3.1, and is chosen to select only a small subset of the localizations in the image. In addition, all the events within the ROI are

considered correlated. In this context, R_{max} reflects the total area occupied by the localizations in the ROI.

To avoid manual selection of ROIs for the CBC analysis of nuclear protein distributions, I implemented an automated variant of CBC (aCBC).

Two user-defined parameters are employed:

1. R_{max} is the value corresponding to the radius of the region, in which the distance distributions will be calculated for each localization. For each detection event, all the localizations found outside the area defined by R_{max} are considered uncorrelated. To determine the value of this parameter for a given dataset, one should consider the size of the structures from each channel, and the distances between the structures in the 2-color image.
2. The distance interval r corresponds to the bin size of the distance distribution histograms ($D_{A_i,A}$ and $D_{A_i,B}$) that are calculated in the first step of the CBC analysis. Each histogram contains R_{max}/r number of bins. Therefore, r defines the resolution of the aCBC analysis.

Determination of aCBC parameters

To evaluate the input parameters value impact on the output of the aCBC analysis, a simple case was considered (Figure 3.3). A synthetic 2-color reconstructed image was generated (Figure 3.3a), in which the first channel (red) represents two Gaussian clusters of single-molecule localizations (as obtained in SMLM experiments), found at a distance of 200 nm from one another. In the second channel (green), a single Gaussian cluster is partially co-localizing with one of the red clusters, with a peak to peak distance of 30 nm. The peak to peak distance between the green cluster and the second red cluster is 170 nm. All the clusters contain 500 localizations and have the same size ($\sigma=30$ nm). The values for r and R_{max} (R for simplicity) are in nm.

The cumulative histograms of aCBC values (Figure 3.3b,c) and the respective aCBC maps (Figure 3.3d,e) of the clusters from the red channel illustrate the differences in output that can be obtained for the same situation by varying either r or R_{max} (R for simplicity). The aCBC analysis was performed by testing 3 values for r at constant R (Figure 3.3b,d), and 3 values for R at constant r

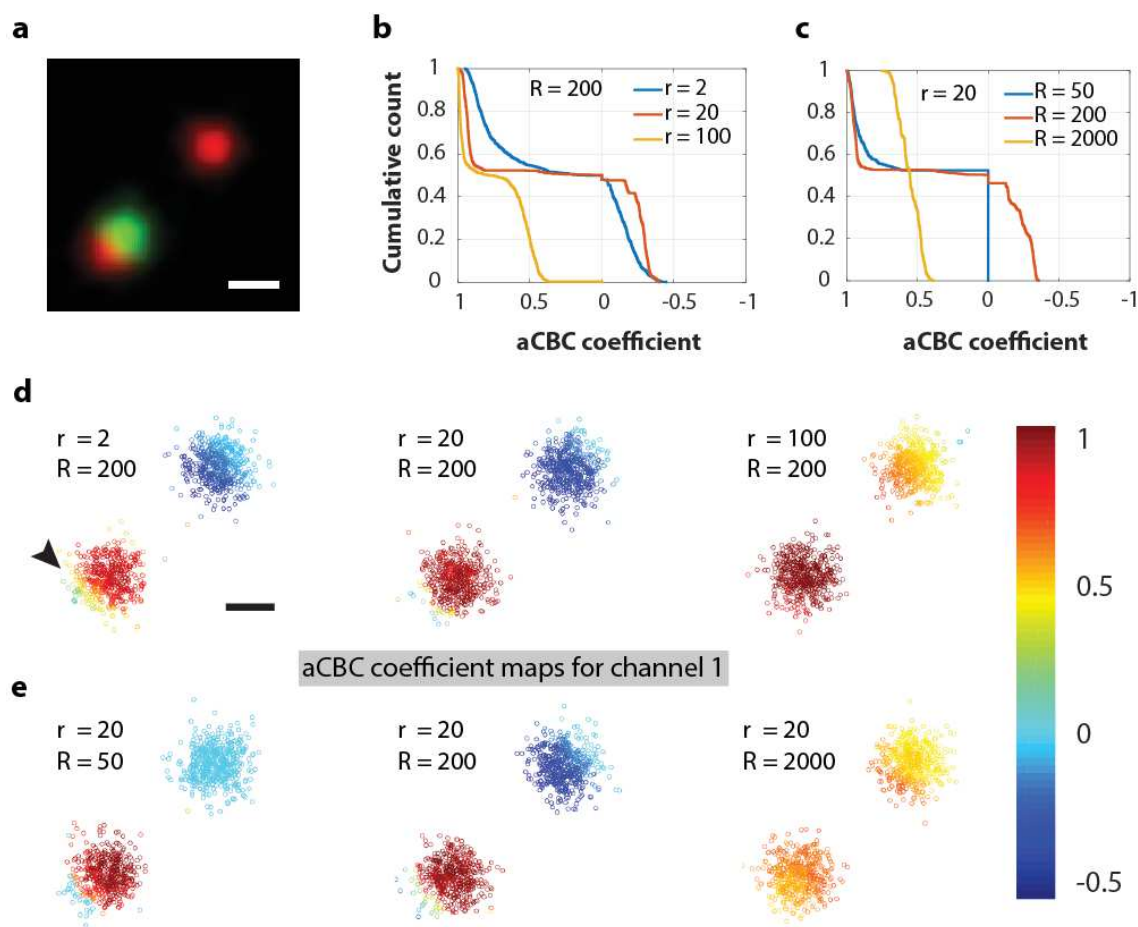
(Figure 3.3c,e).[†] When r is small (2 nm), the analysis finely probes the distances between localizations and results in smoothly distributed positive correlation values for the lower cluster, and negative correlation values for the upper cluster (Figure 3.3b, blue curve). In the colocalizing cluster (Figure 3.3d left panel), the events that strongly overlap with events from the green channel can be differentiated from the events that are in close proximity but overlap with only a small number of events from the green channel (arrowhead). Similarly, in the non-colocalizing cluster, the events that are close but do not overlap with the green cluster display a stronger anti-correlation (dark blue dots) compared to the events that are further away from the green cluster (light blue dots). When r is increased to 20 nm (Figure 3.3d, middle panel), the events from a given cluster show a higher homogeneity and the contrast between the aCBC values in the colocalizing (dark red dots) versus the non-colocalizing (dark blue dots) cluster are enhanced. Thus, approximately the same coefficient is attributed to the events belonging to the same structure (cluster), which may be convenient for analysis of more complex samples. When $r=100$ nm (Figure 3.3d, right panel), a single bin of the distance histograms comprises the large majority of the events from each cluster. The events from the colocalizing structure display similar values to the previous condition. However, the events from the non-colocalizing cluster are considered as positively correlated, and a wrong conclusion of colocalization may be drawn.

As stated above, the parameter R determines the distance, up to which the correlation (positive or negative) is probed (Figure 3.3c, e). For $R=50$ nm (Figure 3.3e, left panel), that is, smaller than the size of the clusters, the colocalizing cluster displays high aCBC values similar to the previous conditions, whereas all the events from the non-colocalizing cluster are excluded from the analysis and considered uncorrelated (straight line at aCBC=0 in Figure 3.3c). At $R=200$ nm (Figure 3.3d and Figure 3.3e, middle panels), which corresponds to the distance between the two red clusters, the area where correlation is probed is large enough to take into account both red clusters and correlate them with the green cluster. As a result, two populations of positive and negative aCBC coefficients can be distinguished (Figure 3.3c, red curve), corresponding respectively to the events from the colocalizing and non-colocalizing cluster. Last, for $R=2000$ nm

[†] For simplicity, only the colocalization coefficients of the red channel are displayed, since the effects commented below are equivalent for the cluster in the green channel.

(Figure 3.3e, right panel), the area by which the distance distributions are normalized is such, that the population information is lost (Figure 3.3c, yellow curve). The colocalization for the lower red cluster is underestimated (lower aCBC coefficients compared to the previous conditions). Inversely, the non-colocalizing cluster is attributed positive aCBC coefficients, and thus appears colocalized with the green cluster.

Figure 3.3 - Determination of aCBC parameters



(a) – Composite reconstructed image of 3 clusters of SMLM localizations with Gaussian distribution, 2 clusters in channel 1 (red) and 1 cluster in channel 2 (green). The clusters contain 500 localizations each, and have the same size ($\sigma=30$ nm). The values for r and R_{\max} (R for simplicity) are in nm. **(b)** – Cumulative histograms of aCBC values in the red channel for R constant. **(c)** – Cumulative histograms of aCBC values in the red channel for r constant. **(d)** – aCBC coefficient maps for channel 1 (R constant). **(e)** – aCBC coefficient maps for channel 1 (r constant). Scale bars: 100 nm.

These observations indicate that the definition of R and r is critical for the accuracy of the method. Depending on the experiment and the sample, one may wish to probe very locally for colocalization and exclude from analysis structures that are considered out of range for a given cellular component. The size, shape and distribution of the studied markers, as well as the spatial resolution of the image are to be considered for the determination of aCBC parameter values. Therefore, knowledge on the structure of interest, prior to the aCBC analysis may be helpful to determine the input parameters. For small abundant globular distributions, as frequently displayed by nuclear factors, a clustering analysis step (see Clusterization in PALM/STORM, Chapter 4) provides such information.

For indication, in this thesis, r is attributed the value of the imaging resolution, taking into account the localization precision of the detected events, as well as the precision of the chromatic aberration and drift corrections. For structures presenting Gaussian distributions of the detected clusters, R is $\sim 10 \cdot \sigma$ of the cluster, such that all the events of the cluster are considered for correlation analysis but the other clusters are discarded from the local calculation of aCBC.

Evaluation of aCBC performance

The aCBC analysis provides a method to determine the extent of colocalization with a detail potentially down to the single-molecule resolution. To test the performance of aCBC in complex samples and establish a robust colocalization quantification procedure, SMLM-like datasets with known colocalization levels were generated and analyzed. The approach and parameters of the SMLM cluster simulation are detailed in Section 3.6.5.

First, a complete colocalization situation was simulated and the resulting 2-color reconstructed image is shown (Figure 3.4a). The dataset consists of a random distribution of Gaussian SMLM clusters within a circle with radius equal to $3 \mu\text{m}$ (the size of clusters is $\sigma = 20 \pm 5 \text{ nm}$, and mean number of events per cluster = 50). In the first channel (red), the centers of 100 clusters completely overlap with the centers of 100 clusters in the second channel (green), which contains a total of 200 clusters.[‡]

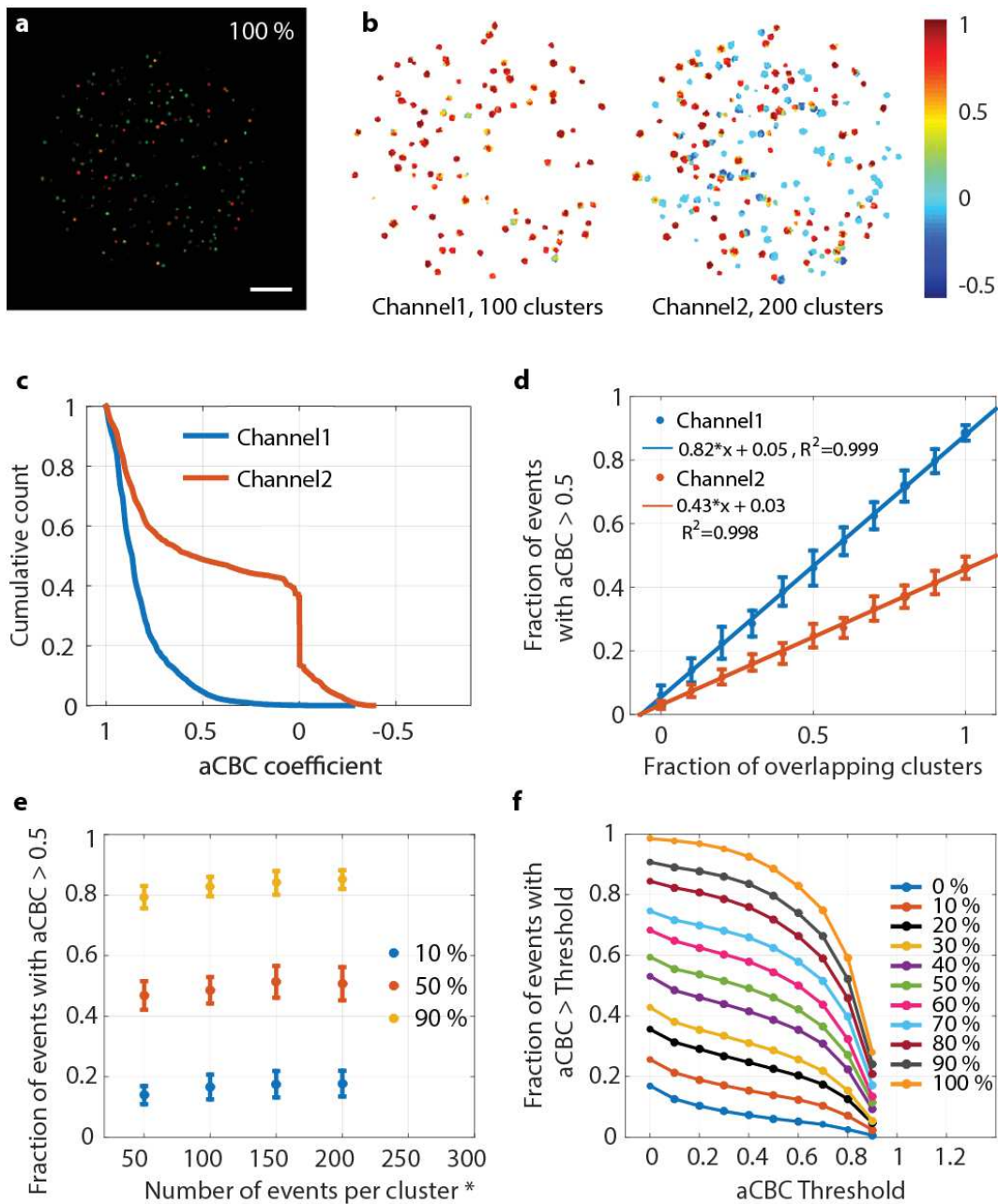
[‡] With the overlay representation of the 2-color image it is difficult to appreciate the degree of colocalization, as it is frequently the case with experimentally obtained images. The intensities

The same dataset was analyzed with aCBC and the colocalization coefficient maps of the individual localizations are shown in Figure 3.4b. As expected, the vast majority of clusters from channel 1 display high correlation coefficients, and from the cumulative histogram (Figure 3.4c) it appears that 93 % of the events in channel 1 have a correlation coefficient >0.5 . In contrast, in channel 2, where only half of the clusters colocalize, three populations of events can be distinguished (Figure 3.4). The largest population is composed of positively correlated clusters ($\sim 60\%$). A second population is defined by completely uncorrelated clusters with $\text{aCBC}=0$ ($\sim 30\%$ of events). The third population contains negatively correlated events ($\sim 10\%$), which correspond to clusters that are positioned in proximity but do not overlap with clusters from channel 1 (Figure 3-4b, right image).

Next, the correlation of the aCBC analysis output and the true colocalization was evaluated. Clusters in 2-colors were generated as above, and the percentage of overlapping cluster centers from channel 1 was varied between 0% and 100%. The aCBC coefficients were calculated, and to compare the different colocalization situations the fraction of localizations with a high colocalization coefficient was extracted from the aCBC coefficient histograms. The results are summarized in Figure 3.4d, where each data point is the mean percentage of events with $\text{aCBC}>0.5$ from 30 simulations at each level of colocalization. The error bars indicate the standard deviation of the mean values obtained from these datasets. A strong linear dependence is observed between the true colocalization (X axis) and the fraction of events with strong positive correlation (Y axis), for both channel 1 and channel 2. This observation indicates that the true colocalization percentage can be inferred by the aCBC analysis in a straightforward manner. Furthermore, the method demonstrates a high level of reproducibility, with average standard deviation of the measurements of 0.04 ± 0.01 for channel 1, and 0.03 ± 0.008 for channel 2.

(density of events) of the different clusters vary independently between the channels even in the case of colocalization, and this difference is the origin of the visual underestimation of structural overlap in the image superimposition method.

Figure 3.4 - Evaluation of aCBC performance



(a) – Composite reconstructed image of a simulated 2-color SMLM dataset or randomly distributed clusters of detections. All the centers of the red channel coincide with centers of the green channel (100% colocalization). Scale bar: 1 μm . **(b)** – aCBC coefficient maps of localizations in the red channel (left) and the green channel (right). **(c)** – Cumulative aCBC histogram of events in the image in a. **(d)** – Correlation between true colocalization and aCBC output. **(e)** – Effect of the mean number of events per cluster on aCBC values for 3 levels of colocalization (10%, 50% and 90%). **(f)** – Effect of the threshold on the resolution of the aCBC method.

To test the robustness of the method with respect to the density of detected events in the individual clusters, four different types of cluster localizations were generated and analyzed with aCBC for three different levels of colocalization (Figure 3.4e). Each data type was characterized by a different mean number of events per cluster ranging from 50 to 200 events.[§] The effect of the density of localizations per cluster on the output of the aCBC analysis was tested for different degrees of colocalization at 10, 50 and 90 percent of overlapping clusters. As shown in Figure 3.4e (results for channel 1), the mean fraction of events with $aCBC > 0.5$ increases only slightly with the number of events per cluster for all the cases of cluster overlap. These results have a significant implication in the colocalization analysis of SMLM experiments. In particular, two SMLM acquisitions of the same markers may yield a variable number of localizations between different acquisitions. The robustness of the aCBC method allows the combination of datasets, which differ in the density of events per cluster, without affecting the results of the colocalization analysis.

The comparison between the different conditions in Figure 3.4d,e was performed by applying a threshold on the aCBC values, and the fraction of events with aCBC coefficient above the threshold were successfully used as a quantifier of colocalization. To explore the effect of the threshold on the aCBC resolution, the dataset from Figure 3.4d was analyzed with a series of thresholds ranging from 0 to 0.9. The mean fraction of events from channel 1 that have an aCBC coefficient greater than a given threshold were plotted as a function of the threshold value (Figure 3.4f). As expected, the increase of the threshold value leads to a decrease in the fraction of events with aCBC coefficients above the threshold. The evolution of these values is monotonous and symmetrical for the different percentages of cluster overlap up to a threshold value of 0.6. For thresholds above 0.6 the data points start to converge, thus decreasing the capacity to discriminate between the different colocalization conditions. The impact of the threshold value is the slightest in the range 0.2-0.6 with very similar resolution, indicated by the distance between points along the Y axis for a given threshold value. Therefore, it can be concluded that the analysis with an aCBC threshold of

[§] These values are the mean of an exponential probability distribution for the number of events per cluster for each simulated cell (c.f. Section 3.6.5).

0.5, which indicates high level of spatial correlation, can efficiently discriminate between different colocalization conditions.

Taken together, these results demonstrate that the aCBC implementation for single-molecule colocalization analysis is a robust and simple to interpret method that can be applied on complex datasets such as the clustered localizations distribution of nuclear factors imaged in 2-color SMLM. The performance of the analysis is tightly dependent on the imaging resolution, which in turn is affected by the sample preparation conditions, as well as by the image acquisition and post-processing. It is then crucial to validate the good quality of these experimental steps, prior to performing analyses to reach biological-significant conclusions.

3.4 Quality control of SMLM images

Nuclear proteins are frequently diffuse and are dynamically localized within the nucleoplasm. When observed with diffraction-limited fluorescence microscopy, these molecules display a homogeneous distribution throughout the nuclear compartment and may be transiently enriched at sites of intensive activity. However, the spatio-temporal resolution of these methods is insufficient to infer patterns of distribution which reflect their biological function.

Recently, several studies have investigated the distribution of chromatin-associated proteins by using super-resolution microscopy, and were commented in Chapter 2. Briefly, the RNAP2 (Cisse et al., 2013) and histone proteins distributions (Izeddin et al., 2014; Ricci et al., 2015) were revealed with high levels of detail, and unknown features of chromatin architecture and transcription initiation were uncovered through quantitative analysis of sub-diffraction resolution images. Nevertheless, the validation of novel structural characteristics in an objective and reproducible manner is a complex task.

In the present section a simple procedure for the quality control of SMLM images is introduced. Through the example of the *Drosophila* architectural protein Beaf-32, displaying a homogeneous nuclear distribution in conventional microscopy, a workflow for the assessment of the labeling efficiency and specificity is proposed

The different strategies for fluorescent labeling of cellular components, namely affinity tags and fusion proteins have their specific advantages and drawbacks, as discussed in Chapter 2. The main concern in immunofluorescence staining is the specificity of the probe, while the transfection of a fluorescent protein construct may lead to aggregation or mistargeting due to overexpression or misfolding, respectively. The specificity of immunostaining may be controlled as discussed above in the sample preparation section (Figure 3.1). The fusion protein expression can be evaluated through Western blot experiments by assessing the amount of total protein in transfected cells relative to untransfected samples, and by controlling the protein molecular weight to discard truncation of the protein sequence. Classically, several promoters with different strengths are tested as well as several transfection conditions. For SMLM imaging, these validation steps are essential, however they may reveal insufficient.

The increased resolution of SMLM methods introduces additional experimental factors, which must be tightly controlled in order to obtain images with optimal quality and biologically relevant results. A critical parameter in the context of fluorescent labeling for super-resolution microscopy is the fluorescent tag size, especially in the case of immunostaining. A classical configuration of affinity labeling of biological samples is the use of a primary antibody targeting the structure of interest, and a secondary antibody bearing the fluorophore molecule. Although it is widely accepted that the tag size in SMLM imaging influences the experimental spatial resolution, secondary antibody labeling protocols are still prevailing.

Here, an experimental procedure is described that allows fluorescent labeling performance to be evaluated in a single step for both transfection and immunofluorescence. It demonstrates the detrimental effect of high molecular weight affinity probes through quantitative colocalization analysis of a doubly labeled protein (Beaf-32) with uncharacterized nuclear distribution.

3.4.1 Dual color protein staining as an image validation strategy

A simple method to evaluate labeling specificity would be to use two different fluorescent tags labeling simultaneously the same factor in a 2-color experiment. In Figure 3.5a, the *Drosophila* insulator-binding protein Beaf-32 is immunostained with either a primary + secondary antibodies protocol (left) or

with a primary antibody alone that is coupled to a fluorophore (right). In both configurations AF647 was used. The same cells were transiently transfected with a Beaf-32-mEos2 fusion and the samples were imaged in 2-color PALM/dSTORM. The low resolution images (epifluorescence) of both the transfection and the immunofluorescence (IF) experiments demonstrate that the Beaf-32 signal is specifically localized within the nucleus and the fluorescence is homogeneously distributed. Some local protein enrichments can be observed in the Beaf-32-mEos2 images. The correspondence between the signal distributions of the IF and transfection experiments is an indicator of efficient labeling and is a useful preliminary control. At this stage, the secondary and the primary antibody immunostaining approaches yield similar results.

3.4.2 Differences between secondary and primary antibody staining

The differences in performance of the two IF approaches can be first illustrated with the comparison of the intensity ratios between the specific (nucleus) versus the nonspecific signal (cytoplasm and nucleus). The table in Figure 3.5b recapitulates these measurements for the AF647 channel images of Figure 3.5a. One can notice the similar intensity ratios between the signal from non-specific binding and autofluorescence (cytoplasm) and the background (outside of cells). These indicate the high level of specificity of both labeling strategies. In contrast, the specific versus nonspecific intensity ratio (nucleus versus cytoplasm) is higher when a secondary antibody is used. The difference originates in the possibility for several secondary antibody molecules to bind on the constant fragment of the primary antibody (Fc, indicated in Figure 3.5c). A signal enhancement is thus obtained as the local concentration of fluorophores is increased. This property of the secondary antibody staining and its higher convenience (lower cost, ease of use), makes the method preferable for conventional and for 3D-SIM microscopies.

However, the use of secondary antibodies increases the effective size of the probe and therefore the distance between the fluorophore and the target molecule. The typical dimensions of an immunoglobulin of class G (IgG) are indicated in Figure 3.5c. The structure and the size values are from the Protein Data Bank (PDB), structure reference 1IGT. In the conditions of neutral pH

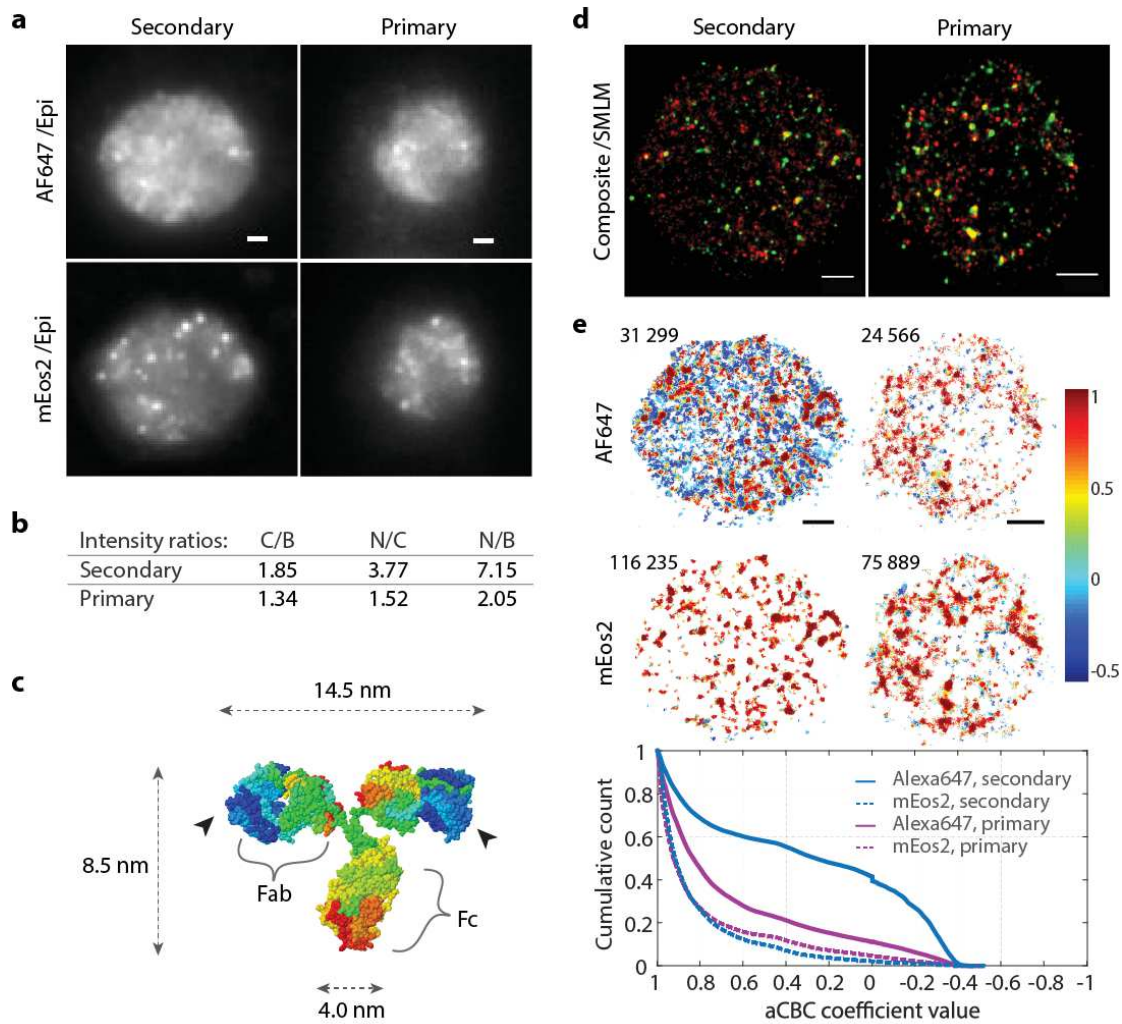
antibody labeling, such as in the protocol discussed above (Section 3.1.6), the fluorescent molecules are conjugated at the amino-termini of the polypeptide chain (dark blue atoms). These lie in the antigen binding domains of the IgG molecule (pointed by black arrowheads). Therefore a fluorescent dye coupled to a primary antibody is found at 0-15 nm from its target, which falls within the localization precision of SMLM instruments. The addition of a secondary antibody increases that distance up to two fold. Although frequently discussed, this aspect of sample preparation for (d)STORM imaging, to my knowledge, has not been investigated experimentally.

3.4.3 Validation of labeling efficiency using quantitative colocalization analysis

Beaf-32-bound antibodies coupled with AF647 molecules should be found in tight spatial proximity to mEos2. Therefore, a strong spatial correlation is expected between the two markers. A visual inspection of the overlaid SMLM images (Figure 3.5d) reveals similar patterns of localizations between the secondary and primary antibody conditions. However, as discussed in Section 3.4.2, in superimposed images the colocalization is underestimated due to differences in intensities between the two channels. The characteristic yellow color indicating colocalization is found mainly in high intensity pixels.

To better appreciate the colocalization levels, a quantitative analysis was performed using aCBC (Figure 3.5e). Remarkably, in the secondary antibody condition, a large population of AF647 events (solid blue line on the aCBC plot) is attributed weak correlation coefficients (positive and negative) and 42% had $aCBC > 0.5$. It is far below the 88% expected for a full colocalization, estimated by the simulations performed in the previous section. Note that the number of localizations in the AF647 channel is lower than in the mEos2 channel. Interestingly, the events from the mEos2 channel (dashed blue line on the aCBC plot) correlate strongly with AF647 events (92% with $aCBC > 0.5$).

Figure 3.5 - Quality control of SMLM images using 2-color labeling and colocalization analysis



(a) – Conventional fluorescence images of *Drosophila* S2 cell transfected with Beaf-32-mEos2 and immunostained with either a secondary (left) or a primary antibody (right) protocol. **(b)** – Signal-to-noise ratio measurements of the images in **a**. C: cytoplasm, B: background (out of the cell), N: nucleus. Cellular and nuclear contours were determined from the brightfield images of the cells (not shown). The mean intensity of each compartment (C, B and N) is calculated and the ratios of intensities are shown in the table. **(c)** – Structure and dimensions of a mammalian immunoglobulin (IgG) from the PDB (1IGT) represented with a “rainbow” color code ranging from dark blue for amino-termini to red for carboxy-termini. *Fab*: fragment antigen binding; *Fc*: constant fragment. **(d)** – Composite reconstructed SMLM images of the cells in **a**. **(e)** – *Top*: aCBC coefficient maps of localizations in the AF647 channel for cells labeled with the secondary antibody protocol (left), and the primary antibody (right). The numbers indicated correspond to the number of detections in each map obtained in 20,000 frames. *Middle*: aCBC coefficient maps of localizations in the mEos2 channel. *Bottom*: Cumulative histogram of aCBC coefficients. Scale bars: 1 μ m.

These results indicate that the Beaf-32-mEos2 protein is efficiently bound by the antibody. Therefore, the low level of AF647 colocalization may be due to a deficiency in the labeled protein expression and/or the IF. For instance, the absence of the fluorescent protein from all the sites occupied by its endogenous equivalent could be caused by mistargeting of the fusion. If such is the case a new genetic construct should be used. Alternatively, the uncorrelated AF647 signal could come from either nonspecific antibody binding, or be caused by an increased distance between the AF647 and mEos2 molecules. The aCBC analysis of the primary antibody staining experiment (Figure 3.5e, right images and magenta lines on the aCBC plot) demonstrates a high level of correlation between mEos2 (86% with aCBC>0.5) and AF647 (77% with aCBC>0.5) events. Hence, it can be concluded that the low colocalization of AF647 events in secondary antibody staining is mainly a consequence of the increased distance between the fluorophore and the target molecule bound by the first antibody. It could be expected then, that further reducing the affinity probe size, such as by using only the antigen binding fragment of primary antibodies (Fab, Figure 3.5c), or smaller tags (e.g. nanobodies) would further increase the accuracy and resolution of cellular structures using SMLM.

In conclusion, I developed a new colocalization analysis method (aCBC) and demonstrated that tag sizes of >15 nm decrease the spatial resolution of SMLM experiments, which could not be observed by visual inspection of reconstructed images. Therefore, the method described here is an efficient control of proper fluorescent labeling applied to SMLM that should be added to the classical sample and image quality evaluation procedures. Furthermore, the fusion protein and antibody co-labeling of the same molecule of interest provides an experimental positive control for high resolution colocalization analysis, since the correlation coefficients reflect distances between directly interacting proteins.

3.5 Additional comments and perspectives

Sample preparation considerations for SMLM

In this chapter I presented an optimized sample preparation procedure for multicolor SMLM of nuclear markers. Several aspects of sample handling, however, require special attention.

Fluorescent labeling of intracellular components requires fixation and permeabilization. Cell fixation as performed here is sufficiently stable to yield structures with high resolution (c.f. Chapter 4), however, it does not allow the sample to be imaged more than a day after labeling, and thus only fresh samples need to be used. Increasing the strength of fixation by adding glutaraldehyde could be tested, as it allows better ultrastructural preservation. However, a strong fixative could impede binding of the affinity probe to its epitope, since a dense mesh of crosslinks is created. In this context as well, the development of small (<10 nm) affinity tags would be beneficial.

The immunofluorescence protocol I established uses 5-10 times higher concentration of primary antibodies compared to protocols for confocal microscopy. Indeed, the increase of antibody concentration led to a significant improvement of labeling densities. For instance, lamin staining used to visualize the nuclear periphery in S2 cells (see Chapter 4) appeared continuous in SMLM only at higher antibody concentrations. However, increasing the antibody concentrations may lead to non-specific binding and an optimization step is required to discard staining specificity issues. The double labeling quality control strategy presented in this chapter is well adapted to evaluate specificity of staining at sub-diffraction resolution.

A crucial parameter in dSTORM is the photoswitching environment, which includes the efficiency of oxygen depletion, the stability in pH, and illumination power densities. It is then expected that the photoswitching properties of organic dyes vary from one experimental setup to another. Indeed, I measured fluorophore duty cycles of AF647 and Cy3B in the classical dSTORM buffer (Heilemann et al., 2008) and compared the results to those in literature (Dempsey et al., 2011). I systematically obtained duty cycles which were 10

times higher than the reported values (data not shown). Importantly, the two switching solutions differed only in the buffer that was used to dissolve the enzymatic oxygen scavenger: the first used PBS and the second Tris/NaCl. Whether phosphate (PBS) and Tris have different effects on dye photoswitching parameters will need to be experimentally assessed. However, imaging conditions (laser powers, temperature regulation, sample mounting) are another factor that vary between laboratories and that has an impact on dye performance. It is therefore necessary to optimize the photoswitching cocktail to match the other experimental parameters. Note that even with the optimized buffer composition that I presented in Section 3.1.4 the duty cycles I obtained were still several folds higher than those published, although the dSTORM image quality was satisfactory.

Colocalization analyses and super-resolution

In this chapter I introduced a quantitative method for colocalization analysis of SMLM data. An important prerequisite for efficient detection of colocalization is sample quality. Indeed, colocalization measurements can be impaired by the limited optical resolution (intrinsic property of the microscope), inappropriate sample preparation and mounting (*i.e.* labeling artefacts and refractive index mismatch), and unadapted image acquisition (*i.e.* photobleaching, cross talk between the detection channels, optical aberrations, pixel sampling). Therefore, prior to analyzing colocalization in 2-color images, especially at high resolution, all procedures described in this chapter must be performed with care.

Colocalization analyses using confocal microscopy (LSM) are widely used in biology. It would be of interest to experimentally evaluate to what extent SMLM imaging can improve the resolution of colocalization compared to LSM in a systematic manner. The implication of this comparison may reveal of practical importance for functional investigations of biological functions. Indeed, when the changes of relative localization between two experimental conditions are not detectable in LSM, when is a difference detected by SMLM? Quantitative knowledge on the degree of improvement brought by super-resolution will allow appropriate experimental strategies to be designed. However, in the case of the abundant nuclear protein distributions investigated in this thesis, SMLM is the method of choice.

Dealing with autofluorescence

The imaging buffer in dSTORM influences the excitation/emission cycles of dyes with molecule-specific kinetics and brightness. Importantly, the buffer also prevents the fluorescent molecules from photobleaching during the acquisition at high laser powers, which also appears to be the case for all fluorescent molecules present in the sample. Indeed, autofluorescent cellular components display photoswitching as well. I could observe that endogenous fluorescent molecules in *Drosophila* cells display a photoswitching behavior similar to the affinity probe-coupled dyes in immunofluorescence experiments. Autofluorescence emission is stronger at shorter wavelengths, and while it is minimal in the AF647 detection channel (700 nm) it is well detected in the Cy3B detection channel (600 nm). In conventional microscopy the autofluorescence-related intensity is lower than the specific signal and can be subtracted from the image using unlabeled control samples. In SMLM, though, the single-molecule intensity of autofluorescence events is similar to the specific fluorescent labeling and the density of detections is high. A density of events filtering approach is then unreliable for the elimination of autofluorescent clusters. Consequently, during optimization, dSTORM images acquired with Cy3B should be compared to images of the same structure labeled with AF647 to assess the contribution of autofluorescence to the final image. In this context, for single color structural investigations in dSTORM the use of AF647 is to be privileged.

In *Drosophila* S2 cells, the great majority of autofluorescent events are localized in the cytoplasm, however ~5-10% of the detection clusters are found within nuclear regions. I analyzed the detection dynamics of autofluorescent clusters (preliminary results) and found the events tend to be more clustered in time compared to Cy3B emission. Further comparative analysis of the photoswitching behavior of autofluorescence and Cy3B would allow the former to be discarded from analysis in two-color applications. Alternatively, for two-color imaging in combination with AF647, Cy3B could be replaced with infrared emitting fluorophores. For the moment though infrared dye photoswitching behavior has proven to be suboptimal compared to AF647 and Cy3B due to limited brightness.

Practical aspects of data analysis

All the data analysis programs that have been described in this chapter and some additional features have been combined in a single program (SMLM_2C) with a graphical user interface, which allows for the interactive analysis of SMLM data. When Micromanager is used for localization of events, the analysis can be performed during image acquisitions, which considerably reduces the time required to obtain the experimental results. Currently, the post-processing steps must remain interactive unless a universal and automated image quality evaluation is developed. However, the automation of the colocalization and clustering analyses can be readily performed.

3.6 Materials and methods

3.6.1 Microscope used for multicolor SMLM imaging

The SMLM microscope setup is schematically represented in Figure 3.6 and listed below.

The emission intensity of four lasers with excitation wavelengths of 405nm (OBIS LX 405-50), 488nm (OBIS LX 488-50), 640 nm (OBIS LX 640-100) and 785 nm (OBIS LX 785-50) were controlled using an acousto-optic tunable filter (AOTF, AOTFnC-400.650-TN AAOptics, Orsay France). Two achromatic lenses from Thorlabs (L1a & b) were used to expand the excitation beam and to obtain a homogeneous illumination over fields of view as large as $45 \times 45 \mu\text{m}^2$.

The lasers were focused by L1b, located near the back port of the microscope, and directed by dichroic mirror DM1 to the back focal plane of a 100x Plan-Apochromat oil objective (OBJ, NA = 1.46, Zeiss) mounted on a z-direction piezoelectric stage (PZ, P721.CDQ PIFOC - Physik Instrumente (PI), Karlsruhe, Germany). L1b can be translated perpendicularly to the optical axis in order to shift between TIRF and epifluorescence imaging mode, depending on the experiment. A motorized stage is used to translate the sample perpendicularly to the optical axis.

Autofocus system

To avoid loss of focus during SMLM acquisition, an active autofocus system was built. In a separate path from the other four lasers, the beam of the 785 nm laser is directed towards the objective lens by dichroic mirrors DM1 and DM2. Part of the IR beam is reflected by the sample, collected by the objective and redirected towards a CMOS camera (CDD1545M Thorlabs) using a 50/50 separator cube (half of the light is reflected and half of it is transmitted). The position of the reflected beam is measured and a feedback response is generated on the piezo stage to adjust the position of the objective. Each movement of the sample with respect to the objective is thus detected and a constant distance between the objective and the sample is maintained (resolution of ~ 5 -10 nm over hours). Total reflection is obtained through the lens L2, which is translated perpendicularly to the optical axis. In the beginning of each experiment, a calibration is carried out to ensure that the intensity of the 785 nm laser reflection varies linearly over a course of 600nm around the plane imaged by the objective.

3.6.2 Antibody labeling

For 2-color dSTORM experiments Alexa Fluor 647 (AF647) and Cyanine 3B (Cy3B^{*}) were chosen for their superior performance (Dempsey 2011). In this section, solid-phase and in-solution protocols are described. For convenience solid-phase labeling is performed using the APEX antibody labeling kit (Molecular Probes) with modifications according to the experimental needs (see below). Succinimidyl esters are stored desiccated and prior to use dyes are suspended in anhydrous DMSO.

In the labeling conditions described here, I found that the reactivity of the Cy3B succinimidyl ester is very similar to the succinimidyl ester of the Alexa Fluor 555, which was reported by (Lundberg et al., 2007). Alexa Fluor 555 is provided in the solid-phase labeling kit and after measuring the concentration of the dye from the kit, the same concentration of Cy3B dye can be used.

* Cy3B (supplied by GE Healthcare) is not available in solid phase labeling kits, and one may wish to use antibody affinity purification tips (20 or 200 μ l) from GlySci for instance.

Both labeling protocols require optimization for every new antibody batch. To yield the desired DOL of 1-1.5 the molar ratio and/or reaction time are essentially modulated, as they display a nearly linear dependence with the resulting DOL (Lundberg et al., 2007).

Solid phase labeling

Antibody labeling with AF647 was performed using the protocol and the fluorophore vial from the APEX labeling kit (Molecular Probes), modulating the time of the reaction at room temperature (RT) and pH8.3 in carbonate buffer. Typically 10 µg of IgG added to the affinity column yields a DOL~1.2 for a reaction time of 2h. Labeling with Cy3B is performed using 10 µg of IgG and 5 µg of Cy3B-succinimidyl ester at RT and pH8.3 for 1h30 to yield DOL~1.3.

Labeling in solution

For labeling in solution antibodies are first concentrated using protein concentrators with a molecular weight cutoff (MWCO) of 30 KDa. This step also results in the exchange of the storage buffer with the labeling buffer (PBS, pH7.4). Typically 500 µl of antibody are loaded on a concentrator and 10 times more PBS is added.[†] The vial is centrifuged at 5000 g at 4°C until the volume of buffer reaches ~ 200 µl (this takes ~30 min). The antibody concentration is measured (should be >2 mg/ml) and the amount of dye to add is calculated to obtain an antibody-dye mass ratio of ~30 both for AF647 and Cy3B. The reaction is performed at room temperature for 1h30. Then, Tris pH7.5 is added at a final concentration of 10 mM to stop the labeling reaction. Unreacted dye molecules are removed by buffer exchange for 2-3 times (Zeba spin columns, ThermoFisher), followed by dialysis at 4°C overnight with a membrane (MWCO 3.5 KDa) in PBS. The presence of free dye is evaluated using IF and conventional imaging by monitoring of the signal specificity.[‡] This protocol typically yields DOL ~1-1.3.

[†] The reaction can be scaled up or down for a given antibody while similar efficiency and DOL are achieved, according to the amounts of antibody available as long as the molar ratio between the dye and the antibody is kept constant.

[‡] Free dye molecules adhere preferentially on fixed cells compared to the coverslip surface. For nuclear proteins, the presence of fluorescence signal in the cytoplasm stronger than for unlabeled cells is an indicator of the presence of free dye.

3.6.3 Image registration for SMLM

To obtain the geometrical transformation required to perform image registration, the bead scans performed as detailed in Section 3.3.1 are analyzed as described below. This analysis has been performed using the protocol described in (Churchman and Spudich, 2012). Bead scan images are analyzed with MTT to obtain coordinates of XY localizations (Figure 3.2d). Bead positions with less than 15 localizations per channel are discarded. Once fits have been performed for each image, a pair of locations is known for each of the N positions the bead had in the field of view. These pairs of locations are called control points. The set of control points can be used to calculate a local weighted mean (LWM) mapping that can be applied to any future data point (Goshtasby, 1988). The "cp2tform" command of Matlab calculates the LWM and yields a transformation structure that can be used in other Matlab functions to perform additional transformations. To apply the transformation calculated by cp2tform on the 2-color images to correct for chromatic aberrations, another Matlab function "tforminv" is applied. To estimate the error associated to the LWM transformation, the target registration error (TRE) is calculated as discussed in (Churchman and Spudich, 2012).

3.6.4 Drift correction algorithm

The original drift correction algorithm was previously developed in the team (Fiche et al., 2013b). Lateral drift over the full acquisition period was assessed by plotting the trajectories of fluorescent beads in x and y coordinates over time. For this procedure, only beads detected during the entire acquisition (~30-40 minutes) were employed. Curves were smoothed by a Stavinsky-Golay filter and overlaid by minimizing the distance between each trajectory using the first detected bead as reference. The origin was calculated by averaging the trajectories over the first 100 images, ensuring the drift was equal to zero at t=0min. The trajectories of the other detected beads were used to calculate the reference trajectory. The quality of the drift correction was estimated by subtracting the reference to all the trajectories and calculating the standard deviations along x and y directions. The experimental drift correction precision was typically 3-10 nm, and lower precision experiments were discarded.

3.6.5 Simulations for aCBC

To evaluate the performance of aCBC a series of simulated datasets of two-color localizations with known percentage of colocalization were generated. First the XY positions of the cluster centers from the first channel were generated as a random distribution of points in a circle with a given radius (3 μm in the case presented here). A user-defined percentage of these positions (percentage of colocalization) is also attributed to a subset of the second channel, then, the remaining clusters are generated in the same manner as for channel 1, except that they are not allowed to overlap with channel 1 centers. At each of the generated positions, clusters of localizations with Gaussian distribution are generated. The size of each cluster is determined as values with normal distribution, a mean of 20 localizations and standard deviation of 5. The number of events per cluster follows an exponential random distribution with a user-defined mean value. The generated datasets of localizations are input in aCBC and analyzed as described in the main text.

Chapter 4

SRM applied to the study of Drosophila chromatin folding

The developments I have described in the previous chapter found application in a broader biological study, in which our group investigated the three-dimensional organization of topological domain borders in single *Drosophila* cells using SIM and SMLM. Here I present our results and interpretations in the form of the manuscript that is in preparation for submission. For consistency with the contents of this thesis, some sections of the manuscript have been edited. The discussion has been extended and the materials and methods section has been made complementary to methods in chapter 3.

Super-resolution imaging of topological barriers reveals higher-order chromatin folding principles

Mariya Georgieva*¹, Alessandro Valeri*¹, Diego I. Cattoni¹, Frédéric Bantignies², Delphine Chamousset¹, Pau Farré⁴, Stephanie Déjardin^{1,2}, Jean-Bernard Fiche¹, Andrés Cardozo-Gizzi¹, Olivier Cuvier³, Eldon Emberly⁴, Giacomo Cavalli², Marcelo Nollmann^{1,#}

¹ Centre de Biochimie Structurale, CNRS UMR5048, INSERM U1054, Université de Montpellier, 29 rue de Navacelles, 34090 Montpellier, France

² Institute of Human Genetics, CNRS UPR 1142, Montpellier 34000, France

³ Laboratoire de Biologie Moléculaire Eucaryote, CNRS, Université de Toulouse, Toulouse, France.

⁴ Simon Fraser University, Burnaby, Canada.

*Equal contribution

To whom correspondence should be addressed:

Marcelo Nollmann: marcelo.nollmann@cbs.cnrs.fr

4.1 Summary

Chromosomes from bacteria to humans are organized at the sub-megabase scale into topological domains (TDs). Borders between TDs are constitutive, while their internal organization and their association dynamics are cell-type specific. Recent studies proposed that in mammalian genomes sequential TD borders associate at sites containing convergent sites of the CTCF insulator protein. Here, we combined super-resolution and oligoPAINT technologies to investigate the roles of Beaf-32 -the insulator protein most overrepresented at TD borders in *Drosophila*- in the association of domain boundaries at the single-cell level. We found that sequential and nonsequential barriers in two genomic loci in chromosomes 2L and 3R followed the path expected for a self-avoiding random polymer and did not display specific association. Distances between barriers flanking black TDs followed exactly the model. Interestingly, barriers flanking active TDs exhibited larger distances than those expected by the model, while boundaries surrounding Polycomb TDs were closer, consistent with distances among barriers reflecting the transcriptional activity of the intervening TD. 69 TD barriers homogeneously spread across chromosome 3R appeared in average as single clusters, consistent with constitutive association between TD borders. Finally, the size, number and composition of Beaf-32 clusters imaged at super-resolution are consistent with Beaf-32 clusters representing single TD borders. Beaf-32 clusters surround H3K27me3 Polycomb territories while it overlaps to a large extent with transcriptionally active sites. Overall, our data is in support of a model by which TDs in *Drosophila* are in part formed and maintained by the combined roles of active transcription and self-association of chromatin elements of the same epigenetic types.

4.2 Introduction

The interplay between genome folding and key biological functions such as transcription, DNA repair or replication remains a fundamental question in chromatin biology. Recent genome-wide developments, such as Chromosome Conformation Capture (3C) (Dekker et al., 2002), have unveiled a new level of three-dimensional chromosome architecture. At the sub-megabase scale, chromatin is partitioned into discrete regions called topological domains (TDs) (Dixon et al., 2012; Hou et al., 2012; Nora et al., 2012; Sexton et al., 2012). TDs and TD-like domains have been identified in mammals (Dixon et al., 2012; Nora et al., 2012), the fruitfly *Drosophila* (Hou et al., 2012; Sexton et al., 2012), and more recently in bacteria (Le et al., 2013; Marbouty et al., 2015). Loci within TDs interact more frequently with each other than with loci outside and genes located within the same TD display common epigenetic properties and tend to have coordinated dynamics of expression during differentiation (Le Dily et al., 2014); suggesting a strong link between chromatin structure and transcription (Hübner et al., 2013).

In mammalian genomes, TDs are abundant (>2000), range in size from tens of kb up to 1-2 Mb (median size of ~ 800 kb), and cover >90% of the entire genome, indicating that they constitute a key organizational element of eukaryotic chromosomes. Importantly, TDs were detected at the single-cell level, suggesting that they represent a genuine stable organizational principle of mammalian genomes and not a consequence of ensemble averaging (Nagano et al., 2013). In *Drosophila*, 1100 TDs ranging between tens and hundreds of kb and with a median size of ~60 kb were described in embryonic and Kc167 cells (Hou et al., 2012; Sexton et al., 2012). Interestingly, microscopy experiments showed that loci located within the same TD were on average closer than loci located in different TDs (but at the same genomic distance), suggesting that TDs may represent regions where chromatin is more condensed (Dixon et al., 2012; Nora et al., 2012). Importantly, the positions of a large proportion (~50%) of TD borders were conserved across cell types in *Drosophila* and mammals (Dixon et al., 2012; Hou et al., 2012; Nora et al., 2012; Sexton et al., 2012), and were also highly conserved between mouse and human (Dixon et al., 2012; Vietri

Rudan et al., 2015). This indicates that TDs are to a large degree invariant during differentiation.

In *Drosophila*, protein localization mapping revealed the existence of five principal types of chromatin states (two associated to active transcription and three to repressed genes) that were classified depending on their epigenomic composition (Filion et al., 2010): Yellow and Red chromatin comprise transcriptionally active domains, blue chromatin contains Polycomb domains (PcG, repressed chromatin), green chromatin mainly contains the HP1 and Su(var)3-9 heterochromatin marks (constitutive heterochromatin), and black domains are not specifically associated to any predominant chromatin mark. Interestingly, in *Drosophila* genomic loci within TDs tend to share the same chromatin type (Sexton et al., 2012). Recently, high-resolution genomic studies revealed the existence of smaller, nested domains within TDs in mouse and human (called sub-TDs) (Rao et al., 2014). Sub-TDs were considerably smaller (185 kb in average) than TDs, and approximated the mean size (~ 100 kb) of TDs in *Drosophila*. Sub-TDs could be segregated into six classes according to their associated epigenetic landscape, recapitulating the correspondence between chromatin color and TDs positions observed in *Drosophila*.

Chromatin insulators are genetic elements implicated in nuclear organization and transcription regulation in eukaryotes. Strikingly, in mouse 75% of TD borders were preferentially enriched by the mammalian insulator CTCF (CCCTC-binding factor), by components of the cohesin complex, and by active histone marks (Dixon et al., 2012). These results suggested a role of insulators and active transcription in the formation of TD borders. In *Drosophila*, physical boundaries between TDs were determined to a large degree by insulators (CP190, chromator, BEAF-32), independently of whether the domains flanked contained transcriptionally active or inactive sites (Sexton et al., 2012).

Recently, two studies suggested that borders between sub-TDs and TDs in mammals strongly interact forming chromatin loops (Rao et al., 2014; Vietri Rudan et al., 2015). These looping interactions seem to be mediated by converging CTCF sites and by cohesin and represent the primary behavior of a large proportion ($\sim 50\%$) of sub-TD borders. Thus, in mammals CTCF seems to play a role as an insulator at TD borders and as a looper at sub-TD borders. The internal folding and interaction patterns of TDs are highly cell-type specific and are not an evolutionarily invariant (Rao et al., 2015; Vietri Rudan et al., 2015),

indicating that TDs may represent functional domains of long-range gene regulation.

4.3 Results

4.3.1 Imaging single TD barriers at the single-cell level

To visualize individual TD barriers at the single cell level, we combined oligoPAINT labeling (Beliveau et al., 2015) with super-resolution imaging. Each TD barrier was labeled with genomic specificity using oligoPAINT technologies (see Experimental Procedures) and visualized by three-dimensional structured illumination microscopy (3D-SIM), a method providing an eight-fold enhancement of resolution with respect to conventional microscopies (Schermelleh et al., 2008). Specific TD barriers were selected and labeled in two chromosomal regions within chromosomes 2L and 3R. The region in Chr. 2L contained a yellow TD surrounded by two black TDs, while the region in Chr. 3R exhibits multiple Polycomb (blue) TDs flanking a black domain (Hou et al., 2012; Sexton et al., 2012) (Figure 4.1a-b). In most cases, barriers between TDs contained short active regions (yellow/red chromatin).

Seven oligoPAINT libraries were designed (L1 to L7) with a minimum coverage of 20 kb and a minimum of 267 probes per library (median of 516 probes spanning ~ 40 kb, Figure 4.1g, see Design of oligoPAINT libraries). S2 cells were fixed and labeled by oligoPAINT (Figure 4.1a, right panel) using a modified protocol (Bantignies and Cavalli, 2014; Beliveau et al., 2015) (see Preparation of sample slides for FISH and 2 color-FISH). Individual oligoPAINT libraries were detected using a Matlab based routine (see Analysis of 3D-SIM data) and appeared mostly (~ 55%) as one or two small, single foci when visualized by confocal microscopy or 3D-SIM (Figure 4.1c). In a population, cells displayed in most cases a single focus but exhibited a degree of heterogeneity (Figure 4.1c-d, Figure S 4.1a and Figure S 4.1h). These results suggest that despite the different ploidities of chromosomes 2 and 3 (six, and four, respectively in S2 cells), barriers are mostly paired independently of chromatin color. Individual foci displayed a size-computed as the lateral full width at half maximum of the fluorescence signal - smaller or comparable to the resolution of 3D-SIM (Figure 4.1,e-f and Figure

4.1i-j), consistent with barriers being mostly paired at this spatial resolution. When imaged by single-molecule localization microscopy (SMLM), barriers appeared often as extended regions smaller than ~ 100 nm in length (Figure 4.1k and Figure S 4.1b), in agreement with sizes from 3D-SIM. Finally, to validate this approach, we used SMLM combined with oligoPAINT to image the bithorax complex (BX-C), a large (~ 350 kb) chromosomal region of polycomb chromatin in chromosome 3R (Figure 4.1a, right panel). In this case, we observed considerably larger structures ~ 500 nm in size (compare upper and lower panels of Figure 4.1l and Figure S 4.1c), consistent with previous studies (Beliveau et al., 2015). Overall, these results indicate that despite chromosome copy number, barriers display a large degree of homologous pairing.

4.3.2 Local organization of barriers at super-resolution

We investigated whether consecutive or nonconsecutive barriers interacted by forming long-range loops. Because of averaging effects, ensemble methods would only tend to detect interactions appearing in a large proportion of cells in a population (i.e. constitutive interactions), while rare interactions would be averaged out. Thus, we used our combination of oligoPAINT and SRM to directly determine, at the single-cell level, the distribution of distances between TD barriers in the genomic regions described above (Figure 4.1a). Each pair of libraries was labeled with different colors and imaged by 3D-SIM and dSTORM (Figure 4.2a). The distance between libraries was determined by calculating the distance between nearest oligoPAINT foci of different colors from volumetric 3D-SIM, independently of the number of foci per cell (Figure 4.2b). Mean distances between libraries correlated to the genomic separation between TD barriers (Figure 4.2b).

First, we measured the distribution of distances between consecutive barriers. A typical example is observed in Figure 4.2c (distributions for all combinations are shown in Figure S 4.2). This distribution did not depend on the combination of colors used for labeling each library (data not shown). To estimate the proportion of consecutive libraries overlapping in space, we calculated for each distribution the percentage of distances below the resolution of 3D-SIM (Figure 4.2c). Strikingly, we found that only a very small percent of barriers localized in space at any given time ($5 \pm 2\%$, Figure 4.2d). This small degree of co-localization did

not depend on the epigenetic state of the TD flanked. Finally, the probability of interaction between non-consecutive barriers was similarly small (Figure 4.2d). Overall, these results are inconsistent with constitutive interactions between consecutive or non-consecutive barriers, at least for the two genomic regions explored.

Next, we determined the mean distance between barriers and its dispersion. The mean distance between barriers increased monotonically with genomic distance (Figure 4.2b-e). This finding is inconsistent with constitutive interactions between neighboring barriers, as this model would predict a non-monotonous dependence of physical with genomic distance. The mean distances between barriers located in different chromosomes were comparable to the size of the nucleus, indicating that the sub-nuclear localizations of the two genomic regions explored were uncorrelated. The dependence of physical and genomic distances between barriers within the same chromosome (Figure 4.2b) can be well fit by a self-avoiding random walk model (Mirny, 2011), consistent with previous studies (Bickmore, 2013). Interestingly, several distances considerably deviated from the mean distribution. Distances between barriers flanking yellow chromatin TDs (active) were higher than that expected for black or blue chromatin TDs (Figure 4.2e). Notably, the distance encompassing barriers 5-7 in chromosome 3R were considerably shorter than that expected, consistent with association between neighboring blue chromatin TDs (Sexton et al., 2012) (see inset in Figure 4.2e). Inversely, distances between libraries 1-3 and 2-4, which encompass a yellow and a black domain, display longer than expected distances (Figure 4.2e).

Interestingly, the dispersion of the physical distance distributions increased almost linearly with genomic distance between barriers (Figure 4.2f). This behavior is expected as the longer the distance probed the more the measurement accumulates dispersion due to heterogeneity (intrinsic, functional, or dynamic) in the structure of the chain. In fact, the linearity of this dependence allows us to extract an average dispersion per genomic distance unit of $\beta = 0.9 \pm 0.3$ nm/kb. Strikingly, the dispersion between barriers flanking yellow TDs displayed a considerably larger value of β (ranging between 1.5 and 3), consistent with active chromatin displaying a larger degree of structural/dynamic heterogeneity. In contrast, barriers flanking blue and black TDs displayed average values of β whereas barriers between TD-e and BX-C (Figure 4.1a)

showed a considerably lower value of β , consistent with less structural heterogeneity in distances between these TDs (Figure 4.2f).

4.3.3 Chromosomal organization of barriers

Next, we extended our approach to investigate the organization of topological barriers at the chromosomal level. For this, we engineered an oligoPAINT library with 69 different barriers spanning chromosome 3R (Figure 4.3a). Barriers were not necessarily sequential, but displayed a strong ChIP-chip signal for Beaf-32, and were homogeneously covered ($\sim 20 \pm 1$ kb) by oligoPAINT probes (263 ± 30 in average, Figure 4.3a). In most cases, barriers contained mostly yellow chromatin, while chromatin between barriers was predominantly black (Figure 4.3b). Barriers were homogeneously distributed over chromosome 3R, with an average barrier-to-barrier distance of 320 ± 90 kb (Figure 4.3c).

Imaging of this library by 3D-SIM consistently led to the detection of a large number of small clusters within the nucleus (Figure 4.3d). The average size of clusters corresponded to the 3D-SIM resolution (Figure 4.3e-f). Their 3D distribution was random, as shown by the normalized Ripley's function (Figure S 4.3e). The radial density of clusters measured from the nuclear envelope was homogeneous between 700-1200 nm and decayed close to the nuclear periphery and to the center (Figure 4.3g). The low percentage of oligoPAINT probes located close to the nuclear periphery ($< 3\%$ within 200 nm) indicates that barriers in chromosome 3R are mostly localized in the interior of the nucleus, despite the large ($> 88\%$) percentage of barriers flanking black domains.

Chromosome 3 in S2 cells is tetraploid, and in average we observed a pairing of $\sim 55-70\%$ (i.e. proportion of single clusters per barrier, Figure 4.1c). From the distribution in the number of foci per library, one can estimate the total number of barriers as $N = 69 \times \sum_{k=1}^4 (p_k \times k)$, where p_k represents the proportion of cells displaying k foci (Figure 4.1c). For the three barriers labeled with single oligoPAINT probes (libraries 5-7, Figure 4.1a), one can estimate that a mean of 100, 91 and 110 barriers should be detected per cell provided barriers do not interact together. To test if this is the case, we measured the distribution in the number of clusters per cell for the Chr. 3R library (Figure 4.3a). Strikingly, we observed 98 ± 26 clusters per cell (Figure 4.3h), consistent with barriers in our oligoPAINT library showing little or no looping interactions.

4.3.4 Chromatin insulators and nuclear distribution of TD frontiers

A large proportion of TD barriers in the *Drosophila* genome are bound by insulators (Sexton et al., 2012). Thus, imaging insulator proteins at super-resolution provides a complementary method for directly visualizing the organization of TD barriers at the single cell level. We imaged Beaf-32, as this is the insulator binding protein displaying the highest enrichment in domain borders. By conventional microscopy, Beaf-32 displayed a diffuse nuclear signal (Figure 4.4a, and Figure S 4.3a), large clusters at the periphery were only observed under osmotic shock conditions as shown by (Schoborg et al., 2013) (Figure S 4.4a). Thus, we turned to super-resolution microscopies. First, we used 3D-SIM to image Beaf-32 labeled by immunofluorescence. Beaf-32 assembled in clusters within the 3D volume of the nucleus (Figure 4.4b). Beaf-32 also assembled in clusters displaying similar distributions and sizes when imaged by stimulated emission depletion microscopy and by SMLM (Figure S 4.3b and Figure S 4.5). Clusters had the size of the 3D-SIM resolution limit (~ 120 nm lateral, and 250 nm axial) (Figure 4.4c and Figure S 4.3c). The nuclear radial distribution of Beaf-32 clusters was very similar to that observed for TD barriers in chromosome 3 (Figure 4.4d and Figure 4.3d), consistent with Beaf-32 clusters representing Beaf-32 bound to TD barriers. To further test this hypothesis, we performed multi-color 3D-SIM where we simultaneously imaged Beaf-32 and single TD barriers bound by Beaf-32 and labeled by oligoPAINT (libraries 4, 6 and 7, Figure 4.1). In this case, we observed an almost complete localization (>93 %, $N > 15$) between TD barriers and Beaf-32 clusters (Figure 4.4e).

To further investigate the size of Beaf-32 clusters, we turned to two-color dSTORM (2c-dSTORM), a method that provides a considerably larger resolution than 3D-SIM. Beaf-32 clusters were found within the nuclear lamina and exhibited a homogeneous distribution (Figure 4.5a). To ensure that cluster sizes and distributions were not affected by the antibody binding efficiency, we performed PALM in cultures transiently transfected with a functional Beaf-32-mEos2 fusion (Figure 4.5b, and Figure S 4.4b). In order to test whether Beaf-32 localizations were randomly distributed, we used the normalized Ripley function (Ripley, 1977). In average, localizations were grouped in clusters of ~ 50 nm in size, and the distribution of localizations considerably deviated from a random

distribution (Figure 4.5c). A similar distribution was obtained from PALM clusters (Figure S4c). To obtain a better estimate of cluster sizes, we applied a clustering algorithm (Fiche et al., 2013b). By both 2c-dSTORM and PALM, Beaf-32 cluster sizes were very similar (42 ± 5 and 45 ± 5 nm, respectively, Figure 4.5d and Figure S4.5d) and slightly larger than the pointing resolution under our conditions (30 nm). Finally, to obtain a relative quantification of the number of Beaf-32 molecules within each cluster (cluster composition) we turned to the method developed by Annibale et al. (Annibale et al., 2011b). In average, Beaf-32 clusters contained 4.8 ± 1 molecules, and most clusters had a similar composition (Figure 4.5e and Figure S 4.4e). All in all, the homogeneity, size and composition of Beaf-32 clusters are consistent with individual TD barriers, and inconsistent with aggregation of TD barriers within the cell.

To further test this hypothesis, we counted the total number of Beaf-32 clusters per nuclei by 3D-SIM. Interestingly, the distribution in the number of Beaf-32 clusters is peaked and well defined (Figure 4.5f), with a mean of 440 ± 10 clusters per cell (mean \pm sem). Beaf-32 was shown to bind to thousands of binding sites genome-wide (Emberly et al., 2008). From the genomic positions of these binding regions and the number of reads, we estimated a total of ~ 1500 clusters containing CGATA binding sites in S2 cells. But due to the limited resolution of 3D-SIM, sites that are close together in genomic distance will appear as a single cluster when imaged at the single cell level. Thus, this limitation will considerably lower the expected number of Beaf-32 clusters that should be detected in our imaging conditions. The reduction in the number of sites that should be detected by microscopy can thus be estimated by counting the number of total sites that are found within a genomic window of a specified size. We estimated the number of clusters that should be detected per cell as a function of genomic window size and plotted the results as a two-dimensional histogram (Figure 4.5g), where color represents enrichment in Beaf-32 signal. It is clear that even for low enrichments ($\text{Log} < 2$) and considerably small genomic window sizes (< 10 kb), the number of sites detected per cell is of the same order as that detected by 3D-SIM (440 ± 10). These results are fully consistent with TD barriers not displaying a large degree of constitutive looping at the single-cell level.

4.3.5 Epigenetic organization of Beaf-32 clusters

Next, we used two-color SRM to investigate the organization of Beaf-32 clusters with respect to different transcriptional activity markers at the single-cell level. Previous studies identified a large degree of correlation between RNAPII and Beaf-32 binding sites, and a very low degree of correlation of Beaf-32 with silent chromatin regions (Bushey et al., 2009; Emberly et al., 2008). However, these correlations were characterized by ensemble, genome-wide methods unable to establish a direct interaction between these factors. First, we used 2c-dSTORM to determine the organization of Beaf-32 clusters with respect to inactive chromatin regions labeled by H3K27me3. To determine the degree of co-localization between factors, we implemented an automatic variant of localization-based co-localization analysis (aCBC, see Figure S 4.5a-f and Quantitative analysis of colocalization). Notably, H3K27me3 tends to spread over large territories spanning hundreds of nanometers (Figure 4.6a, N=20). These territories are typically devoid of Beaf-32, and are composed of semi-continuous fibers. Interestingly, Beaf-32 clusters are often found at the borders of H3K27me3 territories, consistent with their role in demarcating barriers between active and inactive domains (Figure 4.6a, bottom right). This low degree of co-localization between Beaf-32 and H3K27me3 clusters is reflected by a very small percentage of $aCBC > 0.5$ (Figure 4.6d), and demonstrates that Beaf-32 clusters do not occupy H3K27me3 territories at the single-cell level. This finding is consistent with Beaf-32 being overrepresented in regions occupied by active promoters (Emberly et al., 2008; Nègre et al., 2010).

To test this further, we imaged Beaf-32 and paused RNAPII by two color dSTORM. In contrast to H3K27me3, the distribution of RNAPII clusters is more homogeneous and Beaf-32 often co-localizes with active RNAPII hotspots (Figure 4.6b, N=30). Quantification of the co-localization coefficient indicates that Beaf-32 clusters are consistently localized at sites of active transcription (Figure 4.6d). It is worth noting, however, that while most Beaf-32 clusters are close to RNAPII clusters, very often RNAPII clusters do not contain Beaf-32. Overall, these data indicate that at the single-cell level Beaf-32 clusters, and by extension Beaf-32 barriers, are very often at transcriptionally active hotspots while many other transcriptionally active regions are not occupied by Beaf-32.

Finally, we investigated the spatial localization of Beaf-32 clusters with respect to blue chromatin domains marked by Polycomb. Polycomb regions are more sparse and more concentrated spatially than either RNAPII or H3K27me3 (Figure 4.6c, N=30), in agreement with the inhomogeneous distribution of blue domain sizes (i.e. BX-C and Antennapedia comprise the largest domains by far). The number of Polycomb clusters is considerably lower than that of other marks (~ 20 clusters/cell, N=40), consistent with the relatively lower proportions of blue domains with respect to yellow/red or black domains. SMLM images reveal Beaf-32 clusters do not spatially localize with blue domains at the single cell level, reflected by a very low colocalization coefficient (Figure 4.6d). BX-C most often represents the largest Pc body in the cell (Cheutin and Cavalli, 2012). It is worth noting that Beaf-32 clusters localize to the periphery of BX-C bodies (Figure 4.6c), consistent with the presence of Beaf-32 at barriers flanking BX-C and other blue TDs.

4.4 Discussion

Recent studies have proposed that a predominant mechanism for the formation of mammalian sub-TDs involves looping between sequential TD barriers (Rao et al., 2014; Vietri Rudan et al., 2015). In this study, we devised an experimental strategy to test whether this mechanism is likely to be predominant in *Drosophila*. This strategy involved directly measuring the distance between consecutive and non-consecutive TDs at the single cell level by sub-diffraction resolution microscopy. The mean distance between TDs and the dispersion of distances increased monotonically with genomic distance, indicating a stable mean structure of the chromatin fiber. The dependence of physical versus genomic distance scaled with a coefficient characteristic of the self-avoiding random walk typical at short distances (Mirny, 2011) (theoretical exponent: 0.6, experimental: 0.65 ± 0.1). This finding is inconsistent with a 'rosette' model in which all TD barriers coalesce by specific interactions (Figure 4.7a), as this would require the physical distance between TD barriers not to increase with genomic distance. In addition, our observation is inconsistent with a 'consecutive looping' model in which only consecutive TD barriers loop (Figure 4.7b), as this model predicts a consistently lower distance between consecutive TD barriers than between non-consecutive barriers. These traits were not observed in our data

(Figure 4.7e). Moreover, the physical distance between domain borders was correlated to the size of the TD being flanked, and barriers co-localized only in a very low fraction of cells (< 2.5%, Figure 2d), in favor of a boundary organization that is distinct from constitutive looping.

These observations, however, are fully compatible with a model in which TD barriers do not loop ('TD condensate' model, Figure 4.7c). In addition, this model is consistent with our observations that the distance between barriers reflects the epigenetic state of the TDs they flank: (1) barriers between black TDs follow the self-avoiding random walk behavior; (2) distances between barriers flanking yellow (active) TDs are consistently larger than the prediction from the theoretical model, in agreement with the expected dynamic and decondensed conformation of transcriptionally active chromatin; while (3) in some instances distances flanking TDs with the same epigenetic state (e.g. blue or Polycomb) are shorter than theoretically predicted (Figure 4.2e) consistent with the tendency of polycomb chromatin TDs to form homotypic interactions (Bantignies et al., 2011; Jost et al., 2014; Sexton et al., 2012). Overall, these results are consistent with yellow, blue and black chromatin TDs displaying an architecture correlating with their transcriptional activity. Therefore, TD borders would not establish a rigid scaffold that spatially confines TD organization. Rather the relative positions of boundaries are affected by the chromatin domains they encompass. Importantly, the distances between borders accurately reflected the underlying chromatin structure at the single cell level, which argues in favor of stable and possibly predictable genome architecture.

To test for border interactions within larger portions of the genome, we labeled 69 boundaries and calculated the number of fluorescent foci detected. Strikingly, the mean total number of foci per cell was fully compatible with the expected values for individual non-interacting borders and could account for the degree of homologous chromosome pairing, consistent with the TD condensate model. To investigate the degree of TD border interactions at the level of the whole genome, we took advantage of the very significant binding enrichment of the insulator protein Beaf-32 at domain boundaries. Quantitative analysis of 3D-SIM images revealed ~450 Beaf-32 foci per cell, a number compatible with the total number of Chip-seq binding sites that should be visible in our imaging conditions. In addition, we observed that Beaf-32 clusters are small (~45 nm) and contain a small number of proteins (~4-5). Beaf-32 binding sites (CGATA motif) display a

linearly clustered distribution along the genome, with triplets of sites often found within regions of 1kb (Emberly et al., 2008). Thus, these results and observations are inconsistent with rosette or consecutive looping models representing constitutive determinants of TD formation, as these models would require larger Beaf-32 clusters with many more proteins per cluster being detected at the single-cell level.

Although looping does not seem to be the mechanism that drives genome partitioning into domains of preferential chromatin contacts, boundaries could still be a factor in the establishment of TDs. For instance, TD borders are sites of active transcription. Thus, the high occupancy of architectural proteins, the transcription machinery, and chromatin remodelers at domain boundaries could confer them particular structural properties, such as increased rigidity that would constrain chromatin interactions to either side of the border (Figure 4.7c). Such a mechanism, involving multiple factors is compatible with the partial or no perturbation of TD structures upon knockdown of CTCF (Zuin et al., 2014a), or the ablation of the H3K27me3 epigenetic marks (Nora et al., 2012). A structural characterization of individual boundaries with SMLM and a proteomic investigation of border-associated factors would shed light on possible molecular mechanisms of TD formation.

Previous ChIP-chip/seq studies have shown that RNAPII is often detected at regions close to Beaf-32 binding sites in an ensemble population of cells (Bushey et al., 2009; Emberly et al., 2008). This observation suggested a role of Beaf-32 in transcriptional activation (Liang et al., 2014). To test whether Beaf-32 is constitutively co-localized to active RNAPII sites, we measured the spatial correlation of Beaf-32 and of paused RNAPII at the single-cell level using super-resolution microscopy. As expected from genome-wide studies, Beaf-32 and RNAPII displayed a high degree of colocalization at the single-molecule level. In contrast, Beaf-32 did not occupy the same regions as other marks (e.g. H3K27me3 or Pc). As for Beaf-32, the RNAPII distribution pattern did not indicate an important degree of spatial clustering, as previously observed by SMLM for mammalian RNAPII (Cisse et al., 2013; Zhao et al., 2014). Rather, RNAPII was very abundant within the nuclei of S2 cells, with no sites of particular enrichment that would resemble transcription factories. In addition, the nuclear distribution of both Beaf-32 and RNAPII was homogeneous (Figure 4.6). These observations are in line with the high gene density of the *Drosophila* genome compared to

mammals where transcriptionally active loci may be found close in 3D space both because of the smaller genome and the smaller size of the nucleus. Furthermore, the absence of remarkable RNAPII clustering may be related to the fast export of mRNAs to the cytoplasm as could be seen by fluorescent staining of polyA tails of mRNAs using RNA-FISH (Forler et al., 2004). Indeed, the lower fraction and size of introns in the *Drosophila* genome may lead to faster rates of mRNA synthesis and export, and thus a low degree of accumulation of paused RNAPII at promoters, since initiation and elongation are coordinated.

Evidence from microscopic and Hi-C methods have predicted that active and inactive chromatin domains are organized at the single-cell level into compartments (Cremer et al., 2015; Dekker and Heard, 2015; Lanctôt et al., 2007). Most Beaf-32 binding sites (>85%) mark the position of TD barriers. The majority of barriers marked by Beaf-32 represent active chromatin (yellow). Thus, we used Beaf-32 as a probe to image the nanoscale distribution of active domain boundaries, while simultaneously imaging other epigenetic regions by H3K27me3, Pc, and active RNAPII. Remarkably, we observed for the first time at the single-cell level that H3K27m3 distributed in well-defined territories with a typical size of 100-400 nm surrounded by channels depleted of H3K27me3 and populated by Beaf-32-labeled domain boundaries (Figure 4.6a). This constitutes strong experimental support for active/repressed TDs partitioning into distinct territories (or 'globules') with active barriers expelled to the periphery (Jost et al., 2014). These territories were not easily observed by microscopic methods in the past most possibly due to the limited resolution of diffraction-limited methods. Simultaneous imaging of Beaf-32-labeled domain boundaries together with active RNAPII or Polycomb is consistent with these observations, as they show that active TD barriers labeled by Beaf-32 intermingle with regions rich in active RNAPII, while they are segregated from Polycomb-rich regions.

4.5 Perspectives and outlook

Our results suggest looping is not a constitutive property of Beaf-32 in *Drosophila*, since a very low number of molecules was counted per Beaf-32 spot. To date there is no homolog of Beaf-32 found in mammals, which could account for the different landscapes depicted by CTCF in mammals and BEAF-32 in *Drosophila*. Beaf-32 and CTCF although both highly enriched at TAD borders and displaying looping activity and physical insulation of genomic regions, may be involved in distinct mechanisms that differently influence chromatin folding. In favor of this hypothesis is the observation that during mitosis a subset of Beaf-32 remains bound to chromosomes (data not shown), which is not the case of mammalian CTCF until telophase (Zuin et al., 2014b).

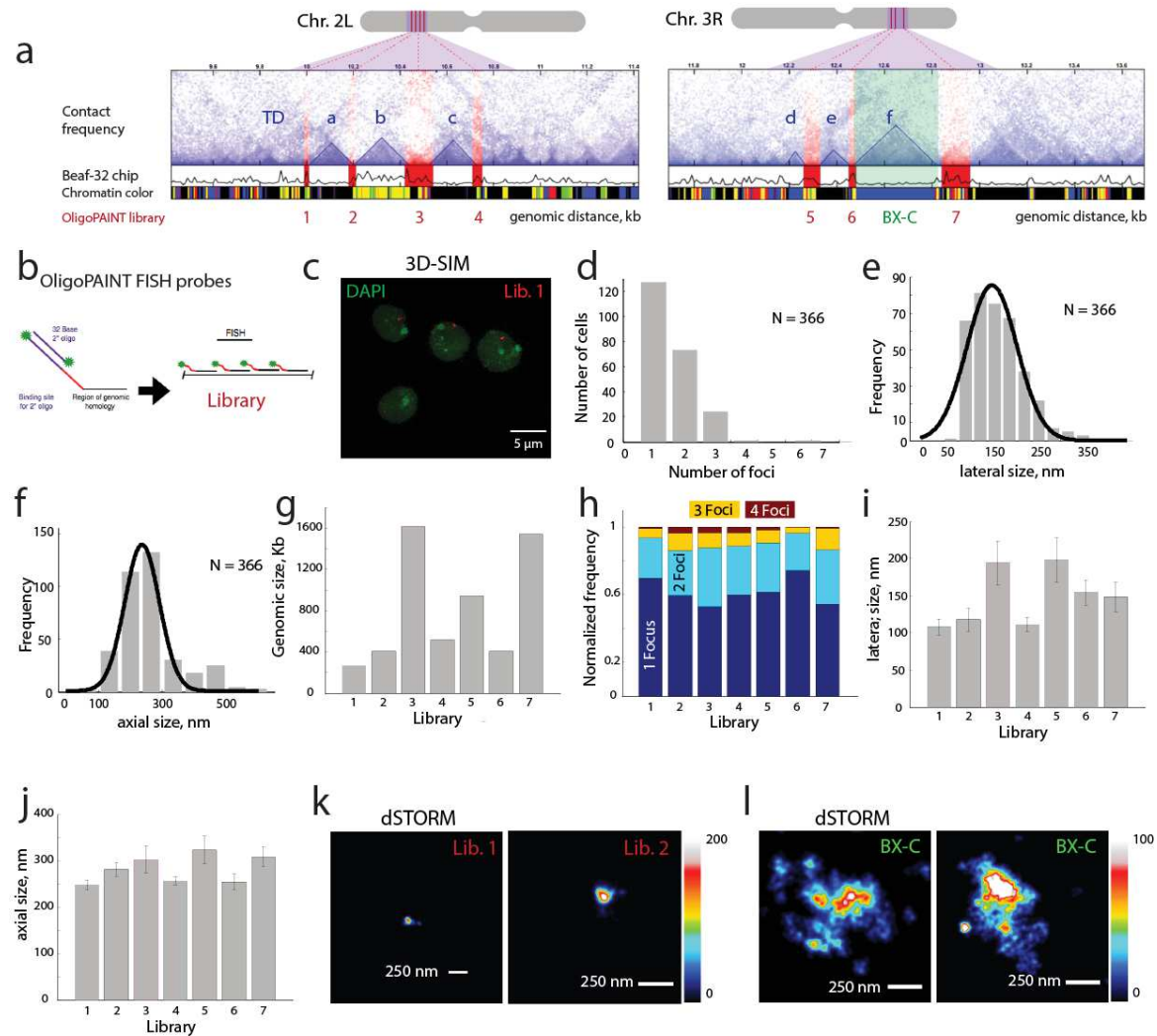
Alternatively, TAD formation itself may be a result of different mechanisms between species. Despite the elevated gene homology between *Drosophila* and human (~60%), and the similarities between developmental programs, there are various genomic differences that could reflect or play a role in the divergence of genome organization pathways. As mentioned above, the *Drosophila* genome has a significantly lower proportion of non-coding sequences compared to mammals. Furthermore, while in *Drosophila* one function is related to one gene, there is an important level of gene duplication in mammals. Homologous chromosomes tend to be paired in *Drosophila* (~50-60%) but are mostly separated in mammalian species. In mammals constitutive heterochromatin seems to preferentially localize to the nuclear periphery, while it does not seem to be the case in *Drosophila* S2 cells (Figure 1.1). In mammals, but not *Drosophila*, cohesin is also significantly found at TAD borders, although again, the majority of binding sites are not at borders (Sexton and Cavalli, 2015b). Finally, only CTCF has been found to have an insulating function in mammals, whereas in *Drosophila*, no less than 11 IBPs have been identified and possibly more will be discovered. In this context, it would be interesting to monitor mammalian TAD borders organization and the localization of CTCF with super-resolution microscopy. A higher frequency of pairwise contacts, for instance, would suggest distinct mechanisms of TAD formation and maintenance between organisms.

It is yet to be demonstrated which factors determine genome folding into TADs, and functional tests would allow essential components for the topological organization of chromatin to be identified. Recently, *Drosophila* cells were perturbed by heat shock which resulted in a global transcription repression and a genome-wide redistribution of architectural proteins from TAD borders to the TAD interior which also changed chromatin topology (Li et al., 2015). These results indicate that on average chromatin architecture would efficiently be remodeled in response to environmental stimuli. Observing the physical impact of stress on the chromatin fiber at the single cell level would inform on potential mechanisms that drive the interplay between genome topology and gene regulation. For instance, how do distances between borders change upon general transcription repression? Do borders flanking different epigenetic regions respond differently? One could think of border interactions as a scaffold for gene compaction, in agreement with the radial loop model discussed in Chapter 1. In this line of thought, what is the role of condensins? An experimental model to test for such effects would be chromatin compaction during mitosis. Optimization of the FISH protocol would then be possibly required. Furthermore, depletion of architectural proteins binding to specific loci, alone or in combination, would inform on the essential components to establish or maintain TADs. Deletion of subsets of binding sites through genome editing may reveal a fruitful strategy to investigate molecular mechanisms at the level of single genes.

Genome-wide techniques yield probabilistic maps of chromatin interactions, and identify protein candidates for the functional regulation of genome architecture. The impressive amounts of quantitative information that are generated provide a powerful guide to deeper mechanistic investigations. With the development of super-resolution microscopy technologies, interphase chromatin structure and function can be investigated at the molecular scale and reveal the mechanisms that drive interphase chromatin dynamics.

4.6 Main Figures

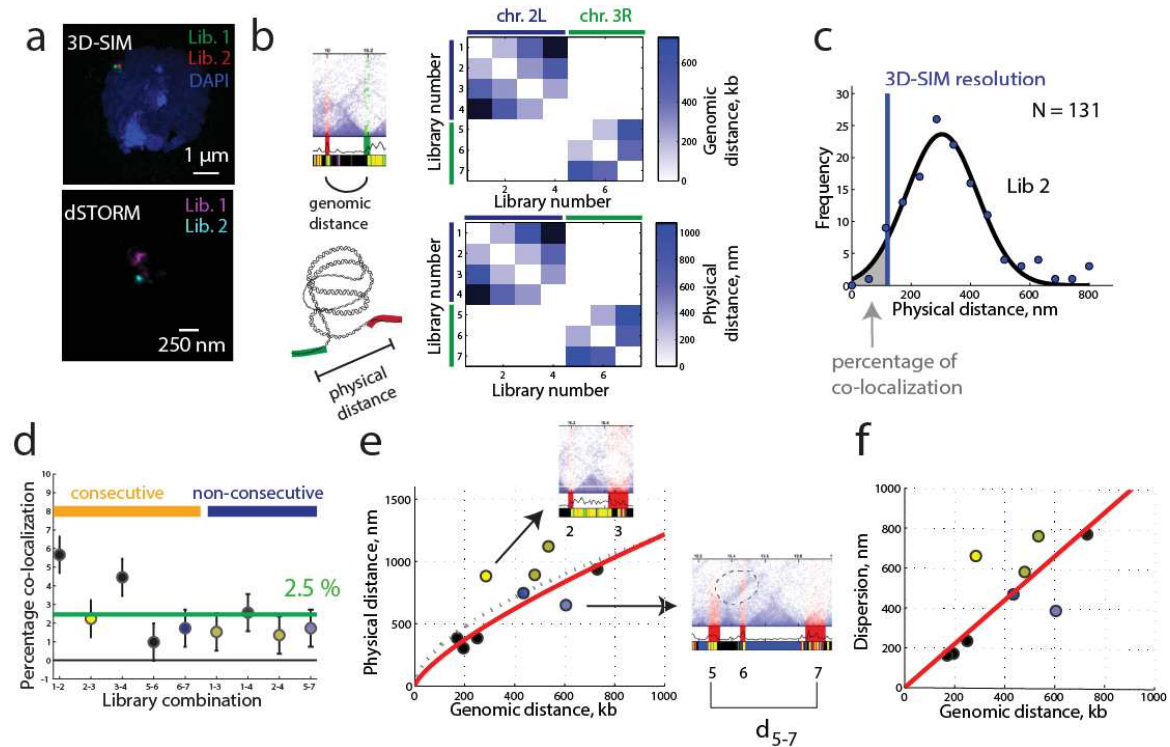
Figure 4.1 - Imaging single TD barriers at the single-cell level



Hi-C normalized map for *Drosophila* embryos in ~ 2 Mb regions of chromosomes 2L and 3R (Sexton et al., 2012). Contact map is rotated by 45° from conventional matrix representation. Y-axis denotes contact frequency and x-axis denotes genomic distance in kb. Bottom panel shows Chip-Seq profile of BEAF-32 and color-coded chromatin organization according to protein binding profiles (Filion et al., 2010). Red shadowed regions indicate the genomic position and size of oligoPAINT libraries designed to label TD barriers. **(b)** Labeling strategy using oligoPAINT FISH probes. **(c)** Characteristic example of an individual nucleus imaged by 3D-SIM (see Movie S1). **(d)** Representative histogram depicting the frequency of detection of individual oligoPAINT libraries (number

of foci) detected from 3D-SIM images for library 2 (see Extended Experimental Procedures for details). N indicates the number of cells analyzed. The relative number of foci detected per cell for all libraries (1-7) is depicted in Fig. 1g. **(e-f)** Histograms of (e) lateral and (f) axial distribution of sizes for library 2. A Gaussian distribution was fitted to the experimental distribution (black solid line) and the full width at half maximum value (FWHM) of the profiles in the lateral and axial directions were computed to estimate the sizes of the libraries. The mean FWHM for all libraries (1-7) are depicted in Fig. 1h-i. **(g)** Genomic region spanned by each oligoPAINT library. **(h)** Average relative proportion in the number of number of foci detected per cell from 3D-SIM images for all libraries. **(i-j)** Lateral (x/y) and axial (z) distribution of sizes for all libraries obtained as described in panels d-e. **(k-l)** STORM image of libraries 1, 2 (k) and BX-C (l). TD barriers often appear as single foci with a lateral size of ~50-100 nm. In contrast, BX-C appears as a distributed structure spanning hundreds of nm in size.

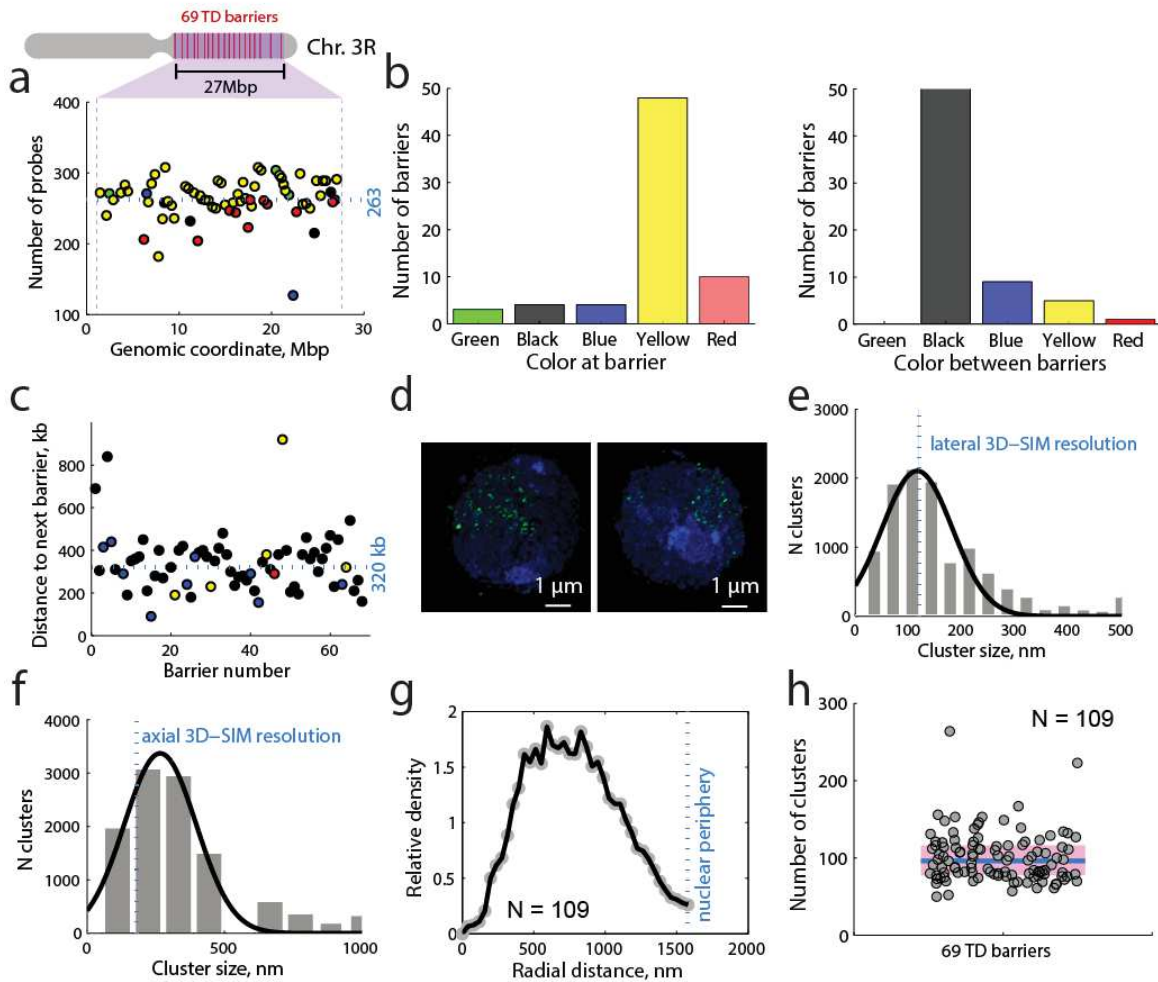
Figure 4.2 - Local organization of barriers at super-resolution



Typical two-color 3D-SIM and STORM images of cells simultaneously labeled with two oligoPAINT libraries. **(b)** Upper matrix: genomic distance between any two given combination of libraries. No genomic distance is displayed for libraries between different chromosomes. Lower panel: mean physical distance between combinations of libraries determined from 3D super-resolution FISH imaging. **(c)** Distribution of distances between libraries 1 and 2 (blue circles). A Gaussian fit (black curve) was used to determine the mean and standard deviation (see panels e and f). Cyan shaded area represents the area under the curve from zero to the resolution of 3D-SIM (120 nm), and provides an estimate for the maximum degree of co-localization between libraries. **(d)** Maximum degree of co-localization for different combinations of libraries. Combinations are sorted depending on whether they measure distances between consecutive (left) or non-consecutive TDs (right). Solid colors (left) represent the color of chromatin of the TD being flanked by a given combination of libraries. Shaded colors (right) are shown when libraries flank several TDs with mixed colors (shaded yellow: mix of a yellow and a black TD; shaded blue: mix of a blue and a black TD). **(e)** Distribution of physical versus genomic distance. Color code are identical to those used in panel (d). Magnified regions display the contact map between libraries 2 and 3 (top), and between libraries 6 and 7 (right). A fit for a self-avoiding random walk model ($d = a \times s^b$, where d is the physical distance, s is the genomic distance, and b is the fractional exponent) is shown as a dashed line (all points fitted, fractional exponent: 0.6) or as a red line (only

distances between barriers flanking black TDs are fitted, fractional exponent: 0.7). **(f)** Standard deviation of the distribution of distances as a function of genomic distance. Red line represents a linear fit passing through the origin. Color code is as in panel d.

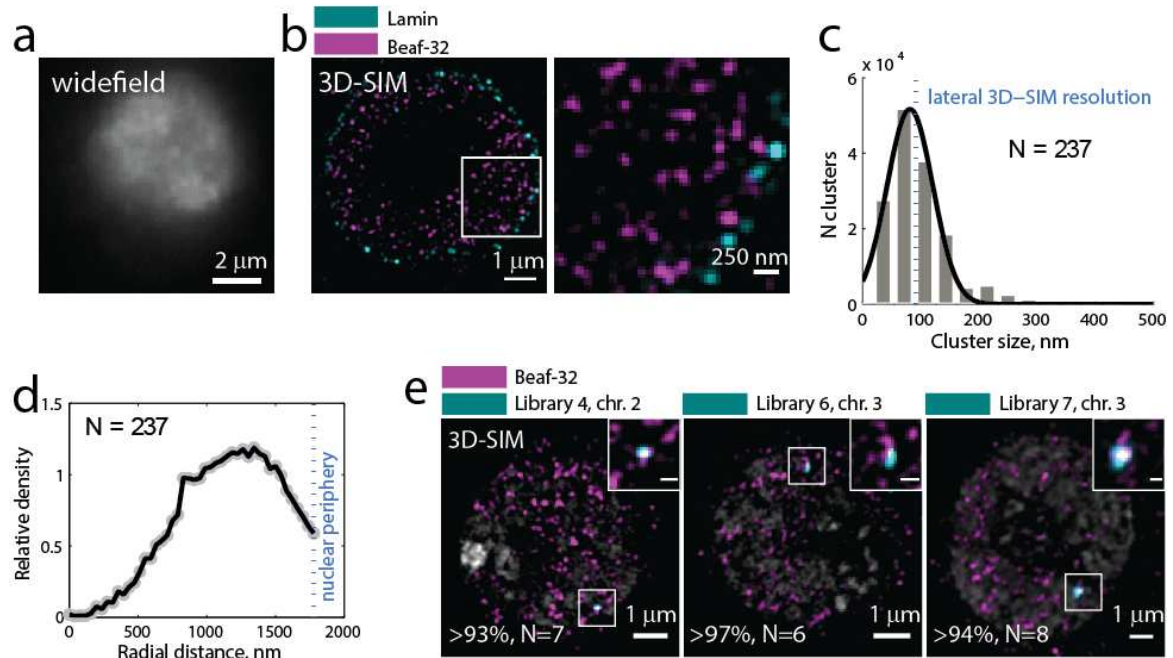
Figure 4.3 - Chromosomal organization of barriers



69 barriers between TDs spanning the entire right arm of chromosome 3 were labeled by oligoPAINT probes (red lines). The distribution in the number of probes per library is shown as a function of probe position along chromosome 3R. Color codes correspond to the color of chromatin at the TD barrier labeled. In average, libraries had 263 probes. **(b)** Number of TD barriers labeled for each chromatin color at the barrier (left) and the predominant color between barriers (right). **(c)** Distribution in the distance to next TD barrier as a function of barrier number. Barriers are numbered sequentially from centromere to telomere. Color code corresponds to the color of the predominant chromatin region between each TD barrier and the next barrier being labeled. The distribution of distances between barriers is homogeneous, with a mean of 320 kb. **(d)** Two characteristic 3D-SIM images of the 69 TD barriers labeled by oligoPAINT probes (green). DNA (DAPI) is labeled in blue. Typically, tens of clusters can be independently detected in each cell. **(e)** Distribution in the sizes of clusters detected per cell. Vertical dashed line represents the lateral resolution of 3D-SIM under these conditions (120 nm). Most clusters have a size equal or smaller than the lateral

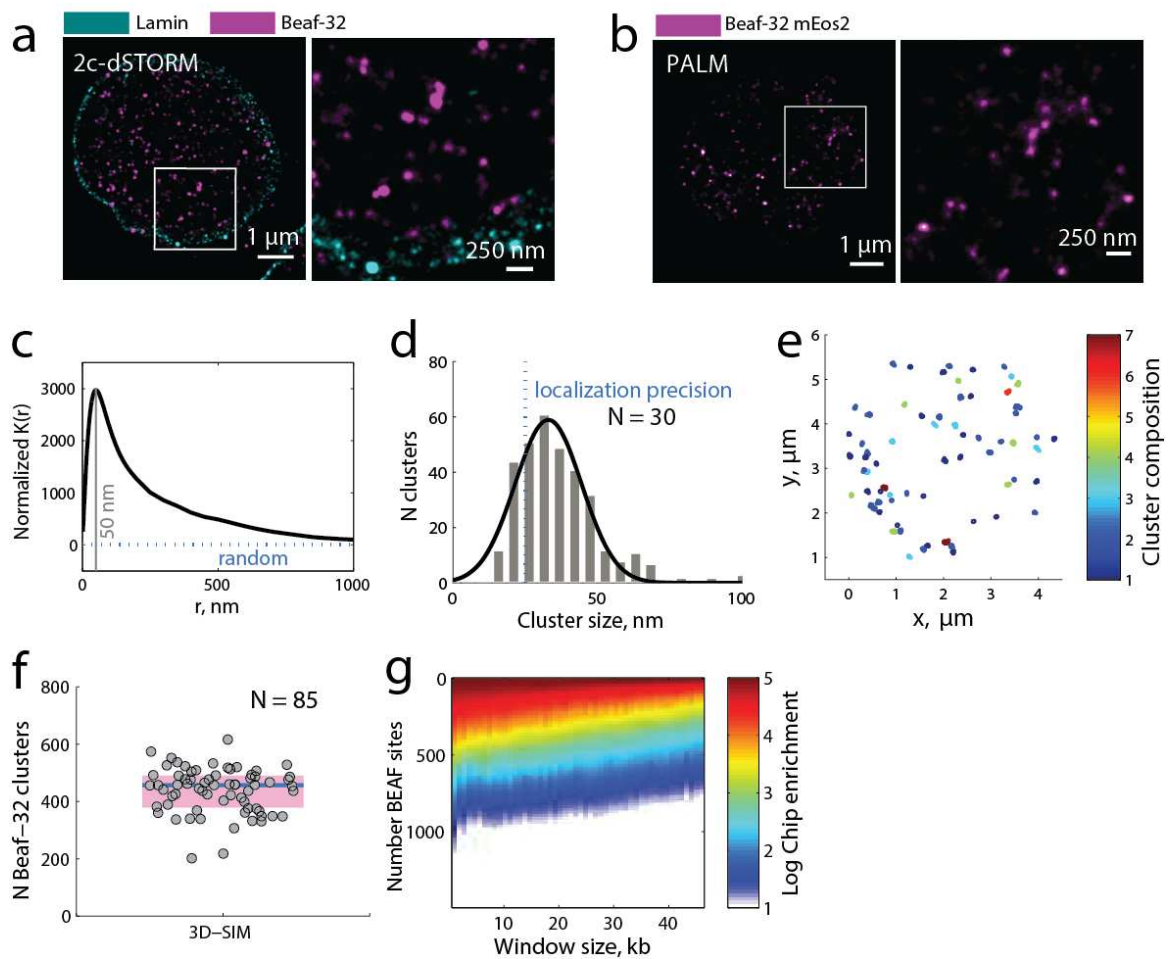
resolution. **(f)** Distribution of cluster sizes in the axial direction. Vertical dashed line indicates the axial 3D-SIM resolution (300 nm). **(g)** From the coordinates of each detected cluster, and the segmentation of the volume occupied by the nucleoid (see Experimental Procedures), the radial distribution of clusters was calculated from the center of the nucleus. **(h)** Boxplot representing the number of detected clusters per cell. The number of clusters in each cell is shown as grey circles, blue line represents the mean, and pink box the standard deviation. N represents the number of cells.

Figure 4.4 - Chromatin insulators and nuclear distribution of TD frontiers



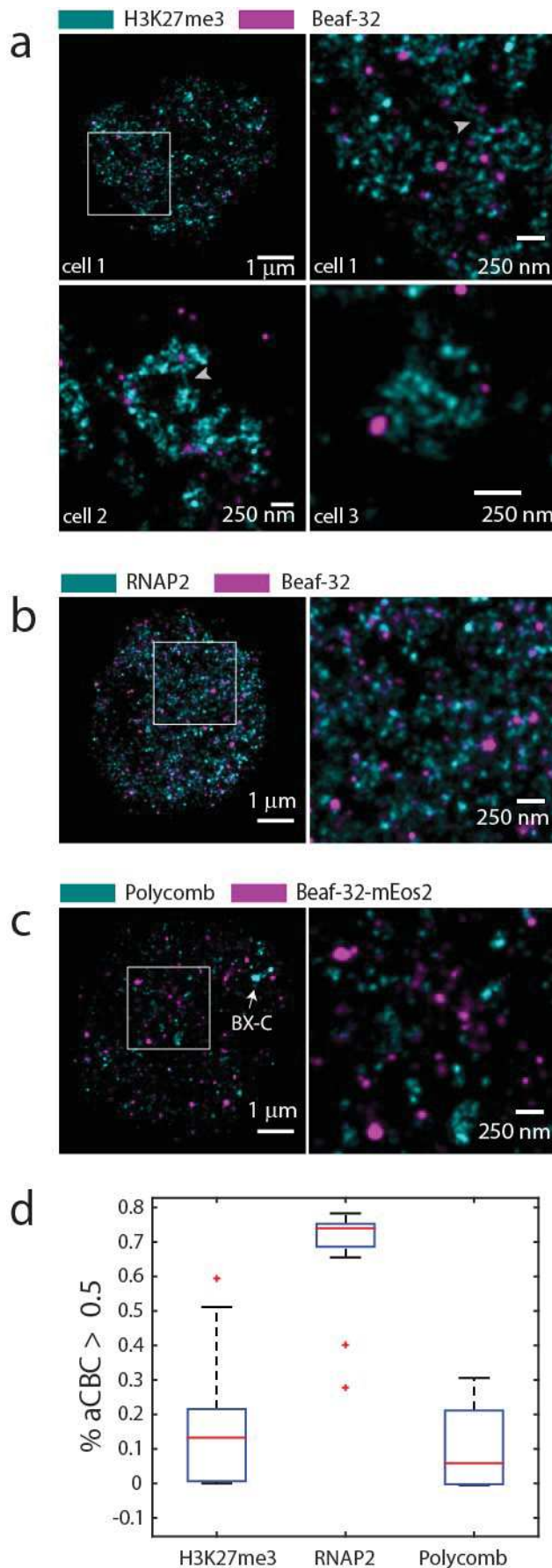
Typical epifluorescence image of antibody-labeled Beaf-32. **(b)** Characteristic 3D-SIM image under the same labeling conditions as in panel (a). Beaf-32 clusters are shown in pink, lamin in green. **(c)** Distribution of Beaf-32 cluster sizes in the lateral direction. Lateral resolution of 3D-SIM is shown as a vertical dashed line. N indicates number of cells. **(d)** Radial distribution of Beaf-32 clusters in the nucleus. **(e)** Typical three-color 3D-SIM images of immunolabeled Beaf-32 (magenta), single oligoPAINT probe libraries (cyan) and DNA (DAPI, grey).

Figure 4.5 - BEAF-32 distribution quantified by SMLM



Characteristic two-color dSTORM image Beaf-32 (magenta) and lamin (cyan). Whole cell is shown in left panel and magnified region in right panel. Beaf-32 can be clearly seen to form clusters distributed across the nucleus. Beaf-32 was labeled with primary antibody. **(b)** Typical PALM image of Beaf-32-mEos2. **(c)** Normalized Ripley's function as a function of radial distance from dSTORM data (black line) and for a random distribution of localizations (grey dashed line). The peak of the distribution provides an estimate of the typical cluster size. A similar distribution was obtained from PALM data (Figure 4.4h). **(d)** Beaf-32-mEos2 foci were clusterized and the number of detected clusters is plotted as a function of cluster size. Similar results were obtained for dSTORM imaging of Beaf-32 (Figure 4.4e). **(e)** Beaf-32 clustered localizations in a cell displayed with a color code indicating the estimated number of molecules per cluster. **(f)** Distribution in the number of Beaf-32 clusters obtained per cell from volumetric 3D-SIM datasets. N indicates number of cells. **(g)** Bioinformatics analysis of number of genomic loci occupied by Beaf-32 for different integration window sizes. Color-code indicates log of Chip signal enrichment.

Figure 4.6 - Epigenetic organization of Beaf-32 clusters

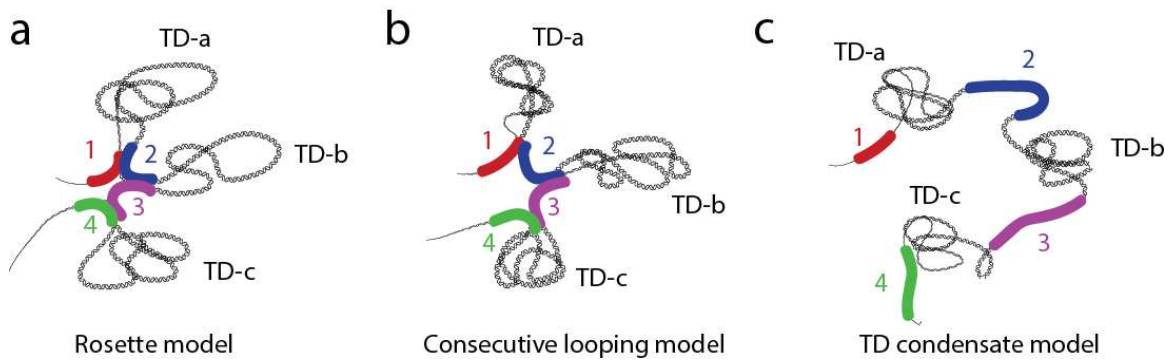


(a) – Typical two-color dSTORM image of Beaf-32 (magenta) and H3K27me3 (three cells are shown). Image on top right is magnification of image on top left. Beaf-32 rarely localizes with H3K27me3 marks. Image on bottom right is a zoom on a H3K27me3 domain with 2 foci of Beaf-32 at its periphery. Arrowheads point to regions of continuous single fiber stretches (FWHM 30 nm)

(b) – Characteristic two-color dSTORM image of Beaf-32 (magenta) and paused RNAPII, phosphorylated on CTD S5 (cyan), showing a large degree of colocalization.

(c) – Typical two-color dSTORM image of Polycomb (cyan) and Beaf-32 (magenta). Beaf-32 does not colocalize with Polycomb.

(d) – Quantification of the degree of colocalization between Beaf-32 and H3K27me3, RNAPII, and Polycomb using aCBC (see Section 3.3.2)

Figure 4.7 - Models for the higher-order structuration of TDs.

(a) – Rosette model proposes looping interactions between sequential and non-sequential TD barriers. **(b)** The consecutive looping model suggests that the barriers flanking each TD loop, but this looping does not extend to non-sequential barriers. **(c)** The TD condensate model proposes that the formation of TDs is due to the reinforced interaction between loci within the TD, or by domain borders acting as topological barriers preventing interactions of loci from neighboring TDs.

4.7 Experimental Procedures

3D-SIM, PALM and dSTORM

3D-SIM imaging was performed on an OMX V3 microscope (Applied Precision Inc) as previously described (Fiche et al., 2013). Reconstruction and alignment of 3D-SIM images was performed using softWoRx v 5.0 (Applied Precision Inc). PALM and 3D-PALM imaging was performed as described previously (Fiche et al., 2013; Marbouty et al., 2015). For 3D-PALM, a MicAO 3D-SR module (Imagine Optic™, France) was used. Two color dSTORM was performed using Cy3 and Atto647-labeled primary antibodies. Extensive chromatic aberration correction algorithms were used to ensure correction between channels was better than 10 nm. Refer to Supplemental Experimental Procedures for more details.

Cell culture, stress treatment and fixation

Drosophila S2 cells were obtained from the Drosophila Genomics Resource Center. They were grown in serum-supplemented (10%) Schneider's S2 medium at 25°C. Before stress treatment (heat shock or osmotic stress), S2 cells were allowed to adhere to a poly-l-lysine coverslip for 30 min in a covered 35-mm cell culture dish. To induce heat shock, cells were incubated at 37°C for 20min before fixation with 4% paraformaldehyde (PFA). For the osmotic stress, cells were treated with different indicated concentrations of NaCl (10mM, 50mM, 100mM, 250mM, 500mM, 1M from a 5M stock) as previously described (Schoborg et al., 2013). Controls were kept in conditioned media. Cells were stressed for 20 min and then immunostained. In brief, cells were fixed with 4% PFA for 10 min at RT, rinsed 3× with PBS, and either directly observed at the microscope (transfected cells) or immediately treated for immunostaining

Immunostaining

Cells were permeabilized with 0.5% Triton X-100 for 10 min, and blocked with 5% of bovine serum albumin (BSA) for 15 min at RT. For SIM experiments, primary antibodies (Emberly et al., 2008; CP190 and Beaf-32 made from rabbit

by Eurogentec) were diluted to final concentration of 4 μ g/ml in 1% BSA, and coverslips were incubated for 1h at RT in a humidified chamber followed by a 3 \times wash with PBS for 10 min each. Secondary antibodies (anti-mouse-A488 #A21202, anti-rabbit-A568 #A10042, anti-rabbit-A488 #A21206, anti-rabbit-Cy5 #A10523, anti-mouse-A568 #A11031, LifeTechnologies, Cstock at 2mg/ml) were then diluted to final concentration of 4 μ g/ml for 3D-SIM in 1% BSA and incubated for 1h at RT, and coverslips were washed as described. 0.5 μ g/ml DAPI was added to counterstain DNA, rinsed 2 \times with PBS, and mounted in Vectashield. For dSTORM only primary antibodies (H3K27me3/pAb-195-050/Diagenode, Anti-RNA polymerase II CTD repeat YSPTSPS phosphoS5/#ab5131/Abcam, Polycomb/generous gift from Giacomo Cavalli lab) were used at a final concentration of 7 μ g/ml diluted in 1% BSA and incubated overnight at 4 $^{\circ}$ C then washed 3 \times with large volumes of PBS (50 ml each). Fiducial markers diluted 1/4000 (Tetraspeck, #10195142, FisherScientific) were incubated with the samples for 5min in PBS. The coverslips were mounted on slides with 100 μ l wells (#2410, Glaswarenfabrik Karl Hecht GmbH & Co KG) in dSTORM buffer composed of PBS, glucose oxidase (G7141-50KU, Sigma) at 2.5 mg/ml, catalase at 0.2 mg/ml (#C3155-50MG, Sigma), 10% glucose and 50 mM of β -mercaptoethylamine (MEA, #M9768-5G, Sigma) are dissolved in PBS, and sealed with duplicating silicone (Twinsil, Rotec).

S2 cells transfection with BEAF-32-mEos2

The mEOS2-Beaf-32 sequence was synthesized by Clontech before being cloned in the plasmid pMT/V5-His-TOPO (DES TOPO TA Expression kit, LifeTechnologies) and used for the following transfection protocol. Transfections were performed in S2 cells that were plated at 2 millions of cells per well in a 6 wells plate containing 2 ml of Schneider's medium in each well. Cells were incubated 2-3h at 25 $^{\circ}$ C and transfected with Effectene reagent (Qiagen) in a mix containing 100 μ l EC buffer, 0.4 μ g pMT/V5-His-TOPO mEOS2-Beaf-32, 3.2 μ l enhancer, 20 μ l Effectene. After 24h, copper sulfate CuSO₄ (250 μ M) was added to activate the Drosophila metallothionein (MT) promoter for metal-inducible expression of our Beaf-32 gene of interest. The day after (i.e. 48h after the transfection), cells were harvested.

Design of oligoPAINT libraries

OligoPAINT libraries were constructed using a protocol adapted from Beliveau et al. (Beliveau et al., 2015).

Libraries 1-7, Chr3R-69TD, and BX-C were constructed from the oligoPAINT public database (<http://genetics.med.harvard.edu/oligopaints>). All libraries consisted of 42mer sequences discovered by OligoArray2.1 run with the following settings: -n 30 -l 42 -L 42 -D 1000 -t 85 -T99 -s 70 -x 70 -p 35 -P 80 -m 'GGGG;CCCC;TTTTT;AAAAA' -g 44. Oligonucleotide for libraries 1-7 and BX-C were ordered from CustomArray (Bothell, WA). The procedure used to synthesize oligoPAINT probes is described below. Chr3R-69 oligonucleotides were purchased from MYcroarray (Ann Arbor, MI). OligoPAINT probes for this library were synthesized using the same procedure as for the other libraries except for the initial emulsion PCR step. Secondary, fluorescently-labeled oligonucleotides were synthesized by Integrated DNA Technologies (IDT; Coralville, IA for Alexa488) and by Eurogentec (Angers, France for Cy3b). Please see Supplementary Table 1 for a list of oligoPAINT probe sets used for libraries 1-7. Sequences for secondary oligonucleotides and PCR primers are described below (Supplementary Tables 2-4).

Table 1: OligoPAINT probe sets for libraries 1-7

Chr	Lib	Genomic coordinates		Number of oligos	Specific primer pairs	
Chr2L	1	9990000	10010000	267	BB287-FWD	BB288-REV
Chr2L	2	10180000	10210000	405	BB293-FWD	BB294-REV
Chr2L	3	10420000	10540000	1615	BB295-FWD	BB296-REV
Chr2L	4	10710000	10750000	516	BB84-FWD	BB83-REV
Chr3R	5	12260000	12330000	944	BB291-FWD	BB292-REV

Chr3R	6	12450000	12480000	405	BB300-FWD	BB301-REV
Chr3R	7	12840000	12960000	1541	BB302-FWD	BB303-REV

PCR primers and secondary oligos

Fluorophore-labelled PCR primers, 5'-phosphorylated PCR primers used in the lambda exonuclease protocol and DNA secondary oligos were purchased from IDT and purified by IDT using high-performance liquid chromatography. Unlabelled, unphosphorylated primers were also purchased from IDT and purified by IDT using standard desalting.

Please see Supplementary Table below for a list of PCR primer pairs and a list of secondary oligos used.

Table 2: Unlabelled PCR primers

Name	Sequence	Lib	Chr
BB287-FWD	/5Phos/CGCTCGGTCTCCGTTTCGCTCTC	1	2L
Sec1-BB288-REV	CACCGACGTCGCATAGAACGGAAGAGCGTGTGGGGCTAGGTACAGGGTTCAGC	1	2L
BB293-FWD	/5Phos/CCGAGTCTAGCGTCTCCTCTG	2	2L
Sec1-BB294-REV	CACCGACGTCGCATAGAACGGAAGAGCGTGTGAACAGAGCCAGCCTCTACCTG	2	2L
Sec5-BB294-REV	TAGCGCAGGAGGTCCACGACGTGCAAGGGTGTAACAGAGCCAGCCTCTACCTG	2	2L
BB295-FWD	/5Phos/GCGTTAGGGTGCTTACGTCTG	3	2L
Sec1-BB296-REV	CACCGACGTCGCATAGAACGGAAGAGCGTGTGCACCTCCGTCTCTCACCTCTC	3	2L
Sec5-BB296-REV	TAGCGCAGGAGGTCCACGACGTGCAAGGGTGTCACCTCCGTCTCTCACCTCTC	3	2L
BB84-FWD	/5Phos/GATACGTTGGGAGGCAATGAG	4	2L

Sec1-BB83-REV	CACCGACGTCGCATAGAACGGAAGAGCGTGTGATCCTAACAAATCCCGCTGAGG	4	2L
Sec5-BB83-REV	TAGCGCAGGAGGTCCACGACGTGCAAGGGTGTATCCTAACAAATCCCGCTGAGG	4	2L
BB291-FWD	/5Phos/CAGGTCGAGCCCTGTAGTACG	5	3R
Sec1-BB292-REV	CACCGACGTCGCATAGAACGGAAGAGCGTGTGCTAGGAGACAGCCTCGGACAC	5	3R
BB300-FWD	/5Phos/CCAGTGCTCGTGTGAGAAGTC	6	3R
Sec1-BB301-REV	CACCGACGTCGCATAGAACGGAAGAGCGTGTGCTGCAGAGAAGAGGCAGGTTTC	6	3R
Sec5-BB301-REV	TAGCGCAGGAGGTCCACGACGTGCAAGGGTGTCTGCAGAGAAGAGGCAGGTTTC	6	3R
BB302-FWD	/5Phos/CGCACTGAACCAGACTACCTG	7	3R
Sec1-BB303-REV	CACCGACGTCGCATAGAACGGAAGAGCGTGTGGAGAGGCGAGGACACCTACAG	7	3R
Sec5-BB303-REV	TAGCGCAGGAGGTCCACGACGTGCAAGGGTGTGAGAGGCGAGGACACCTACAG	7	3R

Table 3: Labelled PCR primers

Name	Sequence
BB506-A647 (Sec1)	/5Alex647N/CACCGACGTCGCATAGAACGG
BB506-A488 (Sec1)	/5Alex488N/CACCGACGTCGCATAGAACGG
BB510-Cy3B (Sec5)	/5Cy3B/TAGCGCAGGAGGTCCACGAC

Table 4: Secondary labelled oligonucleotides

Name	Sequence
Sec1-A647-X2(Sec1)	/5Alex647N/CACACGCTCTCCGTTCTATGCGACGTCGGTGagatggtt/3AlexF647N/

Sec1-A488-X2(Sec1)	/5Alex488N/CACACGCTCTCCGTTCTATGCGACGTCGGTGagatgttt/3AlexF488N/
Sec5-Cy3B-X2(Sec5)	/5Cy3B/ACACCCTTGACGTCGTGGACCTCCTGCGCTAagatgttt/3Cy3B/

Emulsion PCR amplification of oligonucleotide libraries

Raw, multiplexed libraries purchased from CustomArray were amplified using universal primers using emulsion PCR to generate template to use in subsequent PCR reactions. Hundred ml of aqueous PCR master mix was gradually mixed into a 600-ml of 95.95% mineral oil (Sigma M5904):4% ABIL EM90 (Degussa):0.05% Triton-X-100 (Sigma T8787) oil phase (v/v/v) at 1,000 r.p.m. for 10 min at 4C. For the emulsion PCR, we used the following PCR primers:

- GACTGGTACTCGCGTGACTIONT as forward primer
- GTAGGGACACCTCTGGACTGG as reverse primer.

Reactions were amplified with the following cycle: 95 C for 2min; 30 cycles of 95 C for 15 s, 60 C for 15 s and 72 C for 5min, with a final extension step at 72 C for 5min. After cycling, the DNA was recovered by a series of organic extractions: first using diethyl ether (Sigma 296082), then using ethyl acetate (Sigma 494518); then once again using diethyl ether. These extractions were followed by a purification of DNA samples with Qiagen columns to remove Taq polymerase. For stepwise emulsion, PCR and emulsionbreaking protocols, please see the Oligopaints website (<http://genetics.med.harvard.edu/oligopaints>).

Oligopaint probe synthesis

Oligopaints probes containing secondary oligo binding sites were synthesized using the lambda exonuclease method (Beliveau et al., 2015). The secondary oligo-binding sites were added to Oligopaint probe sets through the use of the following 'touch-up' PCR cycle: 95 C for 5min; 3 cycles of 95 C for 30 s, 60 C for 45 s and 72 C for 30 s; 20 cycles of 95 C for 30 s, 68 C for 1min and 72 C for 30 s, with a final extension step at 72 C for 5min. The template generated via 'touch-up' PCR was further amplified with the following cycle: 95 C for 5min; 31 cycles of 95 C for 30 s, 60 C for 30 s and 72 C for 15 s, with a final extension

step at 72 C for 5min. For stepwise probe synthesis protocols, please see the Oligopaint website (<http://genetics.med.harvard.edu/oligopaints>).

‘One-day’ probe synthesis using lambda exonuclease

Oligopaint probe sets were amplified using the ‘two-PCR’ method described above, but with the unlabeled primer being phosphorylated on its 5’end. The PCR reaction was then collected, concentrated using spin columns (Zymo D4031) and digested with lambda exonuclease (New England Biolabs M0262). Five units of lambda exonuclease were added per every 100 ml of unconcentrated PCR reaction (for example, use 50 units if the labelling PCR had a volume of 1 ml before concentration by the spin column) and the reaction was incubated at 37 C for 30 min in a thermocycler and then stopped by incubation at 75 C for 10 min. Finally, the digestion products were concentrated using ethanol precipitation and quantified using Nanodrop. For a detailed protocol, please see the OligoPAINT website (<http://genetics.med.harvard.edu/oligopaints>).

Preparation of sample slides for FISH and 2 color-FISH

To prepare sample slides containing fixed S2 cells for FISH, S2 cells were allowed to adhere to a poly-l-lysine coverslip for 1h in a covered 35-mm cell culture dish at 25C. Slides were then washed in PBS, fixed 4% paraformaldehyde (PFA) for 10 min, rinsed 3 times for 5 min in PBS, permeabilized 10min with 0.5% Triton, rinsed in PBS, incubated with 0.1M HCl for 10min, washed in 3 times for 1 min with 2X saline-sodium citrate - 0.1% Tween-20 (2XSSCT) and incubated in 2XSSCT/50% formamide (v/v) for at least 30min. Then, probes were prepared by mixing 20µl of hybridization buffer FHB (50% Formamide, 10% Dextranulfat, 2X SSC, Salmon Sperm DNA 0.5 mg/ml), 0.8 µL of RNase A, 30 pmol of primary probe and 30pmol of secondary oligo. 12 µl of this mix were added to a slide before adding and sealing with rubber cement the coverslips with cells onto the slide. Probes and cells are finally co-denatured 3 min at 78°C before hybridization overnight at 37°C. The next day, the slides were washed for 3 times for 5 min in 2X SSC at 37°C, then for 3 times for 5 min in 0.1X SSC at 45°C. Finally, they were stained with 0.5µg/ml of DAPI for 10min, washed with PBS, mounted in Vectashield and sealed with nail polish. For a more detailed protocol, see (Bantignies and Cavalli, 2014).

Two-color STORM and PALM acquisition

The microscope setup was described in Section 3.6.1.

Analysis of two-color STORM and PALM datasets

Unless stated otherwise, all homemade software and routines were developed in Matlab. Single-molecule localizations were obtained by using Multiple Target Tracing (MTT) (Serge et al., 2008). Localization coordinates were further processed using SMLM_2C, custom software written in Matlab. Fluorescent beads were used to correct for drift and chromatic aberrations. Lateral drift was corrected with 5 ± 3 nm precision as previously described (Fiche et al., 2013). Chromatic aberration correction was performed as described in (Churchman and Spudich, 2012). Samples with abnormal drift or lesser precision of drift or chromatic aberration correction were discarded. Clusterization of localizations was performed as described in Cattoni et al. (Cattoni et al., 2013). Colocalization of single-molecule localizations was performed using a custom implementation of the Coordinate-based colocalization analysis (Malkusch et al., 2011) adapted for whole-cell automated analysis.

Size of BEAF-32 clusters in PALM/STORM experiments (Ripley Analysis)

To get an unbiased estimate of the size of BEAF-32 clusters in PALM/STORM experiments, we calculated for the localizations in each dataset the Ripley's K-function ($K(r)$, (Ripley, 1977)). $K(r)$ scales with the number of localizations found in the searching area πr^2 thus it is well suited to identify the characteristic r at which localizations accumulate (i.e. cluster radius). To properly account for the size of the sampling area and the size of the sample (i.e. number of localizations) Ripley's function was computed as described by Lagache et al. (Lagache et al., 2013). Due to the round shapes of the nuclei, to avoid strong border effects, only the localizations in rectangular ROIs at the center of the nuclei were subjected to the Ripley analysis. In order to identify statistical relevance of the distribution, positive deviations of $K(r)$ 0.05 and 0.95 quantiles were calculated and superimposed to the computed Ripley's functions. The clusters' radii found with Ripley analysis $R_{\text{Cluster}} = R_{\text{Max}}/1.3$ (NB this is how they define R cluster in the paper) is in good agreement with the radii found with our clusterization algorithm.

Clusterization in PALM/STORM

Clusterization of PALM/STORM localizations is obtained by an algorithm described in detail elsewhere (Cattoni et al., 2013). Briefly, the field of view was divided in virtual pixels of a size smaller than the physical pixels. The localizations are then plotted over the virtual pixels and used to generate a binarized image (virtual pixels containing at least one localization are set to 1 the others to 0). The different clusters are identified as groups of connecting virtual pixels containing at least 10 localizations.

3D Structured Illumination Microscopy (3D-SIM)

Instrumentation and imaging

Samples were prepared as described above and mounted on an OMX V3 microscope (Applied Precision Inc.) equipped with a 100X/1.4 oil PlanSApo objective (Olympus) and three emCCD cameras. 405 nm, 488 nm and 561 nm excitation lasers lines were used to excite DAPI, Alexa488 and Cy3, respectively. Each channel was acquired sequentially. A transmission image was also acquired to control for cell morphology. For each channel, a total of 1455 images made of 97 different Z-planes separated by 125 nm were acquired, in order to acquire a stack of 12 μm . Three different angles (60° , 0° and $+60^\circ$) as well as five phase steps were used to reconstruct 3D-SIM images using softWoRx v5.0 (Applied Precision Inc.). Final voxel size was 39.5 nm in the lateral (xy) and 125 nm in the axial (z) directions, respectively, for a final 3D stack volume of $\sim 40 \times 40 \times 12 \mu\text{m}$. Multicolor TetraSpeck beads (100 nm in diameter, Invitrogen) were used to measure x, y and z offsets, rotation about the z-axis and magnification differences between fluorescence channels. These corrections were applied to the reconstructed images. The same beads were used to validate the reconstruction process ensuring a final resolution of ~ 120 nm in xy and ~ 300 nm in z at 525 nm of emission wavelength. 3D-SIM raw and reconstructed images were analyzed with SIMCheck ImageJ Plug-in (University of Oxford, <http://www.micron.ox.ac.uk/software/SIMCheck.php>). Acquisition parameters were optimized to obtain excellent signal-to-noise ratio avoiding photobleaching between the different angular, phase, and axial acquisitions.

Analysis of 3D-SIM data

In 3D-SIM, foci were identified by first segmenting the DAPI signal of the nuclei (by manually selecting rectangular ROIs in the XY-plane and keeping all the Z-planes) and then calculating, for each channel separately, the maximum entropy threshold of the fluorescence intensities in the 3D ROIs. By using the intensity thresholds the 3D ROIs are finally binarized (voxels above threshold are set to 1 while the others to 0) and the different foci identified as groups of connected voxels.

3D nuclei segmentation in SIM

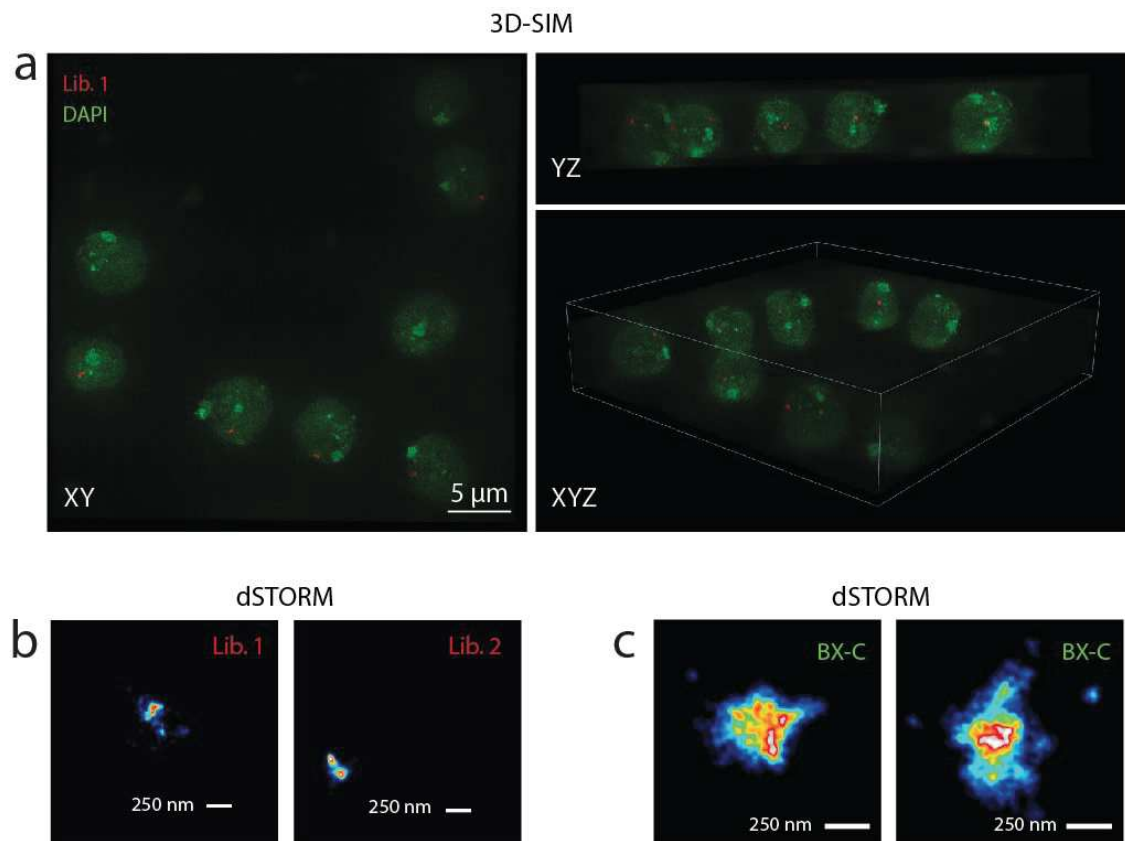
In order to identify nuclear shells, nuclei are first segmented (as discussed in the previous paragraph) and then a low-pass filter is applied to the DAPI intensities so that only the large-scale information (i.e. nuclear shape) is kept. For each plane of the 3D ROIs, an intensity threshold is computed as described by Snell et al. (Snell et al., 2011) in order to distinguish voxels inside or outside the nucleus. The average intensity threshold calculated from the threshold of the single planes is used to identify the complete nuclear shell.

Flow cytometry

Transfected or untransfected cells were harvested and centrifuged at 1000rpm for 5min at room temperature. Then, they were washed with PBS, centrifuged at 1000rpm for 5min at 4°C and finally fixed in cold 70% EtOH. After one night at 4°C, cells were washed 2 times with PBS (centrifugation at 850g for 5min at 4°C) before the addition of 1ml of PBS on each pellet. After 5min of incubation on ice for rehydration of the pellet, the cells were incubated 20min at 37°C with 50µg/ml of RNase A (12091-039, Invitrogen) and then incubated 20min on ice with 10µg/ml of propidium iodide (P3566, ThermoFisherScientific). Finally, cells were runned on Miltenyi MACSQuant flow cytometer (MRI-RIO platform, IGH).

4.8 Supplementary Figures

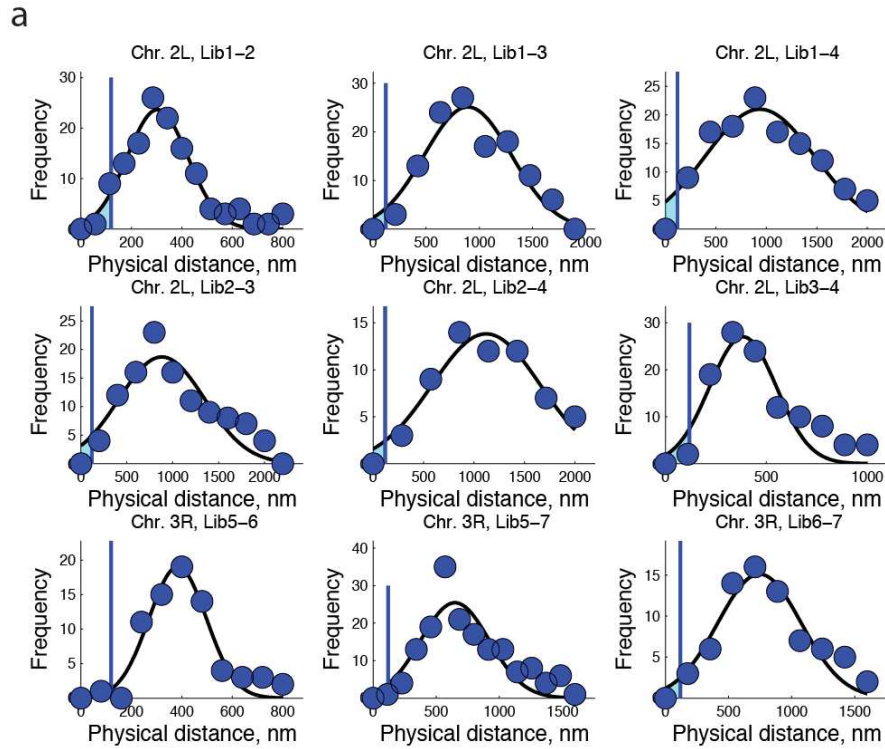
Figure S 4.1 - 3D-SIM and dSTORM imaging of TD barriers



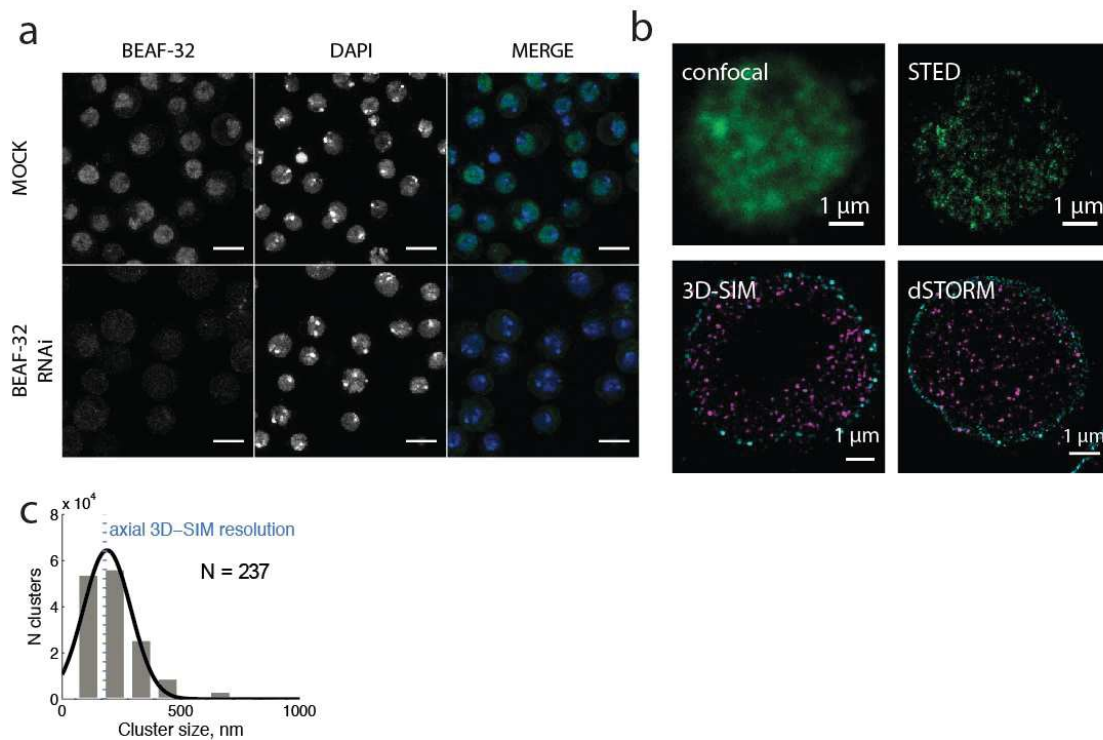
(a) Field of view of S2 cells imaged by 3D-SIM. Three different views are provided. Green represents DAPI, red represents library 1 labeled by oligoPAINT.

(b-c) dSTORM image of libraries 1, 2 and BX-C. TD barriers often appear as single foci with a lateral size of ~50-100 nm. In contrast, BX-C appears as a distributed structure spanning hundreds of nm in size.

Figure S 4.2 - Distance distributions between pairs of TD barriers



(a) Distribution of distances between libraries pairs of libraries (blue circles, see top of each panel). A Gaussian fit (black curve) was used to determine the mean and standard deviation (see Figures 2e and 2f). Cyan shaded surface represents the area under the curve from zero to the resolution of 3D-SIM (120 nm for green channel), and provides an estimate for the maximum degree of co-localization between libraries.

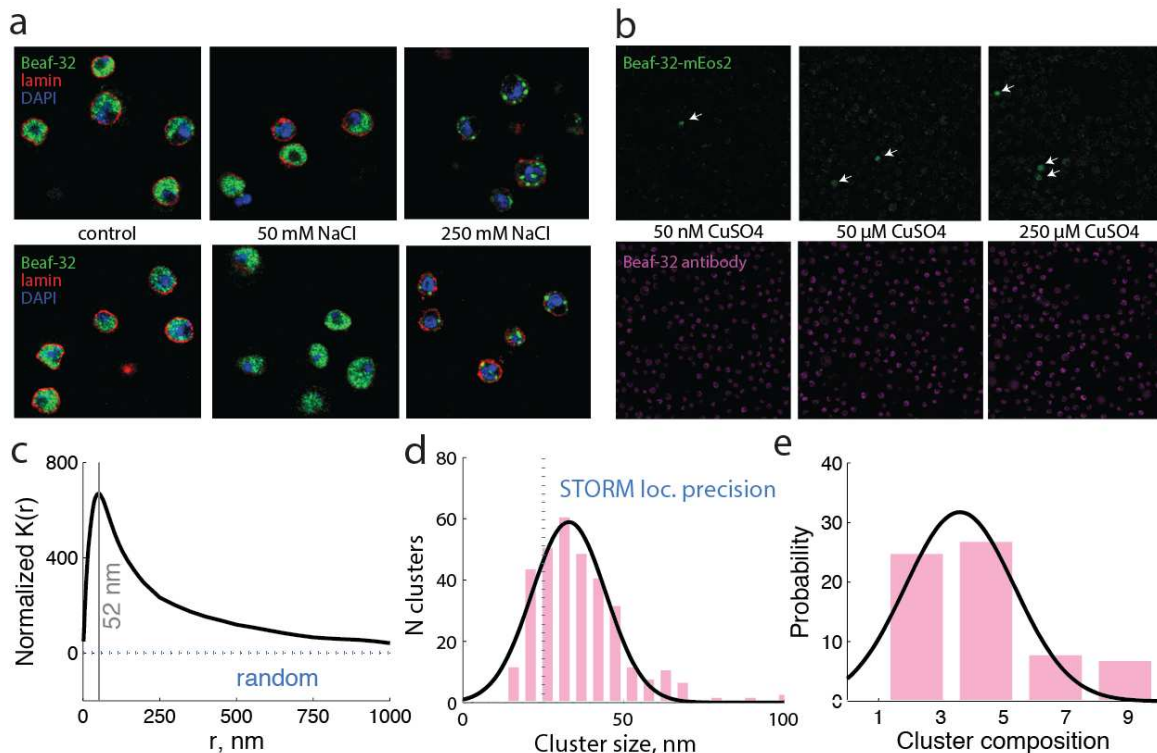
Figure S 4.3 - Beaf-32 antibody specificity and STED imaging of Beaf-32

(a) Control for Beaf-32 antibody specificity. Beaf-32 from a wild type culture of S2 cells is imaged by IF using conventional microscopy (top panel). Beaf-32 is depleted in an S2 culture by RNA interference (RNAi) and imaged using the same conditions (bottom panel). The nearly complete loss of fluorescence in the nucleus in cells in which Beaf-32 was depleted is evidence for the excellent specificity of the antibody. Note that the non-specific signal observed in the cytoplasm of RNAi-treated cells may be due to a very low degree of nonspecific binding of the secondary antibody (as compared to the nuclear signal in the mock sample) or reflect the autofluorescence of cytoplasmic components.

(b) Confocal and stimulated emission depletion (STED) microscopy of a typical S2 cell in which Beaf-32 was labeled by IF (green, top panel). As for SMLM and 3D-SIM, multiple small clusters can be revealed at super-resolution, but could not be visualized using diffraction-limited microscopies. For comparison, 3D-SIM and dSTORM imaging of Beaf-32 under the same conditions are shown in the bottom panels (lamina: cyan, Beaf-32: magenta).

(c) Distribution of Beaf-32 cluster sizes in the axial direction. Axial resolutions of 3D-SIM is shown as a vertical dashed line. N indicates number of cells.

Figure S 4.4 - Influence of osmotic shock on Beaf-32 nuclear distribution, expression levels of Beaf-32-mEos2 transfected cells, and STORM/PALM analysis of Beaf-32



(a) Three color immunofluorescence confocal image of a field of view of S2 cells labeled with lamin (red), DAPI (blue) and using a primary+secondary antibody for Beaf-32 (green). In control cells (first column) Beaf-32 distributes roughly homogeneously throughout the nucleus (although higher intensity regions can be often seen). At 50 mM salt, the distribution of Beaf-32 seems unchanged. However, at high osmotic shocks (250 mM monovalent salt), Beaf-32 can be seen to cluster in a small number of sites within the nucleus and predominantly at the cell periphery. These results are consistent with Schoborg et al. (Schoborg et al., 2013).

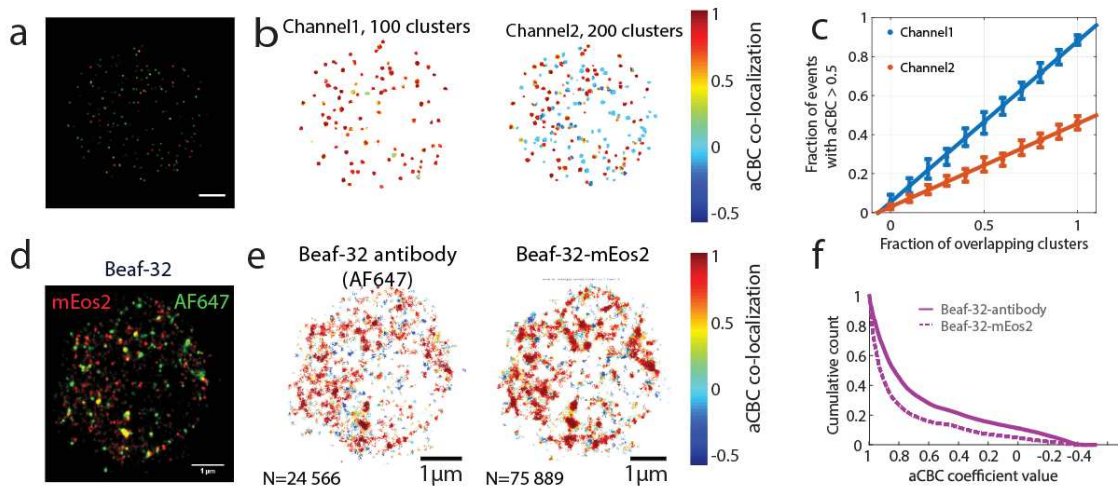
(b) Two-color immunofluorescence confocal images of S2 cells transfected with Beaf-32-mEos2. A field of view is shown for each induction condition. Top row represents Beaf-32-mEos2. A relatively homogeneous level of fluorescence can be observed in the population of cells, apart from a few cells with higher expression (see arrows). Cells with higher levels of signal than the average were discarded for PALM imaging. Bottom row: transfected cells imaged by immunofluorescence (primary Beaf-32 antibody conjugated to Cy5). A very homogeneous fluorescence signal is observed for different cells in this channel, consistent with the induction levels of Beaf-32 being very similar to endogenous levels of Beaf-32.

(c) Normalized Ripley's function as a function of radial distance from dSTORM data (black line) and for a random distribution of localizations (grey dashed line). The peak of the distribution provides an estimate of the typical cluster size. A similar distribution was obtained from PALM data (Figure 4.4h).

(d) Beaf-32 foci from dSTORM images were clusterized and the number of detected clusters is plotted as a function of cluster size. Similar results were obtained for PALM imaging of Beaf-32-mEos2 (Figure 4.4i).

(e) Beaf-32-mEos2 foci were clusterized and the distribution in the number of detected clusters is plotted. A typical cell is displayed in Figure 4i.

Figure S 4.5 - Co-localization analysis: simulations and positive control



(a-b) To evaluate the effect of the input parameter values on the output of the aCBC analysis, a simple case was simulated. A random distribution of Gaussian SMLM clusters within a circle with radius equal to $3 \mu\text{m}$ (the size of clusters is $\sigma=20\pm 5 \text{ nm}$, and mean number of events per cluster = 50). In the first channel (red), the centers of 100 clusters completely overlap with the centers of 100 clusters in the second channel (green), which contains a total of 200 clusters. Thus, in this simulation, all red clusters should co-localize with a green cluster, but only half of the green clusters localize with a red cluster. A partial overlap is seen when reconstructions using probability density distributions are shown in different colors (panel a). The dataset was analyzed with aCBC and the colocalization coefficient maps of the individual localizations are shown in panel b. In this representation, it is clear that clusters in channel 1 (red) display a very high degree of co-localization whereas only a fraction of clusters in channel 2 (green) display a large degree of co-localization. **(c)** Next, the correlation coefficient from aCBC analysis was measured as a function of the simulated colocalization. Clusters in 2-colors were generated as in panels a-b, and the percentage of overlapping clusters from channel 1 was varied between 0% and 100%. The aCBC coefficients were calculated, and to compare the different colocalization situations the fraction of localizations with a high colocalization coefficient was extracted from the aCBC coefficient histograms. The results are summarized in panel c, where each data point is the mean percentage of events with $\text{aCBC} > 0.5$ from 30 randomly generated datasets at a given level of colocalization. The error bars indicate the standard deviation of the mean values obtained from several simulations. A strong linear dependence is observed between the

true colocalization (X axis) and the fraction of events with strong positive correlation (Y axis), for both channel 1 and channel 2. This observation indicates that the true colocalization percentage can be inferred by the aCBC analysis in a straightforward manner. Furthermore, the method demonstrates a high level of reproducibility, with average standard deviation of the measurements of 0.04 ± 0.01 for channel 1, and 0.03 ± 0.008 for channel 2. **(d)** To validate our co-localization acquisition and analysis approach, we performed a positive control in which Beaf-32 was imaged simultaneously by two different methods: tagging with a photoactivatable probe (mEos2) and immunolabeled using primary Beaf-32 antibodies. A typical two-color probability density image is shown. **(e)** To quantitatively estimate the degree of co-localization, we applied aCBC analysis. We observe that most clusters of Beaf-32 antibody (left panel) are localized with a Beaf-32-mEos2 cluster, and vice versa (right panel). **(f)** To further quantify the degree of co-localization, we plotted the cumulative count as a function of aCBC coefficient. Clearly, this distribution shows that most localizations display a large degree of co-localization in both channels.

APPENDIX

ABBREVIATIONS

(a)CBC	(automated) Coordinate-based colocalization analysis
(d)CTCF	(drosophila) CCCT- binding factor, a zinc finger insulator protein
(d)STORM	(direct) Stochastic optical reconstruction microscopy
(m)ESC	(mouse) Embryonic stem cells
3C	Chromosome conformation capture
4C	Chromosome conformation capture on chip
5C	Chromosome conformation capture carbon copy
BEAF-32	Boundary element associated factor
CHIP-seq	Chromatin immuno-precipitation coupled to high-throughput sequencing
CP190	Centrosomal protein 190 KDa
DAPI	4',6-diamidino-2-phenylindole - fluorescent DNA intercalating dye
DHS	DNaseI hypersensitive sites
FOV	Imaging field of view
H3K27me3	Histone 3 trimethylated on Lysine 24, chromatin repressive mark
Hi-C	Chromosome conformation capture coupled to high-throughput sequencing

HOX	Homeobox gene locus, involved in the regulation of developmental programs in mammals
IBP	Insulator-binding protein
IF	Immunofluorescence
IgG	Immunoglobulin of class G
LRI	Long-range interaction
MHC	Major Histocompatibility complex
PALM	Photoactivated localization microscopy
PBS	Phosphate buffered saline
PcG	Polycomb group proteins
POL2	RNA polymerase 2
POL2pS5	RNA polymerase 2 phosphorylated on Ser5 of the C-terminal domain: initiating (paused) Polymerase on the promoters
PTM	Post-translational modifications
RNAP2	RNA polymerase 2
ROI	Region of interest in an image
SMLM	Single-molecule localization microscopy, includes PALM, Dstorm, STORM, FPALM
SNR	Signal to noise ratio
SRM	Super-resolution microscopy
T(A)D	Topologically associating domain / topological domain
Xa	Active X chromosome in females
Xi	Inactive X chromosome
Xic	X chromosome inactivation center

FIGURES INDEX

Figure 1.1 - Eukaryotic chromatin at various scales.....	26
Figure 1.2 - Topological domains seen by Hi-C	35
Figure 2.1 - Resolution in conventional fluorescence microscopy	47
Figure 2.2 - Super-resolution microscopy techniques	54
Figure 2.3 - Chromatin labeling strategies for single-molecule localization microscopy	64
Figure 3.1 - Control of antibody specificity by RNAi	72
Figure 3.2 - Sequential 2-color SMLM imaging procedure	81
Figure 3.3 - Determination of aCBC parameters.....	92
Figure 3.4 - Evaluation of aCBC performance	95
Figure 3.5 - Quality control of SMLM images using 2-color labeling and colocalization analysis.....	101
Figure 3.6 - Microscope setup for multicolour SMLM imaging	107
Figure 4.1 - Imaging single TD barriers at the single-cell level	134
Figure 4.2 - Local organization of barriers at super-resolution.....	136
Figure 4.3 - Chromosomal organization of barriers.....	138
Figure 4.4 - Chromatin insulators and nuclear distribution of TD frontiers.....	140
Figure 4.5 - BEAF-32 distribution quantified by SMLM	141
Figure 4.6 - Epigenetic organization of Beaf-32 clusters	142
Figure 4.7 - Models for the higher-order structuration of TDs.	143

FIGURES INDEX - SUPPLEMENTARY DATA CHAPTER 4

Figure S 4.1 - 3D-SIM and dSTORM imaging of TD barriers	155
Figure S 4.2 - Distance distributions between pairs of TD barriers	156
Figure S 4.3 - Beaf-32 antibody specificity and STED imaging of Beaf-32.....	157
Figure S 4.4 - Influence of osmotic shock on Beaf-32 nuclear distribution, expression levels of Beaf-32-mEos2 transfected cells, and STORM/PALM analysis of Beaf-32.....	158
Figure S 4.5 - Co-localization analysis: simulations and positive control.....	160

BIBLIOGRAPHY

Abbe, E. (1873). Beiträge zur Theorie des Mikroskops und der mikroskopischen Wahrnehmung.

Albiez, H., Cremer, M., Tiberi, C., Vecchio, L., Schermelleh, L., Dittrich, S., Küpper, K., Joffe, B., Thormeyer, T., von Hase, J., et al. (2006). Chromatin domains and the interchromatin compartment form structurally defined and functionally interacting nuclear networks. *Chromosome Res. Int. J. Mol. Supramol. Evol. Asp. Chromosome Biol.* *14*, 707–733.

Allen, J.R., Ross, S.T., and Davidson, M.W. (2014). Structured Illumination Microscopy for Superresolution. *ChemPhysChem* *15*, 566–576.

Annibale, P., Vanni, S., Scarselli, M., Rothlisberger, U., and Radenovic, A. (2011a). Quantitative Photo Activated Localization Microscopy: Unraveling the Effects of Photoblinking. *PLoS ONE* *6*, e22678.

Annibale, P., Vanni, S., Scarselli, M., Rothlisberger, U., and Radenovic, A. (2011b). Identification of clustering artifacts in photoactivated localization microscopy. *Nat. Methods* *8*, 527–528.

Bantignies, F., and Cavalli, G. (2014). Topological organization of Drosophila Hox genes using DNA fluorescent in situ hybridization. *Methods Mol. Biol. Clifton NJ* *1196*, 103–120.

Bantignies, F., Roure, V., Comet, I., Leblanc, B., Schuettengruber, B., Bonnet, J., Tixier, V., Mas, A., and Cavalli, G. (2011). Polycomb-dependent regulatory contacts between distant Hox loci in Drosophila. *Cell* *144*, 214–226.

Bartkuhn, M., Straub, T., Herold, M., Herrmann, M., Rathke, C., Saumweber, H., Gilfillan, G.D., Becker, P.B., and Renkawitz, R. (2009). Active promoters and insulators are marked by the centrosomal protein 190. *EMBO J.* *28*, 877–888.

Bates, M., Huang, B., Dempsey, G.T., and Zhuang, X. (2007a). Multicolor Super-Resolution Imaging with Photo-Switchable Fluorescent Probes. *Science* *317*, 1749–1753.

Bates, M., Huang, B., Dempsey, G.T., and Zhuang, X. (2007b). Multicolor Super-Resolution Imaging with Photo-Switchable Fluorescent Probes. *Science* *317*, 1749–1753.

Beliveau, B.J., Joyce, E.F., Apostolopoulos, N., Yilmaz, F., Fonseka, C.Y., McCole, R.B., Chang, Y., Li, J.B., Senaratne, T.N., Williams, B.R., et al. (2012). Versatile design and synthesis platform for visualizing genomes with Oligopaint FISH probes. *Proc. Natl. Acad. Sci. U. S. A.* *109*, 21301–21306.

Beliveau, B.J., Boettiger, A.N., Avendaño, M.S., Jungmann, R., McCole, R.B., Joyce, E.F., Kim-Kiselak, C., Bantignies, F., Fonseka, C.Y., Erceg, J., et al.

(2015). Single-molecule super-resolution imaging of chromosomes and in situ haplotype visualization using Oligopaint FISH probes. *Nat. Commun.* *6*, 7147.

Benke, A., and Manley, S. (2012). Live-Cell dSTORM of Cellular DNA Based on Direct DNA Labeling. *ChemBioChem* *13*, 298–301.

Bennett, B.T., Bewersdorf, J., and Knight, K.L. (2009). Immunofluorescence imaging of DNA damage response proteins: Optimizing protocols for super-resolution microscopy. *Methods* *48*, 63–71.

Berezney, R., Malyavantham, K.S., Pliss, A., Bhattacharya, S., and Acharya, R. (2005). Spatio-temporal dynamics of genomic organization and function in the mammalian cell nucleus. *Adv. Enzyme Regul.* *45*, 17–26.

Betzig, E., Patterson, G.H., Sougrat, R., Lindwasser, O.W., Olenych, S., Bonifacino, J.S., Davidson, M.W., Lippincott-Schwartz, J., and Hess, H.F. (2006). Imaging Intracellular Fluorescent Proteins at Nanometer Resolution. *Science* *313*, 1642–1645.

Bickmore, W.A. (2013). The Spatial Organization of the Human Genome. *Annu. Rev. Genomics Hum. Genet.* *14*, 67–84.

Bickmore, W.A., and van Steensel, B. (2013). Genome Architecture: Domain Organization of Interphase Chromosomes. *Cell* *152*, 1270–1284.

Bohn, M., Diesinger, P., Kaufmann, R., Weiland, Y., Müller, P., Gunkel, M., von Ketteler, A., Lemmer, P., Hausmann, M., Heermann, D.W., et al. (2010). Localization Microscopy Reveals Expression-Dependent Parameters of Chromatin Nanostructure. *Biophys. J.* *99*, 1358–1367.

Bolte, S., and Cordelières, F.P. (2006). A guided tour into subcellular colocalization analysis in light microscopy. *J. Microsc.* *224*, 213–232.

Boyle, S., Gilchrist, S., Bridger, J.M., Mahy, N.L., Ellis, J.A., and Bickmore, W.A. (2001). The spatial organization of human chromosomes within the nuclei of normal and emerin-mutant cells. *Hum. Mol. Genet.* *10*, 211–219.

Bückers, J., Wildanger, D., Vicidomini, G., Kastrup, L., and Hell, S.W. (2011). Simultaneous multi-lifetime multi-color STED imaging for colocalization analyses. *Opt. Express* *19*, 3130–3143.

Bushey, A.M., Ramos, E., and Corces, V.G. (2009). Three subclasses of a *Drosophila* insulator show distinct and cell type-specific genomic distributions. *Genes Dev.* *23*, 1338–1350.

Caddle, L.B., Grant, J.L., Szatkiewicz, J., Hase, J. van, Shirley, B.-J., Bewersdorf, J., Cremer, C., Arneodo, A., Khalil, A., and Mills, K.D. (2007). Chromosome neighborhood composition determines translocation outcomes after exposure to high-dose radiation in primary cells. *Chromosome Res.* *15*, 1061–1073.

Carlini, L., and Manley, S. (2013). Live Intracellular Super-Resolution Imaging Using Site-Specific Stains. *ACS Chem. Biol.* *8*, 2643–2648.

- Carlini, L., Benke, A., Reymond, L., Lukinavičius, G., and Manley, S. (2014). Reduced Dyes Enhance Single-Molecule Localization Density for Live Superresolution Imaging. *ChemPhysChem* *15*, 750–755.
- Cella Zancchi, F., Lavagnino, Z., Perrone Donnorso, M., Del Bue, A., Furia, L., Faretta, M., and Diaspro, A. (2011). Live-cell 3D super-resolution imaging in thick biological samples. *Nat. Methods* *8*, 1047–1049.
- Chambeyron, S., Silva, N.R.D., Lawson, K.A., and Bickmore, W.A. (2005). Nuclear re-organisation of the Hoxb complex during mouse embryonic development. *Development* *132*, 2215–2223.
- Cheutin, T., and Cavalli, G. (2012). Progressive polycomb assembly on H3K27me3 compartments generates polycomb bodies with developmentally regulated motion. *PLoS Genet.* *8*, e1002465.
- Chmyrov, A., Keller, J., Grotjohann, T., Ratz, M., d'Este, E., Jakobs, S., Eggeling, C., and Hell, S.W. (2013). Nanoscopy with more than 100,000 “doughnuts.” *Nat. Methods* *10*, 737–740.
- Chozinski, T.J., Gagnon, L.A., and Vaughan, J.C. (2014). Twinkle, twinkle little star: Photoswitchable fluorophores for super-resolution imaging. *FEBS Lett.* *588*, 3603–3612.
- Churchman, L.S., and Spudich, J.A. (2012). Single-molecule high-resolution colocalization of single probes. *Cold Spring Harb. Protoc.* *2012*, 242–245.
- Cisse, I.I., Izeddin, I., Causse, S.Z., Boudarene, L., Senecal, A., Muresan, L., Dugast-Darzacq, C., Hajj, B., Dahan, M., and Darzacq, X. (2013). Real-Time Dynamics of RNA Polymerase II Clustering in Live Human Cells. *Science* *341*, 664–667.
- Cordelières, F.P., and Bolte, S. (2014). Experimenters' guide to colocalization studies: finding a way through indicators and quantifiers, in practice. *Methods Cell Biol.* *123*, 395–408.
- Corput, M.P.C. van de, Boer, E. de, Knoch, T.A., Cappellen, W.A. van, Quintanilla, A., Ferrand, L., and Grosveld, F.G. (2012). Super-resolution imaging reveals three-dimensional folding dynamics of the β -globin locus upon gene activation. *J. Cell Sci.* *125*, 4630–4639.
- Cox, S. (2015). Super-resolution imaging in live cells. *Dev. Biol.* *401*, 175–181.
- Crane, E., Bian, Q., McCord, R.P., Lajoie, B.R., Wheeler, B.S., Ralston, E.J., Uzawa, S., Dekker, J., and Meyer, B.J. (2015). Condensin-driven remodelling of X chromosome topology during dosage compensation. *Nature* *523*, 240–244.
- Cremer, T., and Cremer, M. (2010). Chromosome Territories. *Cold Spring Harb. Perspect. Biol.* *2*, a003889.
- Cremer, M., Küpper, K., Wagler, B., Wizelman, L., Hase, J. v, Weiland, Y., Kreja, L., Diebold, J., Speicher, M.R., and Cremer, T. (2003). Inheritance of gene density-related higher order chromatin arrangements in normal and tumor cell nuclei. *J. Cell Biol.* *162*, 809–820.

- Cremer, T., Cremer, M., Hübner, B., Strickfaden, H., Smeets, D., Popken, J., Sterr, M., Markaki, Y., Rippe, K., and Cremer, C. (2015). The 4D nucleome: Evidence for a dynamic nuclear landscape based on co-aligned active and inactive nuclear compartments. *FEBS Lett.* *589*, 2931–2943.
- Crossman, D.J., Hou, Y., Jayasinghe, I., Baddeley, D., and Soeller, C. Combining confocal and single molecule localisation microscopy: A correlative approach to multi-scale tissue imaging. *Methods*.
- Davey, C.A., Sargent, D.F., Luger, K., Maeder, A.W., and Richmond, T.J. (2002). Solvent Mediated Interactions in the Structure of the Nucleosome Core Particle at 1.9 Å Resolution. *J.Mol.Biol.* *319*, 1097–1113.
- Dekker, J., and Heard, E. (2015). Structural and functional diversity of Topologically Associating Domains. *FEBS Lett.*
- Dekker, J., Rippe, K., Dekker, M., and Kleckner, N. (2002). Capturing chromosome conformation. *Science* *295*, 1306–1311.
- Dekker, J., Marti-Renom, M.A., and Mirny, L.A. (2013). Exploring the three-dimensional organization of genomes: interpreting chromatin interaction data. *Nat. Rev. Genet.* *14*, 390–403.
- Dempsey, G.T., Bates, M., Kowtoniuk, W.E., Liu, D.R., Tsien, R.Y., and Zhuang, X. (2009). Photoswitching Mechanism of Cyanine Dyes. *J. Am. Chem. Soc.* *131*, 18192–18193.
- Dempsey, G.T., Vaughan, J.C., Chen, K.H., Bates, M., and Zhuang, X. (2011). Evaluation of fluorophores for optimal performance in localization-based super-resolution imaging. *Nat. Methods* *8*, 1027–1036.
- Dietzel, S., Jauch, A., Kienle, D., Qu, G., Holtgreve-Grez, H., Eils, R., Munkel, C., Bittner, M., Meltzer, P.S., Trent, J.M., et al. (1998). Separate and variably shaped chromosome arm domains are disclosed by chromosome arm painting in human cell nuclei. *Chromosome Res.* *6*, 25–33.
- Ding, J.B., Takasaki, K.T., and Sabatini, B.L. (2009). Supraresolution imaging in brain slices using stimulated-emission depletion two-photon laser scanning microscopy. *Neuron* *63*, 429–437.
- Dixon, J.R., Selvaraj, S., Yue, F., Kim, A., Li, Y., Shen, Y., Hu, M., Liu, J.S., and Ren, B. (2012). Topological domains in mammalian genomes identified by analysis of chromatin interactions. *Nature* *485*, 376–380.
- Donnert, G., Keller, J., Wurm, C.A., Rizzoli, S.O., Westphal, V., Schönle, A., Jahn, R., Jakobs, S., Eggeling, C., and Hell, S.W. (2007). Two-color far-field fluorescence nanoscopy. *Biophys. J.* *92*, L67–L69.
- Dostie, J., Richmond, T.A., Arnaout, R.A., Selzer, R.R., Lee, W.L., Honan, T.A., Rubio, E.D., Krumm, A., Lamb, J., Nusbaum, C., et al. (2006). Chromosome Conformation Capture Carbon Copy (5C): A massively parallel solution for mapping interactions between genomic elements. *Genome Res.* *16*, 1299–1309.

Downen, J.M., Fan, Z.P., Hnisz, D., Ren, G., Abraham, B.J., Zhang, L.N., Weintraub, A.S., Schuijers, J., Lee, T.I., Zhao, K., et al. (2014). Control of cell identity genes occurs in insulated neighborhoods in mammalian chromosomes. *Cell* *159*, 374–387.

Dubochet, J., Adrian, M., Chang, J.J., Homo, J.C., Lepault, J., McDowell, A.W., and Schultz, P. (1988). Cryo-electron microscopy of vitrified specimens. *Q. Rev. Biophys.* *21*, 129–228.

Durisic, N., Cuervo, L.L., and Lakadamyali, M. (2014). Quantitative super-resolution microscopy: pitfalls and strategies for image analysis. *Curr. Opin. Chem. Biol.* *20*, 22–28.

Ea, V., Baudement, M.-O., Lesne, A., and Forné, T. (2015). Contribution of Topological Domains and Loop Formation to 3D Chromatin Organization. *Genes* *6*, 734–750.

Edelstein, A.D., Tsuchida, M.A., Amodaj, N., Pinkard, H., Vale, R.D., and Stuurman, N. (2014). Advanced methods of microscope control using μ Manager software. *J. Biol. Methods* *1*.

Emberly, E., Blattes, R., Schuettengruber, B., Hennion, M., Jiang, N., Hart, C.M., Käs, E., and Cuvier, O. (2008). BEAF regulates cell-cycle genes through the controlled deposition of H3K9 methylation marks into its conserved dual-core binding sites. *PLoS Biol.* *6*, 2896–2910.

Erdélyi, M., Sinkó, J., Kákonyi, R., Kelemen, A., Rees, E., Varga, D., and Szabó, G. Origin and compensation of imaging artefacts in localization-based super-resolution microscopy. *Methods*.

Eskeland, R., Leeb, M., Grimes, G.R., Kress, C., Boyle, S., Sproul, D., Gilbert, N., Fan, Y., Skoultchi, A.I., Wutz, A., et al. (2010). Ring1B compacts chromatin structure and represses gene expression independent of histone ubiquitination. *Mol. Cell* *38*, 452–464.

Feng, S., Cokus, S.J., Schubert, V., Zhai, J., Pellegrini, M., and Jacobsen, S.E. (2014). Genome-wide Hi-C Analyses in Wild-Type and Mutants Reveal High-Resolution Chromatin Interactions in *Arabidopsis*. *Mol. Cell* *55*, 694–707.

Fiche, J.-B., Cattoni, D.I., Diekmann, N., Langerak, J.M., Clerte, C., Royer, C.A., Margeat, E., Doan, T., and Nöllmann, M. (2013a). Recruitment, Assembly, and Molecular Architecture of the SpoIIIE DNA Pump Revealed by Superresolution Microscopy. *PLoS Biol* *11*, e1001557.

Fiche, J.-B., Cattoni, D.I., Diekmann, N., Langerak, J.M., Clerte, C., Royer, C.A., Margeat, E., Doan, T., and Nöllmann, M. (2013b). Recruitment, Assembly, and Molecular Architecture of the SpoIIIE DNA Pump Revealed by Superresolution Microscopy. *PLoS Biol* *11*, e1001557.

Filion, G.J., van Bommel, J.G., Braunschweig, U., Talhout, W., Kind, J., Ward, L.D., Brugman, W., de Castro, I.J., Kerkhoven, R.M., Bussemaker, H.J., et al. (2010). Systematic Protein Location Mapping Reveals Five Principal Chromatin Types in *Drosophila* Cells. *Cell* *143*, 212–224.

Finch, J.T., and Klug, A. (1976). Solenoidal model for superstructure in chromatin. *Proc. Natl. Acad. Sci. U. S. A.* *73*, 1897–1901.

Flors, C. (2010). Photoswitching of monomeric and dimeric DNA-intercalating cyanine dyes for super-resolution microscopy applications. *Photochem. Photobiol. Sci.* *9*, 643–648.

Flors, C. (2011). DNA and chromatin imaging with super-resolution fluorescence microscopy based on single-molecule localization. *Biopolymers* *95*, 290–297.

Flors, C., Ravarani, C.N.J., and Dryden, D.T.F. (2009). Super-Resolution Imaging of DNA Labelled with Intercalating Dyes. *ChemPhysChem* *10*, 2201–2204.

Fornasiero, E.F., and Opazo, F. (2015). Super-resolution imaging for cell biologists. *BioEssays* n/a – n/a.

Fraser, J., Williamson, I., Bickmore, W.A., and Dostie, J. (2015). An Overview of Genome Organization and How We Got There: from FISH to Hi-C. *Microbiol. Mol. Biol. Rev.* *79*, 347–372.

Gautier, A., Juillerat, A., Heinis, C., Corrêa Jr., I.R., Kindermann, M., Beaufile, F., and Johnsson, K. (2008). An Engineered Protein Tag for Multiprotein Labeling in Living Cells. *Chem. Biol.* *15*, 128–136.

Georgieva, M., and Nollmann, M. (2015). Superresolution microscopy for bioimaging at the nanoscale: from concepts to applications in the nucleus. *Res. Rep. Biol.* *157*.

Ghavi-Helm, Y., Klein, F.A., Pakozdi, T., Ciglar, L., Noordermeer, D., Huber, W., and Furlong, E.E.M. (2014). Enhancer loops appear stable during development and are associated with paused polymerase. *Nature advance online publication*.

Giorgetti, L., Galupa, R., Nora, E.P., Piolot, T., Lam, F., Dekker, J., Tiana, G., and Heard, E. (2014). Predictive polymer modeling reveals coupled fluctuations in chromosome conformation and transcription. *Cell* *157*, 950–963.

Goshtasby, A. (1988). Image registration by local approximation methods. *Image Vis. Comput.* *6*, 255–261.

Göttfert, F., Wurm, C.A., Mueller, V., Berning, S., Cordes, V.C., Honigmann, A., and Hell, S.W. (2013). Coaligned dual-channel STED nanoscopy and molecular diffusion analysis at 20 nm resolution. *Biophys. J.* *105*, L01–L03.

Gould, T.J., Myers, J.R., and Bewersdorf, J. (2011). Total internal reflection STED microscopy. *Opt. Express* *19*, 13351–13357.

Gugel, H., Bewersdorf, J., Jakobs, S., Engelhardt, J., Storz, R., and Hell, S.W. (2004). Cooperative 4Pi excitation and detection yields sevenfold sharper optical sections in live-cell microscopy. *Biophys. J.* *87*, 4146–4152.

Gunkel, M., Erdel, F., Rippe, K., Lemmer, P., Kaufmann, R., Hörmann, C., Amberger, R., and Cremer, C. (2009). Dual color localization microscopy of cellular nanostructures. *Biotechnol. J.* *4*, 927–938.

Gustafsson, M.G.L. (2000). Surpassing the lateral resolution limit by a factor of two using structured illumination microscopy. *J. Microsc.* *198*, 82–87.

Gustafsson, M.G.L. (2005). Nonlinear structured-illumination microscopy: Wide-field fluorescence imaging with theoretically unlimited resolution. *Proc. Natl. Acad. Sci. U. S. A.* *102*, 13081–13086.

Gustafsson, M.G.L., Shao, L., Carlton, P.M., Wang, C.J.R., Golubovskaya, I.N., Cande, W.Z., Agard, D.A., and Sedat, J.W. (2008). Three-Dimensional Resolution Doubling in Wide-Field Fluorescence Microscopy by Structured Illumination. *Biophys. J.* *94*, 4957–4970.

Habuchi, S. (2014). Super-Resolution Molecular and Functional Imaging of Nanoscale Architectures in Life and Materials Science. *Front. Bioeng. Biotechnol.* *2*.

Hagège, H., Klous, P., Braem, C., Splinter, E., Dekker, J., Cathala, G., de Laat, W., and Forné, T. (2007). Quantitative analysis of chromosome conformation capture assays (3C-qPCR). *Nat. Protoc.* *2*, 1722–1733.

Hajj, B., Beheiry, M.E., Izeddin, I., Darzacq, X., and Dahan, M. (2014). Accessing the third dimension in localization-based super-resolution microscopy. *Phys. Chem. Chem. Phys.* *16*, 16340–16348.

Hakim, O., Sung, M.-H., Voss, T.C., Splinter, E., John, S., Sabo, P.J., Thurman, R.E., Stamatoyannopoulos, J.A., de Laat, W., and Hager, G.L. (2011). Diverse gene reprogramming events occur in the same spatial clusters of distal regulatory elements. *Genome Res.* *21*, 697–706.

Heilemann, M., Margeat, E., Kasper, R., Sauer, M., and Tinnefeld, P. (2005). Carbocyanine dyes as efficient reversible single-molecule optical switch. *J. Am. Chem. Soc.* *127*, 3801–3806.

Heilemann, M., van de Linde, S., Schüttpelz, M., Kasper, R., Seefeldt, B., Mukherjee, A., Tinnefeld, P., and Sauer, M. (2008). Subdiffraction-Resolution Fluorescence Imaging with Conventional Fluorescent Probes. *Angew. Chem. Int. Ed.* *47*, 6172–6176.

Heilemann, M., van de Linde, S., Mukherjee, A., and Sauer, M. (2009). Super-Resolution Imaging with Small Organic Fluorophores. *Angew. Chem. Int. Ed.* *48*, 6903–6908.

Heintzmann, R., Jovin, T.M., and Cremer, C. (2002). Saturated patterned excitation microscopy--a concept for optical resolution improvement. *J. Opt. Soc. Am. A Opt. Image Sci. Vis.* *19*, 1599–1609.

Hell, S.W., and Wichmann, J. (1994). Breaking the diffraction resolution limit by stimulated emission: stimulated-emission-depletion fluorescence microscopy. *Opt. Lett.* *19*, 780–782.

Hepperger, C., Mannes, A., Merz, J., Peters, J., and Dietzel, S. (2008). Three-dimensional positioning of genes in mouse cell nuclei. *Chromosoma* *117*, 535–551.

- Hess, S.T., Girirajan, T.P.K., and Mason, M.D. (2006). Ultra-High Resolution Imaging by Fluorescence Photoactivation Localization Microscopy. *Biophys. J.* *91*, 4258–4272.
- Hofmann, M., Eggeling, C., Jakobs, S., and Hell, S.W. (2005). Breaking the diffraction barrier in fluorescence microscopy at low light intensities by using reversibly photoswitchable proteins. *Proc. Natl. Acad. Sci. U. S. A.* *102*, 17565–17569.
- Holden, S.J., Pengo, T., Meibom, K.L., Fernandez, C.F., Collier, J., and Manley, S. (2014). High throughput 3D super-resolution microscopy reveals *Caulobacter crescentus* in vivo Z-ring organization. *Proc. Natl. Acad. Sci.* *111*, 4566–4571.
- Horn, P.J., and Peterson, C.L. (2002). Molecular biology. Chromatin higher order folding--wrapping up transcription. *Science* *297*, 1824–1827.
- Hou, C., Li, L., Qin, Z.S., and Corces, V.G. (2012). Gene density, transcription, and insulators contribute to the partition of the *Drosophila* genome into physical domains. *Mol. Cell* *48*, 471–484.
- Hu, Y.S., Zimmerley, M., Li, Y., Watters, R., and Cang, H. (2014). Single-Molecule Super-Resolution Light-Sheet Microscopy. *ChemPhysChem* *15*, 577–586.
- Huang, B., Wang, W., Bates, M., and Zhuang, X. (2008). Three-Dimensional Super-Resolution Imaging by Stochastic Optical Reconstruction Microscopy. *Science* *319*, 810–813.
- Huang, F., Hartwich, T.M.P., Rivera-Molina, F.E., Lin, Y., Duim, W.C., Long, J.J., Uchil, P.D., Myers, J.R., Baird, M.A., Mothes, W., et al. (2013). Video-rate nanoscopy using sCMOS camera-specific single-molecule localization algorithms. *Nat. Methods* *10*, 653–658.
- Hübner, M.R., Eckersley-Maslin, M.A., and Spector, D.L. (2013). Chromatin organization and transcriptional regulation. *Curr. Opin. Genet. Dev.* *23*, 89–95.
- Izeddin, I., El Beheiry, M., Andilla, J., Ciepielewski, D., Darzacq, X., and Dahan, M. (2012). PSF shaping using adaptive optics for three-dimensional single-molecule super-resolution imaging and tracking. *Opt. Express* *20*, 4957.
- Izeddin, I., Récamier, V., Bosanac, L., Cissé, I.I., Boudarene, L., Dugast-Darzacq, C., Proux, F., Bénichou, O., Voituriez, R., Bensaude, O., et al. (2014). Single-molecule tracking in live cells reveals distinct target-search strategies of transcription factors in the nucleus. *eLife* *3*.
- Jensen, N.A., Danzl, J.G., Willig, K.I., Lavoie-Cardinal, F., Brakemann, T., Hell, S.W., and Jakobs, S. (2014). Coordinate-Targeted and Coordinate-Stochastic Super-Resolution Microscopy with the Reversibly Switchable Fluorescent Protein Dreiklang. *ChemPhysChem* *15*, 756–762.
- Jia, S., Vaughan, J.C., and Zhuang, X. (2014). Isotropic 3D Super-resolution Imaging with a Self-bending Point Spread Function. *Nat. Photonics* *8*, 302–306.

- Jost, D., Carrivain, P., Cavalli, G., and Vaillant, C. (2014). Modeling epigenome folding: formation and dynamics of topologically associated chromatin domains. *Nucleic Acids Res.* *42*, 9553–9561.
- Kalhor, R., Tjong, H., Jayathilaka, N., Alber, F., and Chen, L. (2012). Genome architectures revealed by tethered chromosome conformation capture and population-based modeling. *Nat. Biotechnol.* *30*, 90–98.
- Kaplan, C., and Ewers, H. (2015). Optimized sample preparation for single-molecule localization-based superresolution microscopy in yeast. *Nat. Protoc.* *10*, 1007–1021.
- Khalil, A., Grant, J.L., Caddle, L.B., Atzema, E., Mills, K.D., and Arneodo, A. (2007). Chromosome territories have a highly nonspherical morphology and nonrandom positioning. *Chromosome Res.* *15*, 899–916.
- Klar, T.A., and Hell, S.W. (1999). Subdiffraction resolution in far-field fluorescence microscopy. *Opt. Lett.* *24*, 954–956.
- Klar, T.A., Jakobs, S., Dyba, M., Egner, A., and Hell, S.W. (2000). Fluorescence microscopy with diffraction resolution barrier broken by stimulated emission. *Proc. Natl. Acad. Sci. U. S. A.* *97*, 8206–8210.
- Klein, T., Löschberger, A., Proppert, S., Wolter, S., van de Linde, S., and Sauer, M. (2011). Live-cell dSTORM with SNAP-tag fusion proteins. *Nat. Methods* *8*, 7–9.
- Klein, T., van de Linde, S., and Sauer, M. (2012). Live-Cell Super-Resolution Imaging Goes Multicolor. *ChemBioChem* *13*, 1861–1863.
- Kouzarides, T. (2007). Chromatin Modifications and Their Function. *Cell* *128*, 693–705.
- Kozubek, S., Lukášová, E., Jirsová, P., Koutná, I., Kozubek, M., Ganová, A., Bártová, E., Falk, M., and Paseková, R. (2002). 3D Structure of the human genome: order in randomness. *Chromosoma* *111*, 321–331.
- Küpper, K., Kölbl, A., Biener, D., Dittrich, S., Hase, J. von, Thormeyer, T., Fiegler, H., Carter, N.P., Speicher, M.R., Cremer, T., et al. (2007). Radial chromatin positioning is shaped by local gene density, not by gene expression. *Chromosoma* *116*, 285–306.
- Lampe, A., Tadeus, G., and Schmoranzler, J. (2015). Spectral demixing avoids registration errors and reduces noise in multicolor localization-based super-resolution microscopy. *Methods Appl. Fluoresc.* *3*, 034006.
- Lanctôt, C., Cheutin, T., Cremer, M., Cavalli, G., and Cremer, T. (2007). Dynamic genome architecture in the nuclear space: regulation of gene expression in three dimensions. *Nat. Rev. Genet.* *8*, 104–115.
- Le, T.B.K., Imakaev, M.V., Mirny, L.A., and Laub, M.T. (2013). High-Resolution Mapping of the Spatial Organization of a Bacterial Chromosome. *Science* *342*, 731–734.

- Le Dily, F., Baù, D., Pohl, A., Vicent, G.P., Serra, F., Soronellas, D., Castellano, G., Wright, R.H.G., Ballare, C., Fillion, G., et al. (2014). Distinct structural transitions of chromatin topological domains correlate with coordinated hormone-induced gene regulation. *Genes Dev.* 28, 2151–2162.
- Le Gall, A., Valeri, A., and Nollmann, M. (2015). Roles of chromatin insulators in the formation of long-range contacts. *Nucl. Austin Tex* 6, 118–122.
- Leutenegger, M., Ringemann, C., Lasser, T., Hell, S.W., and Eggeling, C. (2012). Fluorescence correlation spectroscopy with a total internal reflection fluorescence STED microscope (TIRF-STED-FCS). *Opt. Express* 20, 5243–5263.
- Li, L., Lyu, X., Hou, C., Takenaka, N., Nguyen, H.Q., Ong, C.-T., Cubeñas-Potts, C., Hu, M., Lei, E.P., Bosco, G., et al. (2015). Widespread rearrangement of 3D chromatin organization underlies polycomb-mediated stress-induced silencing. *Mol. Cell* 58, 216–231.
- Liang, J., Lacroix, L., Gamot, A., Cuddapah, S., Queille, S., Lhoumaud, P., Lepetit, P., Martin, P.G.P., Vogelmann, J., Court, F., et al. (2014). Chromatin immunoprecipitation indirect peaks highlight long-range interactions of insulator proteins and Pol II pausing. *Mol. Cell* 53, 672–681.
- Lieberman-Aiden, E., Berkum, N.L. van, Williams, L., Imakaev, M., Ragoczy, T., Telling, A., Amit, I., Lajoie, B.R., Sabo, P.J., Dorschner, M.O., et al. (2009). Comprehensive Mapping of Long-Range Interactions Reveals Folding Principles of the Human Genome. *Science* 326, 289–293.
- van de Linde, S., Wolter, S., Heilemann, M., and Sauer, M. (2010). The effect of photoswitching kinetics and labeling densities on super-resolution fluorescence imaging. *J. Biotechnol.* 149, 260–266.
- van de Linde, S., Löschberger, A., Klein, T., Heidebreder, M., Wolter, S., Heilemann, M., and Sauer, M. (2011). Direct stochastic optical reconstruction microscopy with standard fluorescent probes. *Nat. Protoc.* 6, 991–1009.
- Lukinavičius, G., Umezawa, K., Olivier, N., Honigmann, A., Yang, G., Plass, T., Mueller, V., Reymond, L., Corrêa Jr, I.R., Luo, Z.-G., et al. (2013). A near-infrared fluorophore for live-cell super-resolution microscopy of cellular proteins. *Nat. Chem.* 5, 132–139.
- Lundberg, E., Sundberg, M., Gräslund, T., Uhlén, M., and Svahn, H.A. (2007). A novel method for reproducible fluorescent labeling of small amounts of antibodies on solid phase. *J. Immunol. Methods* 322, 40–49.
- Lupiáñez, D.G., Kraft, K., Heinrich, V., Krawitz, P., Brancati, F., Klopocki, E., Horn, D., Kayserili, H., Opitz, J.M., Laxova, R., et al. (2015). Disruptions of topological chromatin domains cause pathogenic rewiring of gene-enhancer interactions. *Cell* 161, 1012–1025.
- Maeshima, K., Imai, R., Tamura, S., and Nozaki, T. (2014). Chromatin as dynamic 10-nm fibers. *Chromosoma* 123, 225–237.

- Mahy, N.L., Perry, P.E., Gilchrist, S., Baldock, R.A., and Bickmore, W.A. (2002). Spatial organization of active and inactive genes and noncoding DNA within chromosome territories. *J. Cell Biol.* *157*, 579–589.
- Malkusch, S., Endesfelder, U., Mondry, J., Gelléri, M., Verveer, P.J., and Heilemann, M. (2011). Coordinate-based colocalization analysis of single-molecule localization microscopy data. *Histochem. Cell Biol.* *137*, 1–10.
- Malkusch, S., Muranyi, W., Müller, B., Kräusslich, H.-G., and Heilemann, M. (2012). Single-molecule coordinate-based analysis of the morphology of HIV-1 assembly sites with near-molecular spatial resolution. *Histochem. Cell Biol.* *139*, 173–179.
- Manders, E.M., Stap, J., Brakenhoff, G.J., Driel, R. van, and Aten, J.A. (1992). Dynamics of three-dimensional replication patterns during the S-phase, analysed by double labelling of DNA and confocal microscopy. *J. Cell Sci.* *103*, 857–862.
- Manley, S., Gunzenhäuser, J., and Olivier, N. (2011). A starter kit for point-localization super-resolution imaging. *Curr. Opin. Chem. Biol.* *15*, 813–821.
- Marbouty, M., Le Gall, A., Cattoni, D.I., Cournac, A., Koh, A., Fiche, J.-B., Mozziconacci, J., Murray, H., Koszul, R., and Nollmann, M. (2015). Condensin- and Replication-Mediated Bacterial Chromosome Folding and Origin Condensation Revealed by Hi-C and Super-resolution Imaging. *Mol. Cell* *59*, 588–602.
- Markaki, Y., Smeets, D., Fiedler, S., Schmid, V.J., Schermelleh, L., Cremer, T., and Cremer, M. (2012). The potential of 3D-FISH and super-resolution structured illumination microscopy for studies of 3D nuclear architecture. *BioEssays* *34*, 412–426.
- Mazzarello, P. (1999). A unifying concept: the history of cell theory. *Nat. Cell Biol.* *1*, E13–E15.
- McEvoy, A.L., Hoi, H., Bates, M., Platonova, E., Cranfill, P.J., Baird, M.A., Davidson, M.W., Ewers, H., Liphardt, J., and Campbell, R.E. (2012). mMaple: A Photoconvertible Fluorescent Protein for Use in Multiple Imaging Modalities. *PLoS ONE* *7*, e51314.
- Meyer, L., Wildanger, D., Medda, R., Punge, A., Rizzoli, S.O., Donnert, G., and Hell, S.W. (2008). Dual-color STED microscopy at 30-nm focal-plane resolution. *Small* *4*, 1095–1100.
- von Middendorff, C., Egner, A., Geisler, C., Hell, S.W., and Schönle, A. (2008). Isotropic 3D Nanoscopy based on single emitter switching. *Opt. Express* *16*, 20774–20788.
- Mirny, L.A. (2011). The fractal globule as a model of chromatin architecture in the cell. *Chromosome Res. Int. J. Mol. Supramol. Evol. Asp. Chromosome Biol.* *19*, 37–51.
- Mitchell-Jordan, S., Chen, H., Franklin, S., Stefani, E., Bentolila, L.A., and Vondriska, T.M. (2012). Features of endogenous cardiomyocyte chromatin revealed by super-resolution STED microscopy. *J. Mol. Cell. Cardiol.* *53*, 552–558.

- Mizuguchi, T., Fudenberg, G., Mehta, S., Belton, J.-M., Taneja, N., Folco, H.D., FitzGerald, P., Dekker, J., Mirny, L., Barrowman, J., et al. (2014). Cohesin-dependent globules and heterochromatin shape 3D genome architecture in *S. pombe*. *Nature* *516*, 432–435.
- Moffitt, J.R., Osseforth, C., and Michaelis, J. (2011). Time-gating improves the spatial resolution of STED microscopy. *Opt. Express* *19*, 4242–4254.
- Moneron, G., and Hell, S.W. (2009). Two-photon excitation STED microscopy. *Opt. Express* *17*, 14567–14573.
- Morey, L., and Helin, K. (2010). Polycomb group protein-mediated repression of transcription. *Trends Biochem. Sci.* *35*, 323–332.
- Müller, T., Schumann, C., and Kraegeloh, A. (2012). STED Microscopy and its Applications: New Insights into Cellular Processes on the Nanoscale. *ChemPhysChem* *13*, 1986–2000.
- Murmann, A.E., Gao, J., Encinosa, M., Gautier, M., Peter, M.E., Eils, R., Lichter, P., and Rowley, J.D. (2005). Local gene density predicts the spatial position of genetic loci in the interphase nucleus. *Exp. Cell Res.* *311*, 14–26.
- Nagano, T., Lubling, Y., Stevens, T.J., Schoenfelder, S., Yaffe, E., Dean, W., Laue, E.D., Tanay, A., and Fraser, P. (2013). Single-cell Hi-C reveals cell-to-cell variability in chromosome structure. *Nature* *502*, 59–64.
- Naumova, N., Imakaev, M., Fudenberg, G., Zhan, Y., Lajoie, B.R., Mirny, L.A., and Dekker, J. (2013). Organization of the Mitotic Chromosome. *Science* *342*, 948–953.
- Nègre, N., Brown, C.D., Shah, P.K., Kheradpour, P., Morrison, C.A., Henikoff, J.G., Feng, X., Ahmad, K., Russell, S., White, R.A.H., et al. (2010). A comprehensive map of insulator elements for the *Drosophila* genome. *PLoS Genet.* *6*, e1000814.
- Neupane, B., Chen, F., Sun, W., Chiu, D.T., and Wang, G. (2013). Tuning donut profile for spatial resolution in stimulated emission depletion microscopy. *Rev. Sci. Instrum.* *84*, 043701.
- Neupane, B., Ligler, F.S., and Wang, G. (2014). Review of recent developments in stimulated emission depletion microscopy: applications on cell imaging. *J. Biomed. Opt.* *19*, 080901–080901.
- Nieuwenhuizen, R.P.J., Lidke, K.A., Bates, M., Puig, D.L., Grünwald, D., Stallinga, S., and Rieger, B. (2013). Measuring image resolution in optical nanoscopy. *Nat. Methods* *10*, 557–562.
- Nishino, Y., Eltsov, M., Joti, Y., Ito, K., Takata, H., Takahashi, Y., Hihara, S., Frangakis, A.S., Imamoto, N., Ishikawa, T., et al. (2012). Human mitotic chromosomes consist predominantly of irregularly folded nucleosome fibres without a 30-nm chromatin structure. *EMBO J.* *31*, 1644–1653.
- Nora, E.P., Lajoie, B.R., Schulz, E.G., Giorgetti, L., Okamoto, I., Servant, N., Pilot, T., van Berkum, N.L., Meisig, J., Sedat, J., et al. (2012). Spatial

partitioning of the regulatory landscape of the X-inactivation centre. *Nature* **485**, 381–385.

Oegema, K., Whitfield, W.G., and Alberts, B. (1995). The cell cycle-dependent localization of the CP190 centrosomal protein is determined by the coordinate action of two separable domains. *J. Cell Biol.* **131**, 1261–1273.

Olivier, N., Keller, D., Rajan, V.S., Gönczy, P., and Manley, S. (2013). Simple buffers for 3D STORM microscopy. *Biomed. Opt. Express* **4**, 885.

Pageon, S.V., Cordoba, S.-P., Owen, D.M., Rothery, S.M., Oszmiana, A., and Davis, D.M. (2013). Superresolution Microscopy Reveals Nanometer-Scale Reorganization of Inhibitory Natural Killer Cell Receptors upon Activation of NKG2D. *Sci. Signal.* **6**, ra62–ra62.

Palstra, R.-J., Simonis, M., Klous, P., Brasslet, E., Eijkelkamp, B., and de Laat, W. (2008). Maintenance of Long-Range DNA Interactions after Inhibition of Ongoing RNA Polymerase II Transcription. *PLoS ONE* **3**, e1661.

Papantonis, A., and Cook, P.R. (2013). Transcription Factories: Genome Organization and Gene Regulation. *Chem. Rev.* **113**, 8683–8705.

Parada, L.A., McQueen, P.G., and Misteli, T. (2004). Tissue-specific spatial organization of genomes. *Genome Biol.* **5**, R44.

Patterson, G., Davidson, M., Manley, S., and Lippincott-Schwartz, J. (2010). Superresolution Imaging using Single-Molecule Localization. *Annu. Rev. Phys. Chem.* **61**, 345–367.

Pavani, S.R.P., Thompson, M.A., Biteen, J.S., Lord, S.J., Liu, N., Twieg, R.J., Piestun, R., and Moerner, W.E. (2009). Three-dimensional, single-molecule fluorescence imaging beyond the diffraction limit by using a double-helix point spread function. *Proc. Natl. Acad. Sci. U. S. A.* **106**, 2995–2999.

Pellett, P.A., Sun, X., Gould, T.J., Rothman, J.E., Xu, M.-Q., Corrêa, I.R., and Bewersdorf, J. (2011). Two-color STED microscopy in living cells. *Biomed. Opt. Express* **2**, 2364–2371.

Phillips-Cremins, J.E., Sauria, M.E.G., Sanyal, A., Gerasimova, T.I., Lajoie, B.R., Bell, J.S.K., Ong, C.-T., Hookway, T.A., Guo, C., Sun, Y., et al. (2013). Architectural protein subclasses shape 3D organization of genomes during lineage commitment. *Cell* **153**, 1281–1295.

Puchner, E.M., Walter, J.M., Kasper, R., Huang, B., and Lim, W.A. (2013). Counting molecules in single organelles with superresolution microscopy allows tracking of the endosome maturation trajectory. *Proc. Natl. Acad. Sci.* **110**, 16015–16020.

Ram, S., Prabhat, P., Chao, J., Ward, E.S., and Ober, R.J. (2008). High accuracy 3D quantum dot tracking with multifocal plane microscopy for the study of fast intracellular dynamics in live cells. *Biophys. J.* **95**, 6025–6043.

Rao, S.S.P., Huntley, M.H., Durand, N.C., Stamenova, E.K., Bochkov, I.D., Robinson, J.T., Sanborn, A.L., Machol, I., Omer, A.D., Lander, E.S., et al. (2014).

A 3D Map of the Human Genome at Kilobase Resolution Reveals Principles of Chromatin Looping. *Cell* 159, 1665–1680.

Rath, U., Ding, Y., Deng, H., Qi, H., Bao, X., Zhang, W., Girton, J., Johansen, J., and Johansen, K.M. (2006). The chromodomain protein, Chromator, interacts with JIL-1 kinase and regulates the structure of *Drosophila* polytene chromosomes. *J. Cell Sci.* 119, 2332–2341.

Rayleigh, Lord (1896). XV. On the theory of optical images, with special reference to the microscope. *Philos. Mag. Ser. 5* 42, 167–195.

Récamier, V., Izeddin, I., Bosanac, L., Dahan, M., Proux, F., and Darzacq, X. (2014). Single cell correlation fractal dimension of chromatin. *Nucleus* 5, 75–84.

Rego, E.H., Shao, L., Macklin, J.J., Winoto, L., Johansson, G.A., Kamps-Hughes, N., Davidson, M.W., and Gustafsson, M.G.L. (2012). Nonlinear structured-illumination microscopy with a photoswitchable protein reveals cellular structures at 50-nm resolution. *Proc. Natl. Acad. Sci.* 109, E135–E143.

Ricci, M.A., Manzo, C., García-Parajo, M.F., Lakadamyali, M., and Cosma, M.P. (2015). Chromatin Fibers Are Formed by Heterogeneous Groups of Nucleosomes In Vivo. *Cell* 160, 1145–1158.

Riddle, N.C., Minoda, A., Kharchenko, P.V., Alekseyenko, A.A., Schwartz, Y.B., Tolstorukov, M.Y., Gorchakov, A.A., Jaffe, J.D., Kennedy, C., Linder-Basso, D., et al. (2011). Plasticity in patterns of histone modifications and chromosomal proteins in *Drosophila* heterochromatin. *Genome Res.* 21, 147–163.

Ries, J., Kaplan, C., Platonova, E., Eghlidi, H., and Ewers, H. (2012a). A simple, versatile method for GFP-based super-resolution microscopy via nanobodies. *Nat. Methods* 9, 582–584.

Ries, J., Kaplan, C., Platonova, E., Eghlidi, H., and Ewers, H. (2012b). A simple, versatile method for GFP-based super-resolution microscopy via nanobodies. *Nat. Methods* 9, 582–584.

Ripley, B.D. (1977). Modelling Spatial Patterns. *J. R. Stat. Soc. Ser. B Methodol.* 39, 172–212.

Rust, M.J., Bates, M., and Zhuang, X. (2006). Sub-diffraction-limit imaging by stochastic optical reconstruction microscopy (STORM). *Nat. Methods* 3, 793–796.

Sachs, R.K., van den Engh, G., Trask, B., Yokota, H., and Hearst, J.E. (1995). A random-walk/giant-loop model for interphase chromosomes. *Proc. Natl. Acad. Sci. U. S. A.* 92, 2710–2714.

Sauer, M. (2013). Localization microscopy coming of age: from concepts to biological impact. *J. Cell Sci.* 126, 3505–3513.

Scarselli, M., Annibale, P., and Radenovic, A. (2012). Cell Type-specific β 2-Adrenergic Receptor Clusters Identified Using Photoactivated Localization Microscopy Are Not Lipid Raft Related, but Depend on Actin Cytoskeleton Integrity. *J. Biol. Chem.* 287, 16768–16780.

- Schermelleh, L., Solovei, I., Zink, D., and Cremer, T. (2001). Two-color fluorescence labeling of early and mid-to-late replicating chromatin in living cells. *Chromosome Res. Int. J. Mol. Supramol. Evol. Asp. Chromosome Biol.* *9*, 77–80.
- Schermelleh, L., Carlton, P.M., Haase, S., Shao, L., Winoto, L., Kner, P., Burke, B., Cardoso, M.C., Agard, D.A., Gustafsson, M.G.L., et al. (2008). Subdiffraction Multicolor Imaging of the Nuclear Periphery with 3D Structured Illumination Microscopy. *Science* *320*, 1332–1336.
- Schermelleh, L., Heintzmann, R., and Leonhardt, H. (2010). A guide to super-resolution fluorescence microscopy. *J. Cell Biol.* *190*, 165–175.
- Schmidt, R., Wurm, C.A., Jakobs, S., Engelhardt, J., Egner, A., and Hell, S.W. (2008). Spherical nanosized focal spot unravels the interior of cells. *Nat. Methods* *5*, 539–544.
- Schoborg, T., Rickels, R., Barrios, J., and Labrador, M. (2013). Chromatin insulator bodies are nuclear structures that form in response to osmotic stress and cell death. *J. Cell Biol.* *202*, 261–276.
- Schoen, I., Ries, J., Klotzsch, E., Ewers, H., and Vogel, V. (2011). Binding-activated localization microscopy of DNA structures. *Nano Lett.* *11*, 4008–4011.
- Seitan, V.C., Faure, A.J., Zhan, Y., McCord, R.P., Lajoie, B.R., Ing-Simmons, E., Lenhard, B., Giorgetti, L., Heard, E., Fisher, A.G., et al. (2013). Cohesin-based chromatin interactions enable regulated gene expression within preexisting architectural compartments. *Genome Res.* *23*, 2066–2077.
- Sengupta, P., Jovanovic-Talisman, T., Skoko, D., Renz, M., Veatch, S.L., and Lippincott-Schwartz, J. (2011). Probing protein heterogeneity in the plasma membrane using PALM and pair correlation analysis. *Nat. Methods* *8*, 969–975.
- Sengupta, P., Van Engelenburg, S., and Lippincott-Schwartz, J. (2012). Visualizing Cell Structure and Function with Point-Localization Superresolution Imaging. *Dev. Cell* *23*, 1092–1102.
- Sergé, A., Bertaux, N., Rigneault, H., and Marguet, D. (2008). Dynamic multiple-target tracing to probe spatiotemporal cartography of cell membranes. *Nat. Methods* *5*, 687–694.
- Sexton, T., and Cavalli, G. (2015a). The Role of Chromosome Domains in Shaping the Functional Genome. *Cell* *160*, 1049–1059.
- Sexton, T., and Cavalli, G. (2015b). The Role of Chromosome Domains in Shaping the Functional Genome. *Cell* *160*, 1049–1059.
- Sexton, T., Yaffe, E., Kenigsberg, E., Bantignies, F., Leblanc, B., Hoichman, M., Parrinello, H., Tanay, A., and Cavalli, G. (2012). Three-dimensional folding and functional organization principles of the *Drosophila* genome. *Cell* *148*, 458–472.
- Shcherbakova, D.M., Sengupta, P., Lippincott-Schwartz, J., and Verkhusha, V.V. (2014). Photocontrollable Fluorescent Proteins for Superresolution Imaging. *Annu. Rev. Biophys.* *43*, 303–329.

- Shivanandan, A., Deschout, H., Scarselli, M., and Radenovic, A. (2014). Challenges in quantitative single molecule localization microscopy. *FEBS Lett.* *588*, 3595–3602.
- Shopland, L.S., Lynch, C.R., Peterson, K.A., Thornton, K., Kepper, N., Hase, J. von, Stein, S., Vincent, S., Molloy, K.R., Kreth, G., et al. (2006). Folding and organization of a contiguous chromosome region according to the gene distribution pattern in primary genomic sequence. *J. Cell Biol.* *174*, 27–38.
- Shroff, H., Galbraith, C.G., Galbraith, J.A., White, H., Gillette, J., Olenych, S., Davidson, M.W., and Betzig, E. (2007). Dual-color superresolution imaging of genetically expressed probes within individual adhesion complexes. *Proc. Natl. Acad. Sci.* *104*, 20308–20313.
- Simonis, M., Kooren, J., and de Laat, W. (2007). An evaluation of 3C-based methods to capture DNA interactions. *Nat. Methods* *4*, 895–901.
- Sofueva, S., Yaffe, E., Chan, W.-C., Georgopoulou, D., Vietri Rudan, M., Mira-Bontenbal, H., Pollard, S.M., Schroth, G.P., Tanay, A., and Hadjur, S. (2013). Cohesin-mediated interactions organize chromosomal domain architecture. *EMBO J.* *32*, 3119–3129.
- Specht, C.G., Izeddin, I., Rodriguez, P.C., El Beheiry, M., Rostaing, P., Darzacq, X., Dahan, M., and Triller, A. (2013). Quantitative nanoscopy of inhibitory synapses: counting gephyrin molecules and receptor binding sites. *Neuron* *79*, 308–321.
- Stephens, D.J., and Allan, V.J. (2003). *Light Microscopy Techniques for Live Cell Imaging.* *Science* *300*, 82–86.
- Subach, F.V., Patterson, G.H., Manley, S., Gillette, J.M., Lippincott-Schwartz, J., and Verkhusa, V.V. (2009). Photoactivatable mCherry for high-resolution two-color fluorescence microscopy. *Nat. Methods* *6*, 153–159.
- Takasaki, K.T., Ding, J.B., and Sabatini, B.L. (2013). Live-cell superresolution imaging by pulsed STED two-photon excitation microscopy. *Biophys. J.* *104*, 770–777.
- Testa, I., Wurm, C.A., Medda, R., Rothermel, E., von Middendorf, C., Fölling, J., Jakobs, S., Schönle, A., Hell, S.W., and Eggeling, C. (2010). Multicolor Fluorescence Nanoscopy in Fixed and Living Cells by Exciting Conventional Fluorophores with a Single Wavelength. *Biophys. J.* *99*, 2686–2694.
- Thompson, R.E., Larson, D.R., and Webb, W.W. (2002). Precise Nanometer Localization Analysis for Individual Fluorescent Probes. *Biophys. J.* *82*, 2775–2783.
- Thurman, R.E., Rynes, E., Humbert, R., Vierstra, J., Maurano, M.T., Haugen, E., Sheffield, N.C., Stergachis, A.B., Wang, H., Vernot, B., et al. (2012). The accessible chromatin landscape of the human genome. *Nature* *489*, 75–82.
- Tolhuis, B., Blom, M., Kerkhoven, R.M., Pagie, L., Teunissen, H., Nieuwland, M., Simonis, M., de Laat, W., van Lohuizen, M., and van Steensel, B. (2011).

Interactions among Polycomb Domains Are Guided by Chromosome Architecture. *PLoS Genet* 7, e1001343.

Tønnesen, J., Nadrigny, F., Willig, K.I., Wedlich-Söldner, R., and Nägerl, U.V. (2011). Two-color STED microscopy of living synapses using a single laser-beam pair. *Biophys. J.* 101, 2545–2552.

Umbarger, M.A., Toro, E., Wright, M.A., Porreca, G.J., Baù, D., Hong, S.-H., Fero, M.J., Zhu, L.J., Marti-Renom, M.A., McAdams, H.H., et al. (2011). The three-dimensional architecture of a bacterial genome and its alteration by genetic perturbation. *Mol. Cell* 44, 252–264.

Van Bortle, K., and Corces, V.G. (2012). Nuclear organization and genome function. *Annu. Rev. Cell Dev. Biol.* 28, 163–187.

Van Bortle, K., Nichols, M.H., Li, L., Ong, C.-T., Takenaka, N., Qin, Z.S., and Corces, V.G. (2014). Insulator function and topological domain border strength scale with architectural protein occupancy. *Genome Biol.* 15, R82.

Veatch, S.L., Machta, B.B., Shelby, S.A., Chiang, E.N., Holowka, D.A., and Baird, B.A. (2012). Correlation functions quantify super-resolution images and estimate apparent clustering due to over-counting. *PLoS One* 7, e31457.

Vicidomini, G., Moneron, G., Han, K.Y., Westphal, V., Ta, H., Reuss, M., Engelhardt, J., Eggeling, C., and Hell, S.W. (2011). Sharper low-power STED nanoscopy by time gating. *Nat. Methods* 8, 571–573.

Vietri Rudan, M., Barrington, C., Henderson, S., Ernst, C., Odom, D.T., Tanay, A., and Hadjur, S. (2015). Comparative Hi-C reveals that CTCF underlies evolution of chromosomal domain architecture. *Cell Rep.* 10, 1297–1309.

Vogelmann, J., Valeri, A., Guillou, E., Cuvier, O., and Nollmann, M. (2011). Roles of chromatin insulator proteins in higher-order chromatin organization and transcription regulation. *Nucl. Austin Tex* 2, 358–369.

Vogelmann, J., Le Gall, A., Dejardin, S., Allemand, F., Gamot, A., Labesse, G., Cuvier, O., Nègre, N., Cohen-Gonsaud, M., Margeat, E., et al. (2014). Chromatin insulator factors involved in long-range DNA interactions and their role in the folding of the *Drosophila* genome. *PLoS Genet.* 10, e1004544.

Volpi, E.V., Chevret, E., Jones, T., Vatcheva, R., Williamson, J., Beck, S., Campbell, R.D., Goldsworthy, M., Powis, S.H., Ragoussis, J., et al. (2000). Large-scale chromatin organization of the major histocompatibility complex and other regions of human chromosome 6 and its response to interferon in interphase nuclei. *J. Cell Sci.* 113, 1565–1576.

Wang, S., Moffitt, J.R., Dempsey, G.T., Xie, X.S., and Zhuang, X. (2014a). Characterization and development of photoactivatable fluorescent proteins for single-molecule-based superresolution imaging. *Proc. Natl. Acad. Sci.* 111, 8452–8457.

Wang, Y., Schnitzbauer, J., Hu, Z., Li, X., Cheng, Y., Huang, Z.-L., and Huang, B. (2014b). Localization events-based sample drift correction for localization

microscopy with redundant cross-correlation algorithm. *Opt. Express* 22, 15982–15991.

Westphal, V., Rizzoli, S.O., Lauterbach, M.A., Kamin, D., Jahn, R., and Hell, S.W. (2008). Video-Rate Far-Field Optical Nanoscopy Dissects Synaptic Vesicle Movement. *Science* 320, 246–249.

Whelan, D.R., and Bell, T.D.M. (2015). Image artifacts in Single Molecule Localization Microscopy: why optimization of sample preparation protocols matters. *Sci. Rep.* 5.

Williamson, I., Berlivet, S., Eskeland, R., Boyle, S., Illingworth, R.S., Paquette, D., Dostie, J., and Bickmore, W.A. (2014). Spatial genome organization: contrasting views from chromosome conformation capture and fluorescence in situ hybridization. *Genes Dev.* 28, 2778–2791.

Willig, K.I., Harke, B., Medda, R., and Hell, S.W. (2007). STED microscopy with continuous wave beams. *Nat. Methods* 4, 915–918.

Willig, K.I., Stiel, A.C., Brakemann, T., Jakobs, S., and Hell, S.W. (2011). Dual-label STED nanoscopy of living cells using photochromism. *Nano Lett.* 11, 3970–3973.

Wombacher, R., Heidbreder, M., van de Linde, S., Sheetz, M.P., Heilemann, M., Cornish, V.W., and Sauer, M. (2010). Live-cell super-resolution imaging with trimethoprim conjugates. *Nat. Methods* 7, 717–719.

Wood, A.M., Van Bortle, K., Ramos, E., Takenaka, N., Rohrbaugh, M., Jones, B.C., Jones, K.C., and Corces, V.G. (2011). Regulation of chromatin organization and inducible gene expression by a *Drosophila* insulator. *Mol. Cell* 44, 29–38.

Würtele, H., and Chartrand, P. (2006). Genome-wide scanning of HoxB1-associated loci in mouse ES cells using an open-ended Chromosome Conformation Capture methodology. *Chromosome Res.* 14, 477–495.

Xu, K., Zhong, G., and Zhuang, X. (2013). Actin, Spectrin, and Associated Proteins Form a Periodic Cytoskeletal Structure in Axons. *Science* 339, 452–456.

Yaffe, E., and Tanay, A. (2011). Probabilistic modeling of Hi-C contact maps eliminates systematic biases to characterize global chromosomal architecture. *Nat. Genet.* 43, 1059–1065.

York, A.G., Ghitani, A., Vaziri, A., Davidson, M.W., and Shroff, H. (2011). Confined activation and subdiffractive localization enables whole-cell PALM with genetically expressed probes. *Nat. Methods* 8, 327–333.

Zabidi, M.A., Arnold, C.D., Schernhuber, K., Pagani, M., Rath, M., Frank, O., and Stark, A. (2015). Enhancer-core-promoter specificity separates developmental and housekeeping gene regulation. *Nature* 518, 556–559.

Zessin, P.J.M., Finan, K., and Heilemann, M. (2012). Super-resolution fluorescence imaging of chromosomal DNA. *J. Struct. Biol.* 177, 344–348.

Zhang, Y., McCord, R.P., Ho, Y.-J., Lajoie, B.R., Hildebrand, D.G., Simon, A.C., Becker, M.S., Alt, F.W., and Dekker, J. (2012). Spatial Organization of the Mouse Genome and Its Role in Recurrent Chromosomal Translocations. *Cell* *148*, 908–921.

Zhao, Z.W., Roy, R., Gebhardt, J.C.M., Suter, D.M., Chapman, A.R., and Xie, X.S. (2014). Spatial organization of RNA polymerase II inside a mammalian cell nucleus revealed by reflected light-sheet superresolution microscopy. *Proc. Natl. Acad. Sci.* *111*, 681–686.

Zhou, X.X., and Lin, M.Z. (2013). Photoswitchable fluorescent proteins: ten years of colorful chemistry and exciting applications. *Curr. Opin. Chem. Biol.* *17*, 682–690.

Zhu, L., Zhang, W., Elnatan, D., and Huang, B. (2012). Faster STORM using compressed sensing. *Nat. Methods* *9*, 721–723.

Zuin, J., Dixon, J.R., Reijden, M.I.J.A. van der, Ye, Z., Kolovos, P., Brouwer, R.W.W., Corput, M.P.C. van de, Werken, H.J.G. van de, Knoch, T.A., IJcken, W.F.J. van, et al. (2014a). Cohesin and CTCF differentially affect chromatin architecture and gene expression in human cells. *Proc. Natl. Acad. Sci.* *111*, 996–1001.

Zuin, J., Franke, V., van IJcken, W.F.J., van der Sloot, A., Krantz, I.D., van der Reijden, M.I.J.A., Nakato, R., Lenhard, B., and Wendt, K.S. (2014b). A Cohesin-Independent Role for NIPBL at Promoters Provides Insights in CdLS. *PLoS Genet* *10*, e1004153.